

MODELING OF ACCELERATOR SYSTEMS AND EXPERIMENTAL VERIFICATION
OF QUARTER-WAVE RESONATOR STEERING

By

Carla Benatti

A DISSERTATION

Submitted to
Michigan State University
in partial fulfillment of the requirements
for the degree of

Physics - Doctor of Philosophy

2014

ABSTRACT

MODELING OF ACCELERATOR SYSTEMS AND EXPERIMENTAL VERIFICATION OF QUARTER-WAVE RESONATOR STEERING

By

Carla Benatti

Increasingly complicated accelerator systems depend more and more on computing power and computer simulations for their operation as progress in the field has led to cutting-edge advances that require finer control and better understanding to achieve optimal performance. Greater ambitions coupled with the technical complexity of today's state-of-the-art accelerators necessitate corresponding advances in available accelerator modeling resources.

Modeling is a critical component of any field of physics, accelerator physics being no exception. It is extremely important to not only understand the basic underlying physics principles but to implement this understanding through the development of relevant modeling tools that provide the ability to investigate and study various complex effects. Moreover, these tools can lead to new insight and applications that facilitate control room operations and enable advances in the field that would not otherwise be possible.

The ability to accurately model accelerator systems aids in the successful operation of machines designed specifically to deliver beams to experiments across a wide variety of fields, ranging from material science research to nuclear astrophysics. One such accelerator discussed throughout this work is the ReA facility at the National Superconducting Cyclotron Laboratory (NSCL) which re-accelerates rare isotope beams for nuclear astrophysics experiments.

A major component of the ReA facility, as well as the future Facility for Rare Isotope Beams (FRIB) among other accelerators, is the Quarter-Wave Resonator (QWR), a coaxial

accelerating cavity convenient for efficient acceleration of low-velocity particles. This device is very important to model accurately as it operates in the critical low-velocity region where the beam's acceleration gains are proportionally larger than they are through the later stages of acceleration. Compounding this matter, QWRs defocus the beam, and are also asymmetric with respect to the beam pipe, which has the potential to induce steering on the beam. These additional complications make this a significant device to study in order to optimize the accelerator's overall performance.

The NSCL and ReA, along with FRIB, are first introduced to provide background and motivate the central modeling objectives presented throughout this work. In the next chapter, underlying beam physics principles are then discussed, as they form the basis from which modeling methods are derived. The modeling methods presented include multi-particle tracking and beam envelope matrix transport. The following chapter investigates modeling elements in more detail, including quadrupoles, solenoids, and coaxial accelerating cavities. Assemblies of accelerator elements, or lattices, have been modeled as well, and a method for modeling multiple charge state transport using linear matrix methods is also given.

Finally, an experiment studying beam steering induced by QWR resonators is presented, the first systematic experimental investigation of this effect. As mentioned earlier, characterization of this steering on beam properties is important for accurate modeling of the beam transport through the linac. The measurement technique devised at ReA investigates the effect's dependence on the beam's vertical offset within the cavity, the cavity amplitude, and the beam energy upon entrance into the cavity. The results from this experiment agree well with the analytical predictions based on geometrical parameters calculated from on-axis field profiles. The incorporation of this effect into modeling codes has the potential to speed up complex accelerator operations and tuning procedures in systems using QWRs.

ACKNOWLEDGMENTS

To begin with, I could not have accomplished any of this without the guidance of my advisor, Mike Syphers. His instruction and patience were truly essential factors in making me the scientist that I am today. If there is one person I wish to emulate in my career, it is Mike. I can only hope to one day be half the mentor to others that he has been for me.

I also received indispensable advice and guidance from Paul Chu, for which I am deeply grateful. I cannot thank him enough for taking me on as a student who was in need of much direction and guidance, which he provided. He has instilled in me many interests in computing and programming which I plan to pursue throughout my career.

The remaining members of my guidance committee, Sekhar Chivukula, Felix Marti, and Stuart Tessmer, also deserve my thanks for their advice and support throughout the years. In addition, the kind support from Walter Wittmer, Daniela Leitner, Alberto Rodriguez, and Matt Hodek has been amazing. They have all helped me in their own ways throughout my time as a student at MSU, enabling me to grow and develop in a supportive environment. I'm also extremely grateful for Marc Doleans and Oliver Kester, who started me off on my adventure in accelerator physics.

The measurements I took at ReA would not have been possible without the help from its capable operators: Shannon Krause, Randy Rencsok, Sam Nash, Ken Galbraith, Eric Mollon, and Jay Paquette. Larry Tobos kept the LB source behaving throughout the measurements, for which I'm sincerely grateful. I also thank Alberto Facco for his consultation during the calculations preceding these measurements. Xiaoyu Wu, Qiang Zhao, and Mauricio Portillo helped me tremendously with modeling, especially with IMPACT and COSY, and for that I am very thankful.

I am grateful for the assistance from Jack Ottarson, Ben Arend, Don Lawton, and Erin O'Donnell, which led to many of the figures and diagrams in this thesis. I also have the physics graduate secretary, Debbie Barratt, to thank for all of her help on the administrative side. I also have Eduard Pozdeyev and Winter Zheng to thank for their contributions with the solenoid parameterization and cavity field profile data respectively.

I'd also like to sincerely thank my family and friends for their continuous support. My parents especially have always supported me in every endeavor, and my brother keeps me grounded by continuing to beat me in video games. My friends all know the struggles I've been through and have been there to help me throughout them all.

Finally, above all, I'd like to acknowledge my Bradley, who believed in me when I didn't believe in myself. He is the main reason I survived graduate school, and I can never thank him enough for everything he has done for me. Thank you for inspiring me, thank you for believing in me, thank you for supporting me. I am forever grateful.

TABLE OF CONTENTS

LIST OF TABLES	viii
LIST OF FIGURES	ix
Chapter 1 Introduction	1
1.1 NSCL	3
1.1.1 ECR Ion Source	5
1.1.2 Cyclotrons	6
1.1.3 RIB Production	8
1.1.4 Fragment Separator	9
1.1.5 Experimental Stations	10
1.1.6 ReAcceleration Motivation	11
1.1.7 ReA	13
1.2 Future Facilities	15
1.2.1 ReA Upgrades	15
1.2.2 FRIB	16
1.3 Modeling Considerations	18
1.3.1 Modeling Methods	18
1.3.2 Multiple Charge State Transport	20
1.3.3 Quarter Wave Resonator Steering	21
Chapter 2 Review of Beam Physics	22
2.1 Transverse Motion	24
2.2 Longitudinal Motion	28
Chapter 3 Modeling Elements	34
3.1 Quadrupoles	35
3.2 Solenoids	40
3.2.1 Hard-Edge Model Parameterization	45
3.2.2 Solenoid with Corrector	51
3.2.3 Solenoid Error Study	54
3.3 Accelerating Cavities	56
3.3.1 Electromagnetic Fields	57
3.3.2 Energy Gain	59
3.3.2.1 TTF Calculation	60
3.3.2.2 Cavity Geometry	62
3.3.3 Focusing Effects	63
3.3.4 Benchmark Considerations	65
3.3.4.1 TTF Computation	66
3.3.4.2 Thin-lens Modeling	66

3.4	Lattice Examples	68
3.4.1	ReA Linac	69
3.4.2	FRIB Linac Segment 1	69
3.5	Multiple Charge State Transport	71
3.5.1	Background	72
3.5.2	Methodology	73
3.5.3	Benchmark	83
Chapter 4	Quarter-Wave Resonator Steering	86
4.1	Steering Predictions	87
4.1.1	QWR Choice	87
4.1.2	Vertical Steering	90
4.1.3	ReA Calculation	93
4.2	Experiment	96
4.2.1	Procedure	98
4.2.1.1	Vertical Offsets	99
4.2.1.2	Profile Measurement	101
4.2.2	Beam Axis Definition	105
4.2.3	Results and Analysis	106
4.3	Conclusions and Outlook	112
Chapter 5	Conclusions	114
5.1	Summary	114
5.2	Outlook	116
	APPENDICES	117
	Appendix A Additional Cavity Measurement	118
	Appendix B L092 Drive Calibration	121
	BIBLIOGRAPHY	124

LIST OF TABLES

Table 3.1	Analysis Results of Quad Scan Measurement Data (2-24-11)	39
Table 4.1	Summary of cavity steering data at $\beta = 0.036, 0.043, 0.046,$ and 0.051 .111	

LIST OF FIGURES

Figure 1.1	The National Superconducting Cyclotron Laboratory (NSCL) in 2012.	3
Figure 1.2	The NSCL layout highlighting areas of production, fast beams, gas stopping, stopped beams in the low energy area, and reaccelerated beams from ReA.	4
Figure 1.3	ECR schematic, including solenoid and hexapole coils. Microwave power, ω_{RF} , creates the resonance zone in the center, and ion extraction is indicated to the right.	5
Figure 1.4	Cyclotron Schematic, depicting simplified beam path in red, alternating charge on “dees” with beam’s relative position, and magnetic field into the page.	7
Figure 1.5	ISOL production yields at ISOL(DE), the Isotope mass Separator On-Line facility at CERN [7], compared with PF production yields at the NSCL [8]. Note that there are bands of isotopes that are inaccessible in the ISOL production method due to its chemically dependent nature, while projectile fragmentation does not have this limitation. However, ISOL can produce a very intense beams with a higher yield than PF for certain elements.	9
Figure 1.6	A1900 schematic, including four dipole magnets with maximum magnetic rigidity of 6 Tm. Production target, intermediate image, and focal plane locations also indicated.	10
Figure 1.7	ReA layout including the accelerating linac on an elevated platform and the experimental stations on the ground level. The elevated deck design facilitates continuous access for laboratory personnel to other experimental areas.	13
Figure 1.8	Planned layout for Energy Upgrade Phase I: ReA6. Note that additional single-cavity cryomodules have been added downstream from the original linac for longitudinal bunching, as well as an additional $\beta = 0.085$ cryomodule for further acceleration. New experimental detectors will also be commissioned with the construction of ReA6. .	16
Figure 1.9	Facility for Rare Isotopes (FRIB) layout.	17

Figure 2.1	Coordinate System	23
Figure 2.2	Phase space ellipse with negative α (defocusing).	26
Figure 2.3	Phase space transformation of a converging beam along a drift space. After achieving a waist, the converging beam becomes diverging. . .	27
Figure 2.4	Longitudinal motion energy gain is proportional to $\cos(\phi)$. Points of zero energy gain (rebunching mode), stable acceleration (negative phase), and unstable region (positive phase) indicated.	29
Figure 3.1	Left (a): Equipotential surfaces of quadrupole fields plotted for several different voltages. Right (b): The electrodes inside an actual electrostatic quadrupole are shaped along equipotential surfaces in order to produce a pure quadrupole field.	36
Figure 3.2	Left (a): Quad Scan Measurements performed before RFQ at ReA. Solid lines indicate measurement data, while dashed lines indicate SVD analysis. Right (b): Analyzed viewer data for L057QB=-5.5 kV with overlay of beam position and RMS beam size in green. Beam profiles in red are shown above and to the left of the beam spot. . .	39
Figure 3.3	Equivalent hard-edge model for LEBT 0.6 T solenoid located before RFQ. The measured longitudinal field profile is shown with $B_{\max} = 0.6926$ T, while the equivalent hard-edge model consists of a drift section ($B = 0$ T), a constant field section ($B = 0.6010$ T), followed by a second drift section ($B = 0$ T).	41
Figure 3.4	The ReA solenoid L090SN scaled to 1T for $B\rho = 0.5$ T m. The solution that minimized M_{tot} is found to be at $L_e = 0.24$ m, $B_e = 0.8$ T.	46
Figure 3.5	XAL simulation of transverse beamsizes, $\langle x^2 \rangle$ and $\langle y^2 \rangle$, σ_{11x} and σ_{11y} as defined in Equation 3.2, for the ReA Linac without the third cryomodule using the solenoid parameterization defined in Equation 3.25. Vertical dashed lines indicate diagnostic locations. Note that the beam is focused in both x and y at the solenoid locations, and the beam sizes at the third and fourth diagnostic locations, at ~ 6 m and ~ 11 m respectively, are of similar magnitude, which was observed experimentally.	49

Figure 3.6	Numerical method results of B_e vs. L_e shown calculated at various $B\rho$ and B_0 values that cover the relevant ReA ranges. The red regions indicate areas with high divergence between the hard-edge and field-profile models, while the blue regions indicate areas where the two models agree. Note that solutions are present (blue regions exist) for low beam rigidities, $B\rho$, only at low solenoid fields, B_0 . The solution range increases to higher fields at higher rigidities.	50
Figure 3.7	Percent difference between the “full-field” and “thin-lens” models for beamsizes calculated at the solenoid exit, $z = 0.2$ m, as a function of relative corrector field strength, B_y , to the main solenoid field, $B_z = 2$ T.	54
Figure 3.8	FRIB Linac Segment 1 (XAL) with random Gaussian error added to each solenoid. Gaussian errors of about (a)0.5% and (b)1% have been used — note how the RMS of the relative difference in $\sigma_{x,y}$ grows by approximately the percentage of the Gaussian error introduced to the system. It is an important result that this growth levels out without increasing exponentially.	56
Figure 3.9	Cut-away image of the ReA $\beta = 0.041$ QWR cavity type. The two accelerating gaps that the beam travels through towards the bottom of the cavity are shown in detail.	57
Figure 3.10	ReA $\beta = 0.041$ Cavity Fields, including the accelerating electric field, E_z , and the transverse fields B_x and E_y . Note that E_y is very small, and so therefore has been multiplied by ten for the purposes of this graph.	59
Figure 3.11	TTF of $\beta = 0.041$ and $\beta = 0.085$ cavities	61
Figure 3.12	QWR and HWR Cavities [29]. The QWR cavities operate at 80.5 MHz, while the HWR cavities operate at 322 MHz.	63
Figure 3.13	Electric field lines in an RF gap.	64
Figure 3.14	ReA TTF for $\beta = 0.041$ and $\beta = 0.085$ cavities, with operating regimes highlighted. The $\beta = 0.041$ cavities are located in the first two cryomodules, CK01 and CL01, while the $\beta = 0.085$ cavities are located in the third cryomodule, CM01.	67
Figure 3.15	Modeling two gap acceleration in XAL as compared with IMPACT for a $\beta = 0.041$ accelerating cavity.	68

Figure 3.16	Benchmarking results of the ReA linac through its second cryomodule show good agreement between the matrix modeling code XAL, and the multi-particle tracking code IMPACT. Plots show the results for transverse β functions (a) β_x and (b) β_y , longitudinal β function (c) β_z , and finally the kinetic energy per nucleon, (d) E_k	70
Figure 3.17	XAL Cavity Benchmark with IMPACT for a U^{33+} beam through FRIB's Linac Segment 1 to the Stripper Foil, including modeling of $\beta = 0.041$ and $\beta = 0.085$ cavities.	71
Figure 3.18	Results from ANL multiple charge state transport: pepper-pot image of the combined bismuth beam with charge states 20+ and 21+ (on the left) and superimposed images of $^{209}Bi^{20+}$ (blue) and $^{209}Bi^{21+}$ (red) beams transported individually (on the right) [51].	73
Figure 3.19	Multiple Charge State Energy Gain: $\Delta\phi = 0$ on left, $\Delta\phi = \omega_{RF}\Delta t$ on right. As discussed in the text, modeling the separate charge states with $\Delta\phi = 0$ yields the unphysical result where each charge state arrives at the accelerating phase of the reference charge state, resulting in higher charge states receiving higher energy gains and lower charge states receiving lower energy gains than the reference charge state. Instead, each individual charge state's arrival time at each cavity must be calculated in order to correctly model the multiple charge state's energy gain, as seen here on the right.	76
Figure 3.20	FRIB Linac Segment 1 as simulated by XAL for U^{33+} and U^{34+} charge states, as well as the result of the two charge states combined.	80
Figure 3.21	End of FRIB Linac Segment 1 chicane as simulated by XAL for U^{33+} and U^{34+} charge states, as well as the result of the two charge states combined.	81
Figure 3.22	Schematic representation of three beamlets with means μ_i , standard deviations σ_i , and intensities N_i	82
Figure 3.23	Results of XAL and IMPACT calculations for FRIB FS1 to Stripper. The IMPACT results are shown with dashed lines, while the XAL results are shown with the solid lines.	84
Figure 3.24	XAL Schema for adding multiple charge state run capabilities.	85

Figure 4.1	FRIB Quarter-Waver Resonator (QWR) and Half-Wave Resonator (HWR) cavity types shown with optimal β and operational frequencies. The FRIB HWRs are designed for four times the frequency of the QWRs, resulting in their length being about half as long.	88
Figure 4.2	Coaxial Cable Analogy: the beam is accelerated at the open end of the “circuit” where the electric field is maximized, while the magnetic field circulates at the closed end.	89
Figure 4.3	The calculated ReA $\beta = 0.041$ cavity D -factors from Equation 4.6, D_{Bx} , D_{Ey} , and D_{rf} , with $E_a = 16$ MV/m and $\phi = -90^\circ$ along with the sum of the three terms.	93
Figure 4.4	Calculation of $\Delta y'$ vs. β for the ReA (a) $\beta = 0.041$ and (b) $\beta = 0.085$ cavity types, plotted for centered and ± 1 mm vertical offset scenarios. A typical accelerating cavity setting is used: $\phi = -20^\circ$ and $E_a = 16$ MV/m. The beam species is H_2 with $q/A = 0.5$. The x -range for each plot is from $\beta = 0.036$, corresponding to the RFQ energy of 0.6 MeV/u, to $\beta = 0.16$, corresponding to the highest beam energy for H_2 at ReA, 12 MeV/u.	94
Figure 4.5	Left (a): Plot of ReA $\beta = 0.041$ calculation $\Delta y'$ vs. β for offsets $dy = -6, -3, 0, 3,$ and 6 mm. Right (b): $\Delta y'$ vs. cavity amplitude E_a for offsets $dy = -6, -3, 0, 3,$ and 6 mm for beam energy $E_k = 0.6$ MeV/u, corresponding to $\beta = 0.036$	96
Figure 4.6	ReA Layout from 2013, including EBIT charge breeder, Q/A section, commissioning source, room temperature RFQ and superconducting linac including two cryomodules containing $\beta = 0.041$ accelerating cavities. Note the drift tube after the second cryomodule is the location for the third cryomodule containing $\beta = 0.085$ accelerating cavities, to be installed.	97
Figure 4.7	Schematic of ReA Linac as commissioned in 2013, before the installation of the third cryomodule. Square elements represent superconducting solenoids, while circular elements represent quarter-wave resonators. The drift space between the diagnostics after the second cryomodule is ~ 5.2 m.	99

Figure 4.8	Beam position at cavity midpoint as projected from measurements at two downstream locations. Error bars are the RMS beam size. Note the improvement of the vertical separation and consistency of horizontal position achieved with the 10-29 data set which utilized the response matrix measurement technique.	100
Figure 4.9	45° Beam Profile Diagnostic setup. In the top left, the plate is shown with three slits and one aperture in the order that they intercept the beam during the profile scans: (1) the horizontal slit measuring the vertical beam profile, (2) the 45° slit for a measure of the coupling between the x and y planes, (3) the vertical slit measuring the horizontal beam profile, and (4) the 5 mm aperture for beam tuning.	102
Figure 4.10	Plots of beam current vs. slit position for raw data from 45° slit scan taken at (a) L092 and (b) L110, and the Gaussian fit results for beam position and RMS beam size. Note that the 45° plate at L110 does not have the 45° slit, which accounts for the missing peak in (b). . .	103
Figure 4.11	45° Beam Profile Diagnostic Plate shown with distances from Equation 4.12, d_{ref} and d_{offset} , labeled.	104
Figure 4.12	Schematic diagram of relevant measurement quantities depicting the difference between the diagnostic axis and the cavity center axis. . .	105
Figure 4.13	Plots of $\Delta y'$ vs. E_a for beam energies (a) $E_k = 0.6 \text{ MeV/u}$ ($\beta = 0.036$), (b) $E_k = 0.85 \text{ MeV/u}$ ($\beta = 0.043$), (c) $E_k = 1.08 \text{ MeV/u}$ ($\beta = 0.046$), and (d) $E_k = 1.24 \text{ MeV/u}$ ($\beta = 0.051$). Lines correspond to the predicted response calculated using cavity design data and experimental conditions.	108
Figure 4.14	Left (a): Plot of $\Delta y'/E_a$ vs. y at the midpoint of the test cavity, including each measurement data set. Note the agreement in the slopes for the different energies. Right (b): Plot of $\Delta y'/E_a$ vs. β including each measurement data set.	110
Figure 5.1	Left (a): Raw experimental data of $\Delta y'$ vs. E_a at $E_k = 0.6 \text{ MeV/u}$ ($\beta = 0.036$). Right (b): The same data set with a constant vertical offset, $\delta = 1.29 \text{ mm}$, applied during the analysis.	115

Figure A.1 Final measurement of L091 data set on 10-31. The $E_a = 0.5$ MV/m L092 data point had all peaks shifted by the same amount. The dashed lines indicate where this overall shift has been manually accounted for in the analysis. L110 data indicates it was an issue with the L092 drive, not a sudden change in the beam, for instance from an instability in the LB source. 119

Figure A.2 Plot of $\Delta y'$ vs. E_a for beam energies $E_k = 1.08$ MeV/u ($\beta = 0.046$). Lines correspond to the predicted response calculated using cavity design data and experimental conditions. 120

Chapter 1

Introduction

Advanced accelerator systems today require sophisticated computer simulations to develop a complete understanding of their operation and functionality due to the increasing complexity of the involved systems. Real-time control and modeling, more now than ever before, are steadily becoming essential components in the operation of accelerators in order to enhance performance.

Accelerator physics is concerned with the creation of beams of particles, their acceleration, and subsequent transport to experimental detectors. During transport, beam manipulation and advanced diagnostic techniques often demand accurate modeling in order to fully understand the accelerator and beam properties to ultimately achieve the necessary requirements for state-of-the-art experiments.

The degree of detail incorporated into these accelerator models is primarily a function of the particular needs of the application the model is serving. There are many different types of accelerator facilities around the world that cover a wide variety of research goals, each having its own unique modeling challenges. Synchrotron light sources utilize high energy electron beams in a storage ring to study topics in materials science and condensed matter physics. High energy proton synchrotrons or linear colliders are used to study subatomic particles in high energy physics. Low to medium energy beams of heavy nuclei are important for nuclear physics experiments, as in the case for Michigan State University's National Superconducting

Cyclotron Laboratory (NSCL).

Accelerators in nuclear physics, such as the NSCL and the Facility for Rare Isotope Beams (FRIB), alter the particle species and energy ranges used to study the vast nuclear landscape. These constantly changing conditions, which accelerators must be designed to accommodate, motivate the necessity of accurate modeling methods in real-time in order to improve accelerator tuning procedures and minimize the operational down-time when switching between beams.

Additionally, new devices need to be properly characterized in order to be incorporated accurately into modeling codes. It is especially important to correctly characterize the effect that elements have on steering of the beam when considering accelerator tuning. In the case that an effect is observed but not yet incorporated into present modeling codes, detailed systematic measurements should be made in order to verify its correct description. One prime example of this is the Quarter-Wave Resonator (QWR) steering experiment performed at the ReA facility at the NSCL, which will be presented in greater detail in the following chapters.

To begin with, though, this introductory chapter presents an overview of the accelerators that will appear throughout this dissertation, focusing on the NSCL in Section 1.1. A background of future facilities of interest is included in Section 1.2. Within a brief summary of the different methods used for modeling these accelerators in Section 1.3, topics which provide unique challenges to the modeling of modern low-energy heavy ion accelerators, including QWR steering, are introduced.

1.1 NSCL

The National Superconducting Laboratory (NSCL) has been a highly successful laboratory for doing world class nuclear research over the past three decades. By commissioning the new reaccelerator, ReA, the lab continues to push the boundaries for nuclear research and expand its capabilities to provide rare isotopes at relevant energy regimes for experimenters. In the future, the Facility for Rare Isotope Beams (FRIB) will replace the coupled cyclotrons with a high power driver linac to become the preeminent facility for nuclear research in the world.

The NSCL, as shown in 2012 in Figure 1.1, is located at Michigan State University (MSU). The NSCL currently consists of a stable Electron Cyclotron Resonance (ECR) ion source, SuSI (the Superconducting Source for Ions), two coupled superconducting cyclotrons, the K500 and the K1200, and the A1900 fragment separator.



Figure 1.1: The National Superconducting Cyclotron Laboratory (NSCL) in 2012.

Experimental stations at the NSCL are categorized by the energy of the beams that they use. High energy experiments take beam directly from the A1900, while low energy experiments are delivered beam from the gas stopping stations.

In addition to the NSCL's coupled superconducting cyclotrons which provide the primary beam on target, another accelerator has also been built on site to reaccelerate rare isotopes,

ReA. The original design for ReA includes accelerating components capable of reaccelerating beams of uranium up to 3 MeV/u. The gas stoppers also provide beam to ReA which delivers re-accelerated beams to its dedicated experiments.

The components of the NSCL to be discussed in further detail are shown in the schematic layout in Figure 1.2, including the ion sources, cyclotrons, fragment separator, experimental stations, and the reaccelerator, ReA. The highlighted regions show the areas of fast beams, gas stopping, stopped beams in the low energy area, and reaccelerated beams.

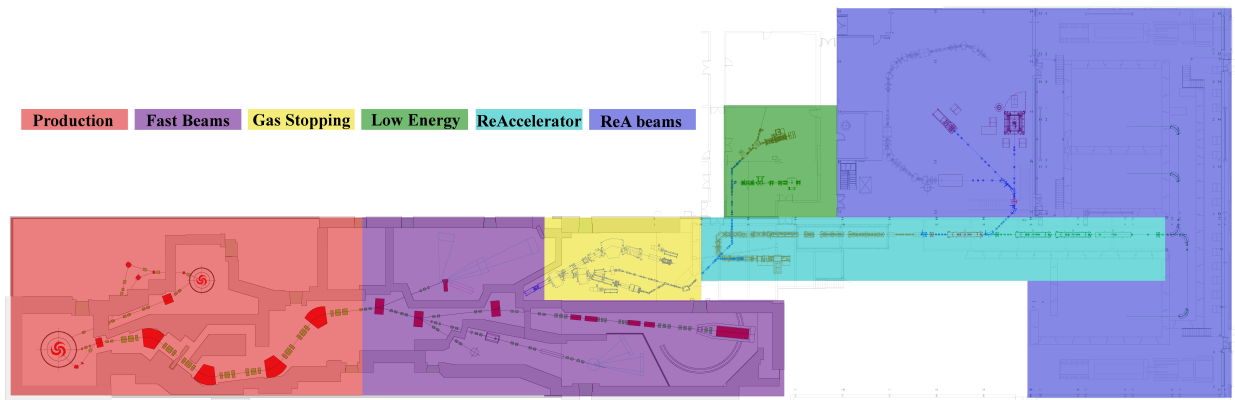


Figure 1.2: The NSCL layout highlighting areas of production, fast beams, gas stopping, stopped beams in the low energy area, and reaccelerated beams from ReA.

The particle beam path begins in an ion source, continuing through the cyclotrons and the fragment separator, the production area of Figure 1.2. It then proceeds to travel to either the fast beam area for fast beam experiments, or the gas stopping area. After the gas stopping area the beam is transported to either the stopped beam experiments or the reaccelerator, ReA, where it can be reaccelerated to its dedicated experiments. The reacceleration approach allows intermediate energies to be attained, as will be explained further in Sections 1.1.6 and 1.1.7.

1.1.1 ECR Ion Source

Stable beams are first produced by SuSI, a superconducting Electron Cyclotron Resonance (ECR) source capable of achieving very intense and highly charged beams, for example more than $380 e\mu\text{A}$ of Xe^{26+} [1]. The SI unit for current is the Ampere (A), which is defined as a Coulomb per second (C/S). When describing beams from ECRs, this unit is typically cited as an electrical amp (eA), which includes the charge state of the beam. The current of the beam as measured on a Faraday Cup, for instance, is measured in electrical Amps (eA). If the particle current is being discussed, this is defined as the electrical current divided by the charge state.

ECRs produce these highly intense beams by resonantly exciting electrons in the plasma with cyclotron frequency $\omega_{\text{RF}} = \frac{qB_{\text{ECR}}}{m}$, where q and m are the charge and mass of an electron, B_{ECR} is the resonant magnetic field, and ω_{RF} is the cyclotron frequency. A schematic of the SuSI plasma chamber is shown in Figure 1.3.

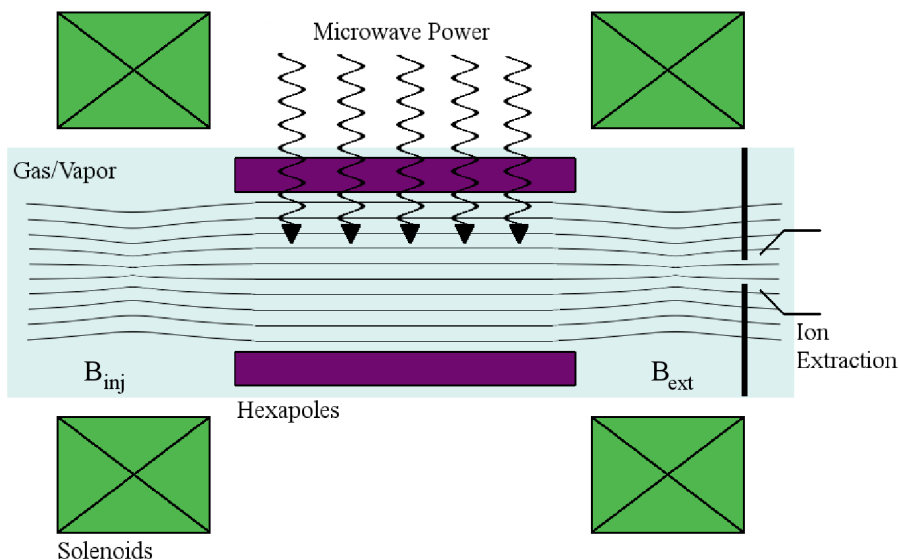


Figure 1.3: ECR schematic, including solenoid and hexapole coils. Microwave power, ω_{RF} , creates the resonance zone in the center, and ion extraction is indicated to the right.

The microwave power heats the electrons, which in turn ionize the neutral gas or metal vapor atoms, increasing the charge state of the desired element. SuSI operates at a microwave frequency of $f_\mu = 18$ GHz, corresponding to a resonant magnetic field of $B_{\text{ECR}} = 0.64$ T.

The plasma inside an ECR is confined axially by solenoid fields: in SuSI on the injection side $B_{\text{inj}} \approx 4B_{\text{ECR}}$ and on the extraction side $B_{\text{ext}} \approx 2B_{\text{ECR}}$. The plasma is confined radially through a hexapole field, where $B_{\text{rad}} \approx 2B_{\text{ECR}}$. All magnets in SuSI are superconducting, which reduces the power consumption and also allows for tunable radial magnetic fields, an advantage over permanent hexapole magnets used in room temperature ECRs [2]. Once the desired charge state is reached, the ions are extracted from the magnetic bottle by applying a voltage to the extraction electrodes [3] and transported to the cyclotrons for acceleration.

1.1.2 Cyclotrons

The K500 was the first ever superconducting cyclotron. A schematic of a cyclotron is shown in Figure 1.4. The name derives from the energy that a proton beam could potentially be accelerated to, 500 MeV. Heavy ion beams have protons and neutrons in the isotope’s nucleus which contribute to their mass. Because of this it is common to cite an energy per nucleon instead of the total beam energy. The K500 is capable of accelerating heavy ion beams up to 17 MeV per nucleon, or 17 MeV/u. The total beam energy is recovered by multiplying this value with the total number of nucleons.

The beam from the ion source is injected into the center of the cyclotron, where it is then accelerated by an alternating electric field between the “dees”. The first cyclotron accelerators had two electrodes, and were so named “dees” for their “D”-shaped electrodes. Both the K500 and the K1200 have three “dees”. To utilize the acceleration through these electrodes multiple times, a static magnetic field is applied.

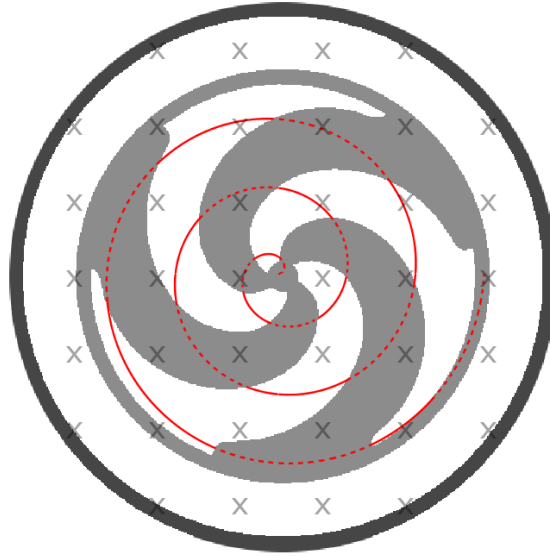


Figure 1.4: Cyclotron Schematic, depicting simplified beam path in red, alternating charge on “dees” with beam’s relative position, and magnetic field into the page.

The ions spiral through this field, with increasing radius $r = \frac{mv}{|q|B}$ as their energy increases. Here m , q , and v , are the mass, charge, and velocity, of the ion beam respectively. B is the magnetic field of the cyclotron. The accelerating voltage is applied to the “dees” at the cyclotron resonance frequency of the beam, $f = \frac{|q|B}{2\pi m}$ which results in the beam experiencing an accelerating electric field through each of the gaps between the electrodes. Once the particles’ radius reaches the radius of the cyclotron, the accelerated beam is ejected.

The K500 was the NSCL’s main accelerator from 1982 to 1989, when it was replaced with the K1200 cyclotron which operated until 1999, when the cyclotrons were coupled [4]. This configuration, known as the coupled cyclotron facility (CCF), allows for much higher energies to be achieved, because a stripper foil is utilized before injection into the K1200. This yields a higher charge state, and in turn a more efficient acceleration is achieved through the K1200 acceleration. The K1200, the larger of the two cyclotrons, can then accelerate ions to a range of energies, from 20 (MeV/u) to 200 MeV/u [5].

1.1.3 RIB Production

The fast beams of rare isotopes at the NSCL are produced through a process called Projectile Fragmentation (PF). The stable high energy ($\sim 200\text{MeV/u}$) ion beam from the cyclotrons is impinged on a thin light production target, such as Beryllium, to produce rare (radioactive) isotope beams (RIBs).

The nuclear reactions inside the target foil at relatively high energies remove a significant amount of nucleons to produce a shower of particles with less mass than that of the projectile and target nuclei. A fraction of the beam reacts with the target, producing rare isotopes lighter than the beam element in a statistical process. By using a heavy beam of an element such as Uranium, many rare isotopes can be produced this way [6].

Another production method for rare isotope beams is called Isotope Selection On-Line, or ISOL, which is a chemically dependent process in which a high energy beam is impinged on a thick target where the rare isotopes diffuse out of the target and are then subsequently accelerated. This process can take on order of microseconds, so for rapidly decaying beams projectile fragmentation is the necessary production method. Because of ISOL's chemically-dependent nature, it may also be necessary to produce certain beams with projectile fragmentation, as seen in Figure 1.5. The isotopes capable of being produced at the NSCL's CCF is shown on the right in Figure 1.5.

Projectile fragmentation (PF) has the advantage that it is a chemically independent process and avoids this limitation of ISOL production. However, as PF is a statistical process, with RIBs farther from stability produced at slower rates, separation of the many different reaction products is necessary in order to form a beam of one desired species.

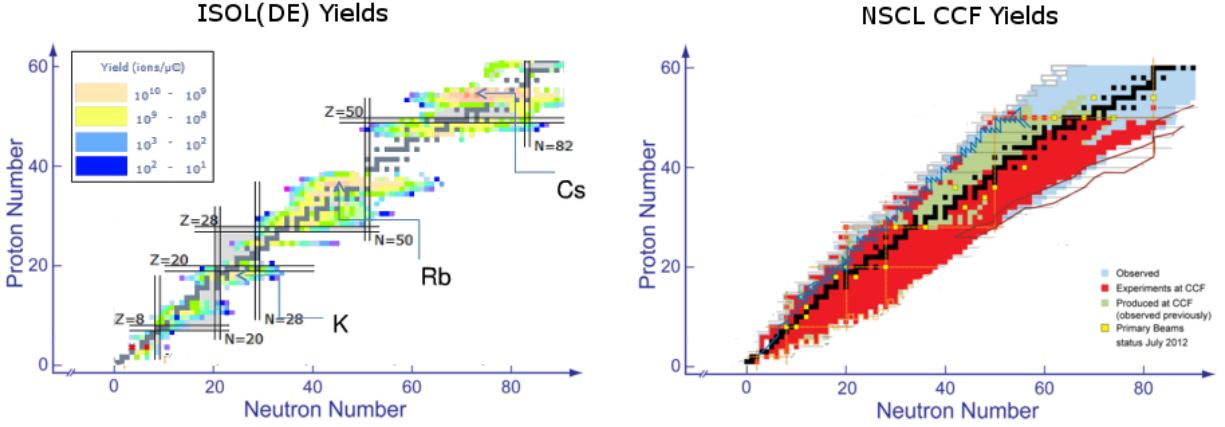


Figure 1.5: ISOL production yields at ISOL(DE), the Isotope mass Separator On-Line facility at CERN [7], compared with PF production yields at the NSCL [8]. Note that there are bands of isotopes that are inaccessible in the ISOL production method due to its chemically dependent nature, while projectile fragmentation does not have this limitation. However, ISOL can produce a very intense beams with a higher yield than PF for certain elements.

1.1.4 Fragment Separator

The A1900 fragment separator at the NSCL, seen in Figure 1.6, uses several methods to efficiently separate a desired isotope beam from the many reaction products created through the PF production method [9]. Its name is derived from “A” for Analysis, and 1900 for the maximum proton kinetic energy in MeV that can be bent by its four dipole magnets.

The first method for isolating the desired RIB utilized by the A1900 is magnetic separation. The dipole magnets disperse the beam according to its momentum to charge ratio, defined as the magnetic rigidity, $B\rho = p/q$. Since the velocities of the different species are fairly similar, this amounts to essentially a selection by mass-to-charge ratio.

This reduces the number of species considerably, but there are still many RIBs with the same A/Q ratio, so further separation is needed. Selection by proton number (Z) is performed by placing a degrader at the intermediate image location (I2 in Figure 1.6) at the center of the A1900. As energy loss in matter is Z -dependent, as given by the Bethe-Bloch

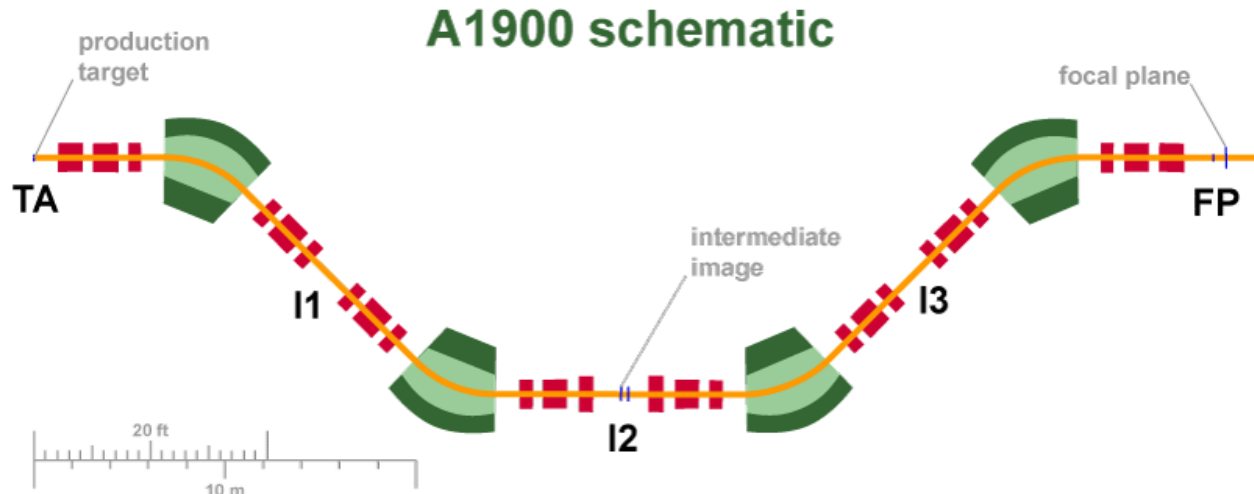


Figure 1.6: A1900 schematic, including four dipole magnets with maximum magnetic rigidity of 6 Tm. Production target, intermediate image, and focal plane locations also indicated.

equation [10], the velocity of the different RIBs changes as a function of their charge alone, which allows them to then be separated out by their magnetic rigidity, $B\rho$.

1.1.5 Experimental Stations

After particle fragment separation, there are several different experimental stations to which the RIB may be delivered. Experiments requiring high energies receive the beam directly from the A1900. These experiments use various detectors including the Modular Neutron Array and Large Multi-Institutional Scintillator Array (MoNA-LISA) [11], the High Resolution Array Detector (HiRA) [12], and the S800 Spectrograph [13] to study nuclear reactions and properties such as half-life, cross-sections, and branching ratios which all require fast beams.

Other experiments probe nuclear properties that require low energy beams, such as measuring the mass as done with the Low Energy Beam and Ion Trap (LEBIT) [14], or for nuclear magnetic resonance (β -NMR) studies, as performed with the Beam Cooler and Laser spectroscopy (BECOLA) [15]. The fast beams from the cyclotrons must therefore have their energy reduced before being transported to these low energy experiments.

The majority of the beam's energy is lost through a solid degrader, followed by further beam cooling in a gas cell filled with an inert gas, such as Helium. Beam cooling in this context refers to the reduction of beam energy due to collisions in the gas which essentially stop the beam. Once this is accomplished, the beam can then be extracted from the gas cell. This process reduces the energy spread of the beam and its area in phase space, or emittance, to an acceptable level for the high-precision low-energy experiments [16]. A new type of gas stopper, called the Cyclotron Gas Stopper, is currently in the process of being assembled and commissioned. The goal for this new gas stopper is to have higher efficiencies for lighter beams than the current linear gas cell [17].

Other nuclear experiments, particularly those of interest in nuclear astrophysics, require higher energies than the stopped beam experiments. The desired range of energies, from ~ 0.33 - 3 MeV per nucleon, is of scientific interest because these are the typical energies that exist in stars. This demand from the nuclear science community drove the decision to design the ReA facility to re-accelerate heavy rare isotope beams to 3 MeV/u [18]. There also remains interesting nuclear physics to probe at slightly higher energies at or above the Coloumb barrier, for which upgrades to ReA6 and ReA12 have also been proposed for the future.

1.1.6 ReAcceleration Motivation

Before the construction of the ReA facility, the NSCL was capable of providing fast (~ 200 MeV/u) rare isotope beams as well as low energy beams (~ 1 eV/u) through its gas stopping station.

These two energy regimes are necessary for studying different nuclear reactions and different properties of the nucleus. For example, higher energy beams are required to produce

transfer reactions. Inverse kinematics, using a heavy beam on a light target, can then be used to measure the $B(E2)$ value which is important in nuclear physics.

High energy beams are also used to study the symmetry energy term in the nuclear equation of state, as well as many other properties of the nucleus. The S800, GRETINA and MONA are some of the experimental stations that use high energy beams at the NSCL. On the other hand, low energy beams are necessary for other types of high precision measurements that are performed at LEBIT and BECOLA which measure the mass and hyperfine structure of the nucleus respectively.

With the addition of the ReA facility, the NSCL has added a new energy region at $\sim 3\text{-}12\text{ MeV/u}$ and now is capable of providing beams in the low, mid-range, and high energy range for nuclear physics experiments. This mid-range region of energy is of interest especially for nuclear astrophysics reactions as well as some other experiments that are well suited in this region. When the facility is upgraded with additional cryomodules (in planning) the energy range will cover physics just above the Coulomb barrier, which is again especially of interest to nuclear astrophysics.

Fast rare isotope beams are produced and slowed down and then reaccelerated to reach the desired energy. This process is necessary in order to preserve the emittance, or phase-space quality, of the beam. The beam cannot be slowed immediately to the desirable mid-range energy, as the emittance would grow to a point where it would not be able to be transported. Even if a degrader is placed immediately before the experiment, this would not provide good cross sections with the large emittance.

It is therefore favorable to slow down the beam in a solid degrader where the beam loses over 95% of its energy, followed by a gas cell where collisions with inert gases reduce its energy further. The ions will not neutralize completely during the collisions with the buffer

gas atoms if the buffer gas has a very high ionization potential — typically a noble gas is chosen for this role as its filled outer electron shell make these gases extremely inert. This leaves a singly-charged beam that can then be extracted and reaccelerated. The ReA facility also includes an Electron Beam Ion Trap (EBIT) which increases the beam’s charge state, or charge breeds the beam, for more efficient re-acceleration.

1.1.7 ReA

The ReA facility, shown in Figure 1.7, consists of an Electron Beam Ion Trap (EBIT), a charge to mass or Q/A selection section, a normal conducting RFQ, a superconducting linac, and transport beam lines that deliver the beam to the experiments [19]. The beam optics designs were developed using COSY [20] and IMPACT [21].

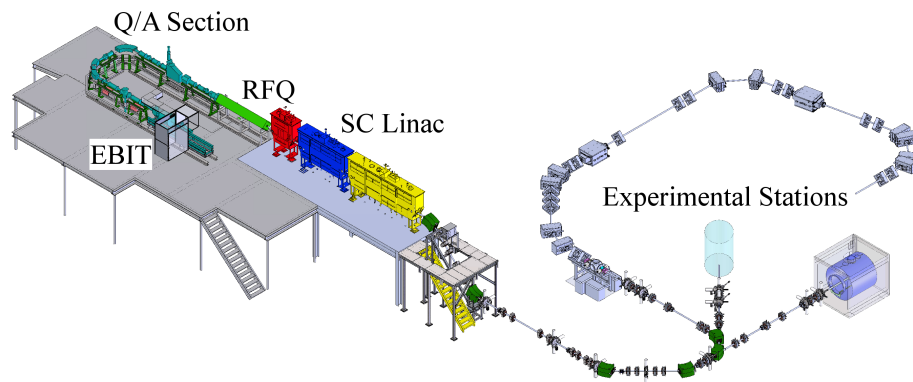


Figure 1.7: ReA layout including the accelerating linac on an elevated platform and the experimental stations on the ground level. The elevated deck design facilitates continuous access for laboratory personnel to other experimental areas.

Gas-stopped beams are typically singly ionized. In order to achieve more efficient acceleration, these beams are injected into the ReA Electron Beam Ion Trap (EBIT) for charge breeding. An EBIT uses a magnetic bottle to confine the ions that it collects, while a

high-density electron beam increases the charge state of the ions by stripping away outer-shell electrons, similar to the mechanism of an ECR [22]. Once the desired charge state is reached, the highly charged ions are ejected from the trap.

An achromatic mass separator consisting of an electrostatic sector and a magnetic sector provides a mass resolving power of $R \sim 100$ and energy spread of $\delta_E = 2\%$ [23]. A small longitudinal emittance is attained by using a Multi-Harmonic Buncher (MHB) before acceleration [24]. The MHB excites up to three harmonics, approximating a Sine wave, in order to bunch the beam for acceptance into ReA's accelerating elements.

The accelerating components of ReA include a normal conducting room temperature Radio-Frequency Quadrupole (RFQ) [25], and three cryomodules with two types of superconducting quarter-wave RF cavities operating at 80.5 MHz [26]. The maximum final energy achievable in this first stage of ReA is 3 MeV/u for heavy nuclei such as uranium, and 6 MeV/u for ions with $A \leq 50$.

The ReA facility at the NSCL has the capability to provide low energy rare isotope beams which are typically difficult to produce at Isotope Separation On-Line (ISOL) facilities. As mentioned in Section 1.1.3, ISOL facilities produce RIBs at rest by impinging a high-energy stable beam on a thick production target. The rare isotopes then diffuse out of the target where they can subsequently be accelerated to the desired energy.

Due to the individual chemistry of each species and target ion source, however, some beams are extremely difficult to produce at the necessary rate for experiments [27]. The ReA facility can take advantage of the chemically-independent projectile fragmentation production method at the NSCL to offer experimenters beams at energies that were previously unavailable.

1.2 Future Facilities

There are many exciting developments planned for the future of the NSCL. Following is a brief summary of these proposals for the future facilities at MSU, including upgrades to the existing reaccelerator and an entirely new primary driver linac to replace the coupled cyclotrons with the Facility for Rare Isotope Beams.

1.2.1 ReA Upgrades

High-quality low-energy beams are extremely desirable in the experimental nuclear physics community. With ReA able to achieve 3 MeV/u beams, many of these low-energy reactions for nuclear astrophysics can be studied. These reaction measurements occur at astrophysical energies, and ultimately motivated the construction of ReA. However, as alluded to earlier, many experiments need slightly higher energies, still well below the energies of the fast beams at production (~ 100 MeV/u).

Some of these experiments include the study of transfer reactions of exotic nuclei, multi-step Coulomb excitation, and nuclear shell structure evolution far from stability, which all require reactions with very short-lived beams at energies around 6-12 MeV/u. Energy upgrades to ReA have therefore been planned in stages, titled ReA6 and ReA12, which will reaccelerate the rare isotope beams to 6 and 12 MeV/u respectively. The layout for ReA6 is shown in Figure 1.8.

The energy upgrade for ReA6 will require four additional cryomodules, three single-cavity cryomodules for longitudinal matching and rebunching, and one cryomodule with 8 accelerating cavities [28]. This cryomodule will be identical in design to the cryomodules designed for FRIB. Drift space after this cryomodule is left during this phase for the second

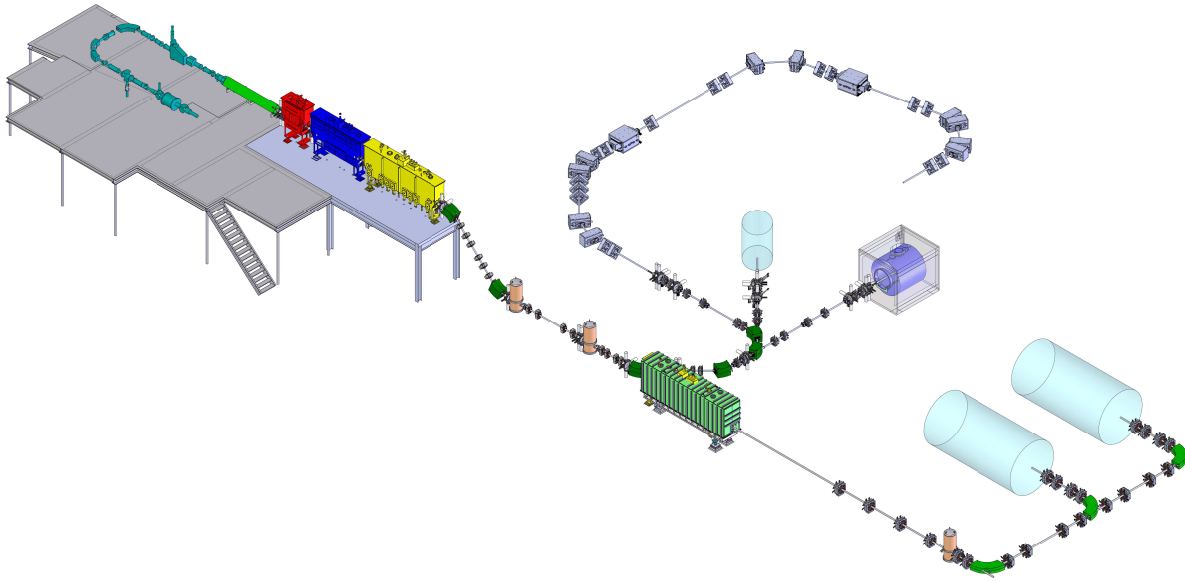


Figure 1.8: Planned layout for Energy Upgrade Phase I: ReA6. Note that additional single-cavity cryomodules have been added downstream from the original linac for longitudinal bunching, as well as an additional $\beta = 0.085$ cryomodule for further acceleration. New experimental detectors will also be commissioned with the construction of ReA6.

energy upgrade to ReA12 which requires an additional two accelerating cryomodules.

1.2.2 FRIB

The Facility for Rare Isotope Beams, FRIB, will take the place of the coupled cyclotrons at the NSCL as the primary beam accelerator. The plans for FRIB also include a new high power target station. After the target, the A1900 fragment separator will be reconfigured to deliver the secondary beam to existing experimental stations as well as additional detectors designed specifically to use beams from FRIB [29]. The configuration can be seen in the schematic layout of Figure 1.9.

The low- β ($\beta = v/c$) portion of FRIB linac utilizes Quarter-Wave Resonators (QWRs), similar to the accelerating cavities of ReA. This fact reinforces the importance of understanding

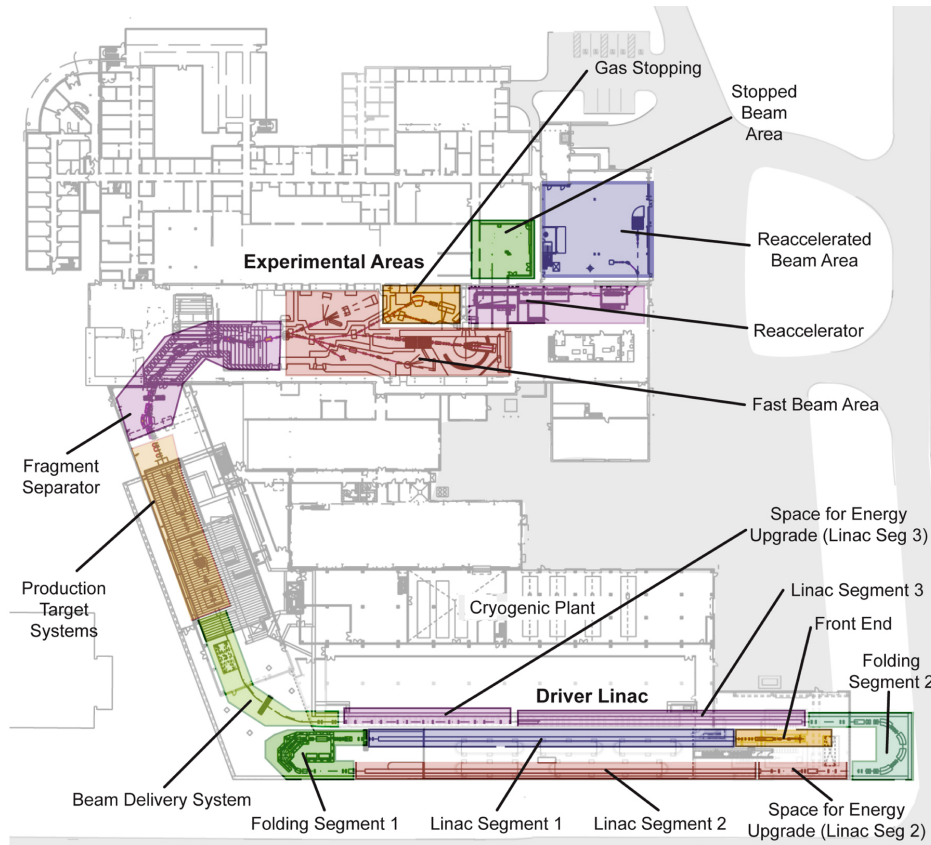


Figure 1.9: Facility for Rare Isotopes (FRIB) layout.

the performance, and characterizing the behavior, of these QWR type cavities. This topic which will be explored in more detail in later chapters.

FRIB will increase the beam power by a factor of ten, from the $\sim 40\text{kW}$ on target at the NSCL currently to $\sim 400\text{kW}$ on target with the final FRIB design parameters. One way to accomplish this is to increase the current, as beam power is a product of beam current and electric potential.

State-of-the-art ECRs are able to provide the necessary increased current, but the possibility exists to dramatically increase the beam current by accelerating multiple charge states at once, as discussed in Section 3.5. By accelerating multiple charge states simultaneously, the total beam current can be increased by almost a factor of five [29].

Many upgrade paths have also been incorporated into the design of FRIB in order to extend its longevity [30]. There is the possibility for an upgrade to include a 1 GeV ISOL facility that would produce certain primary beams at higher intensities than can be achieved with the chemically-independent projectile fragmentation method.

Space has also been left vacant in the accelerator tunnel for additional cryomodules to be added for future energy upgrades. Integrating the design of future upgrades into the project plan ensures FRIB will continue to be at the forefront of nuclear physics research for years to come.

1.3 Modeling Considerations

There are unique challenges that accelerators, such as ReA and FRIB, face which require both in-depth modeling for detailed studies and fast online modeling to facilitate beam tuning. Some typical accelerator modeling methods are introduced in Section 1.3.1, followed by the introduction of some of these unique challenges: multiple charge state transport in Section 1.3.2 and Quarter-Wave Resonator (QWR) steering in Section 1.3.3.

1.3.1 Modeling Methods

There are different methods available for modeling accelerators, including multi-particle tracking codes and beam envelope calculations using matrix based transport codes. The appropriate modeling method depends on the beam properties being studied.

Tracking individual particles through magnetic and electric fields of elements of the accelerator takes the result from those hundreds of thousands of particle runs together to simulate the beam. This multi-particle tracking method is excellent for designing machines

as it considers higher order effects, and can take into consideration misalignments and other errors and uncertainties.

Instead of tracking particles individually, the beam can be considered as a “macro-particle” in which the calculated envelope is actually the RMS extent of particles that make up the beam. By considering the beam statistically, its various statistical moments can be propagated, some of which in turn are observables that can be measured with beam diagnostics. Each element in the accelerator is represented by a first order matrix which acts upon the beam. The matrices are multiplied together to get a model of the full accelerator.

Before choosing a modeling method, it is always important to first establish that the relevant physics phenomena are being appropriately described. Only once the correct physics is incorporated into the model can accurate results expect to be gained. To this end, it is essential that the limitations of each modeling method is understood. Small-angle approximations or linearity assumptions are often used to simplify complicated systems. These descriptions are often valid when characterizing first-order effects, but care must be taken for interpretations not to exceed the limits that each model presents.

Computational resources and restrictions are another factor to consider when choosing an appropriate modeling method. Multi-particle tracking codes are able to provide a very detailed description of the beam, but they also have a proportionally high demand computationally. While envelope or single particle tracking may provide less detail, they are very fast methods that can be used in on-line modeling applications. This is especially important when it is necessary to model multiple different ion species through the accelerator, as with the NSCL and FRIB.

Many beam properties can be studied with a simple linear model, but as mentioned previously, some phenomena require more detailed modeling. For instance, higher order effects

such as field non-linearities and beam-beam effects are typically studied with multi-particle tracking codes which can model 3-D fields, while matrix-based transport codes are sufficient for studying linear motion.

The focus of this dissertation will be based in matrix-based transport modeling, as presented in Chapter 2. Many elements can be studied with this method of modeling, and benchmarking efforts confirm its accuracy when compared with multi-particle tracking codes, as shown in Chapter 3. The modeling codes used throughout include XAL [31], IMPACT [32], and COSY [33]. XAL is a linear matrix-modeling code, IMPACT is a particle tracking code, and COSY is a higher-order matrix transport model.

1.3.2 Multiple Charge State Transport

The high intensities required on target in order to produce the desired beam rates of extremely rare isotopes for nuclear experiments at facilities such as FRIB may be difficult to achieve even using state-of-the-art ECR (electron cyclotron resonance) ion sources. The transport of two or more charge states simultaneously provides a method by which the high intensities required by FRIB may be attained; however, this is a great technical challenge to attempt, and requires much study and simulation in order to ensure that the multiple charge state transport scheme is practical and realistic in its objectives.

Multiple charge state beam transport has typically been modeled through multi-particle tracking codes which can take a considerable time to run. In order to model multiple charge state beams in real-time with an online model, a fast modeling method must be established and benchmarked. This topic will be examined in more detail in Chapter 3 along with a brief summary of the history of multiple charge state transport.

1.3.3 Quarter Wave Resonator Steering

Another challenge facing linac accelerators of heavy ions is to include the steering from Quarter Wave Resonators into the modeling of these cavity types. The asymmetry of the QWRs leads to a vertical kick of the beam, even when the beam enters the cavity centered on-axis. Despite this steering effect, QWRs are the preferred cavity type for low- β acceleration, as will be discussed further in Section 4.1.1.

With respect to accelerators, “steering” is typically thought of as originating from field errors, or possibly misaligned beam line elements. In the case of QWRs used in the low- β portion of the linacs of ReA and FRIB, the steering is inherent in the design of the cavity, meaning even on-axis particles will be steered. Although design considerations can be made to mitigate this effect, simpler cavity geometries may still be preferable for the advantages they provide by way of cost and time saving in production. Moreover, these design alterations may not entirely eliminate this effect for all beam conditions and velocities. Therefore a predictive model to study this effect is desired.

Currently this effect is counteracted through the use of vertical and horizontal correctors installed before and after the cavities. The steering had not yet been measured experimentally to verify the theoretical predictions, or added to online models for tuning purposes. The first measurement data of this effect is presented in Chapter 4, with concluding remarks given in Chapter 5.

Chapter 2

Review of Beam Physics

Fundamental accelerator physics concepts are briefly introduced in this chapter for reference in further discussions. Transverse and longitudinal beam physics principles are presented, followed by a summary of the modeling methods used throughout this work.

In modeling the behavior of charged particles through an accelerator, the motion is determined by the Lorentz force which the particles experience when passing through the electromagnetic fields of the beam line elements. The equation of motion for a particle of charge q with velocity \vec{v} in fields \vec{E} and \vec{B} is therefore given by the following formula:

$$\frac{d\vec{p}}{dt} = q \left(\vec{E} + \vec{v} \times \vec{B} \right). \quad (2.1)$$

The electric and magnetic fields must satisfy Maxwell's equations, where boundary conditions are given by the beam line composed of electromagnetic elements. It is often useful to describe the motion of particle beams in terms of their transverse motion, perpendicular to the direction of transport, and longitudinal motion, along the direction of transport.

In Figure 2.1, transverse motion corresponds to momentums p_x and p_y , while longitudinal motion corresponds to p_z . A moving frame of reference with respect to a reference particle along the ideal trajectory, s , is used for a coordinate system.

These coordinates define the position of a particle in an accelerator as a six dimensional

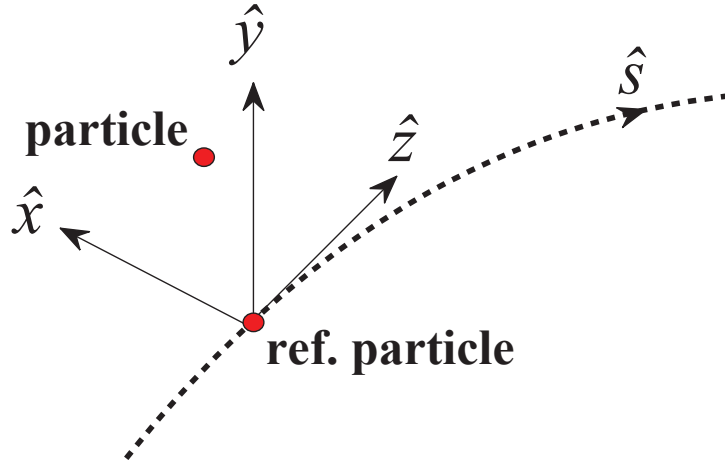


Figure 2.1: Coordinate System

vector as given in Equation 2.2, where primes denote derivatives with respect to s , and $\delta = \frac{\Delta p}{p_{\text{ref}}}$, the normalized difference in longitudinal momentum of the particle with respect to the reference particle.

$$\vec{U} = \begin{pmatrix} x \\ x' \\ y \\ y' \\ z \\ \delta \end{pmatrix} \quad (2.2)$$

With the coordinates established, particle dynamics can now be explored. Independent transverse and longitudinal motions are introduced in Sections 2.1 and 2.2 before considering coupling between the two motions, such as in the case of solenoids, discussed in Chapter 3.

2.1 Transverse Motion

Solving for the transverse linear motion of particle beams yields a solution that takes the form of a harmonic oscillator with its damping constant dependent on the position s in the beam line, as derived in [34]. This is exactly the form of the solution to Hill's equation, a linear second-order differential equation that has been studied since the nineteenth century.

$$x'' + K(s)x = 0 \tag{2.3}$$

Hill's equation, given by Equation 2.3, essentially describes a harmonic oscillator with a position-dependent spring constant, $K(s)$. This motivates the choice to let x take the following form, where ω and ψ are functions of s :

$$x(s) = A_1\omega(s) \cos(\psi(s)) + A_2\omega(s) \sin(\psi(s)). \tag{2.4}$$

Solving for x'' and plugging into equation 2.3 results in

$$(A_1C_2 + A_2C_1) \cos(\psi) + (-A_1C_1 + A_2C_2) \sin(\psi) = 0 \tag{2.5}$$

where

$$C_1 = \omega\psi'' + 2\omega'\psi' \tag{2.6}$$

$$C_2 = \omega'' - \omega(\psi')^2 + K\omega. \tag{2.7}$$

In order for the formula to remain valid for all values of s , the coefficients in front of the Cosine and Sine terms in Equation 2.4 must independently go to zero. Requiring nonzero A_1

and A_2 constants leads to the conclusion that the expressions C_1 and C_2 be zero. Solving for $C_1 = 0$ in Equation 2.6 results in the formula

$$\psi' = \frac{k}{\omega^2} \quad (2.8)$$

where k is a constant of integration.

We define $\beta(s) = 1/\psi'$ as the betatron function, along with $\alpha = -\frac{1}{2}\beta'$ and $\gamma = (1 + \alpha^2)/\beta$. The choice for these definitions becomes evident when solving $C_2 = 0$ in Equation 2.7. In terms of β and γ , the solution is simplified to

$$\beta'' + 2K\beta - 2\gamma = 0. \quad (2.9)$$

Plugging in $\alpha' = -\frac{1}{2}\beta''$, Equation 2.9 becomes

$$\alpha' = K\beta - \gamma. \quad (2.10)$$

Making a change of variables to express x in terms of constants $\sqrt{\epsilon}$ and δ , the equation of motion in Equation 2.4 and its derivative can be written as

$$x = \sqrt{\epsilon\beta} \cos(\psi + \delta) \quad (2.11)$$

$$x' = -\sqrt{\frac{\epsilon}{\beta}}(\alpha \cos(\psi + \delta) + \sin(\psi + \delta)) \quad (2.12)$$

where the previously defined expressions for β and α have also been used. The choice for the form $\sqrt{\epsilon}$ becomes clear when the results from Equations 2.11 and 2.12 are plugged into the expression $\gamma x^2 + 2\alpha x x' + \beta x'^2$. With much simplification, it can be shown that this

combination results in Equation 2.13.

$$\gamma x^2 + 2\alpha x x' + \beta x'^2 = \epsilon \quad (2.13)$$

This is the general equation for an ellipse, which results in the physical implication that in the case of periodic lattices, on subsequent revolutions the particle will trace out an ellipse in transverse phase space (xx' or yy') of area $A = \pi\epsilon$, with maximum extents $x_{\max} = \sqrt{\gamma\epsilon}$ and $x'_{\max} = \sqrt{\beta\epsilon}$.

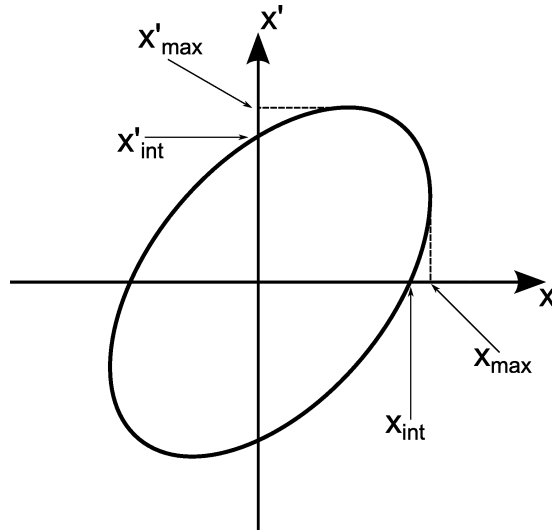


Figure 2.2: Phase space ellipse with negative α (defocusing).

Figure 2.2 shows the ellipse in phase space. Solving Equation 2.13 for the intersections at the x - and x' - axes gives $x_{\text{int}} = \sqrt{\epsilon/\gamma}$ and $x'_{\text{int}} = \sqrt{\epsilon/\beta}$. The area, $\pi\epsilon$, is known as the emittance of the beam — the phase space area of the beam — and is typically given in units of $\pi\text{mm}\cdot\text{mrad}$. The conservation of phase space area in an inertial reference frame is known as Liouville's Theorem [35].

This parametrization of the beam with β , γ , α , and ϵ , was derived by Courant and Snyder in their theory of strong-focusing synchrotrons [36]. These parameters may also be referred to

as Twiss parameters [37]. These parameters are important and convenient tools for describing the state of the beam.

The evolution of the beam in transverse phase space through a drift space is shown in Figure 2.3. A converging beam, with $\alpha > 0$, reaches a beam waist, where the beam is upright in phase space with $\alpha = 0$. After this point it diverges, with $\alpha < 0$. Here the beam is spreading out in position, x or y , and a focusing element would be necessary to maintain beam transport.

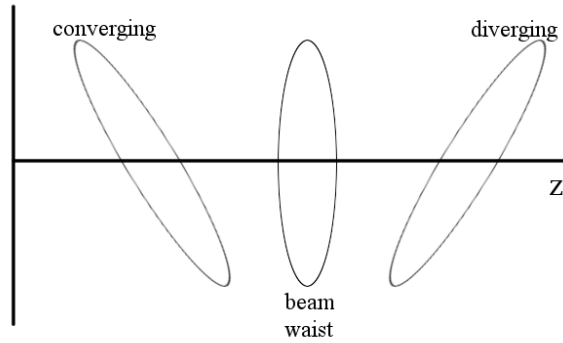


Figure 2.3: Phase space transformation of a converging beam along a drift space. After achieving a waist, the converging beam becomes diverging.

The two-dimensional transformation of the transverse coordinates defined in Equation 2.2 between \vec{U}_0 and \vec{U}_1 can be written as a 2×2 matrix, M , as shown in Equation 2.14. This matrix is referred to as a beam transport matrix.

$$\begin{pmatrix} x_1 \\ x'_1 \end{pmatrix} = M \begin{pmatrix} x_0 \\ x'_0 \end{pmatrix} \quad (2.14)$$

After inserting initial conditions, and much derivation, it can be shown that for linear motion, the transport matrix M takes the form of Equation 2.15, where $\Delta\psi = \psi(s_1) - \psi(s_0)$

is the phase advance of the beam between \vec{U}_0 and \vec{U}_1 [38].

$$M = \sqrt{\frac{\beta_1}{\beta_0}} \begin{pmatrix} \cos(\Delta\psi) + \alpha_0 \sin(\Delta\psi) & \beta_0 \sin(\Delta\psi) \\ \frac{1}{\beta_1}((\alpha_0 - \alpha_1) \cos(\Delta\psi) - (1 + \alpha_0 \alpha_1) \sin(\Delta\psi)) & \cos(\Delta\psi) - \alpha_1 \sin(\Delta\psi) \end{pmatrix} \quad (2.15)$$

Instead of defining a column vector U , of coordinates which represents a point on the phase space ellipse, as in Equation 2.2, it is often desirable to define a matrix that encompasses the ellipse definition in its entirety [39]. This matrix is called the Sigma matrix, and is defined by the ellipsoid equation in matrix form. In two dimensions this can be written as $U^T \sigma_{2D}^{-1} U = \epsilon_{2D}$, where U^T is the transpose of U .

It can be shown that

$$\sigma_{2D}^{-1} = \frac{1}{\epsilon_{2D}} \begin{pmatrix} \gamma & \alpha \\ \alpha & \beta \end{pmatrix} \Rightarrow \sigma_{2D} = \epsilon_{2D} \begin{pmatrix} \beta & -\alpha \\ -\alpha & \gamma \end{pmatrix} \quad (2.16)$$

with σ transforming as $\sigma_1 = M \sigma_0 M^T$. The full 6-D representation of the beam is sometimes referred to as a hyperellipsoid, with the σ matrix therefore representing the hyperellipsoid coefficients.

2.2 Longitudinal Motion

In the longitudinal plane, the reference particle is also known as the synchronous particle because it is synchronized with the RF frequency of the accelerating fields. During acceleration, this particle arrives at a given point with the exact design velocity for the accelerator, while particles with slightly less energy arrive later, and those with slightly more energy arrive earlier.

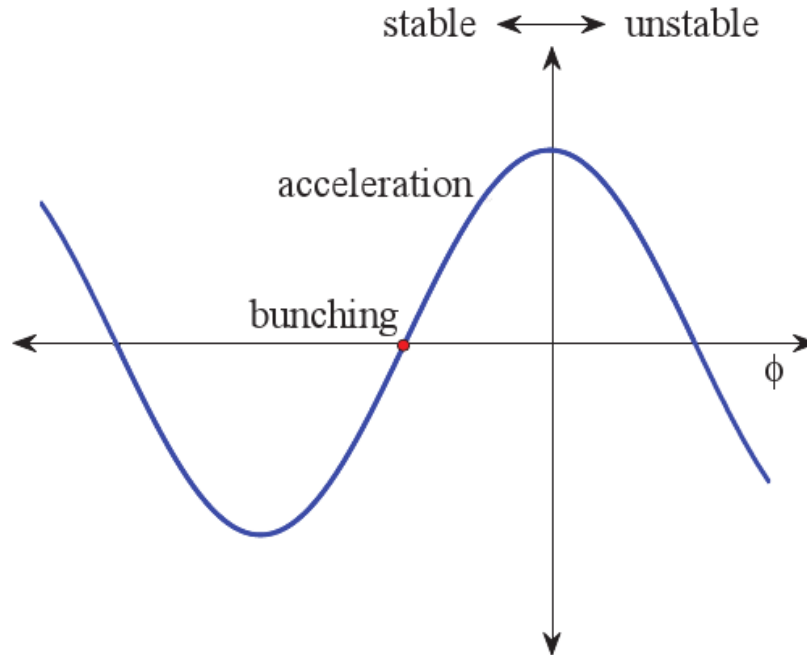


Figure 2.4: Longitudinal motion energy gain is proportional to $\cos(\phi)$. Points of zero energy gain (rebunching mode), stable acceleration (negative phase), and unstable region (positive phase) indicated.

Stable acceleration phases are located before the peak of the RF amplitude, as labeled in Figure 2.4. In this region, particles that arrive earlier (i.e. with more energy) than the synchronous particle experience a smaller accelerating field, while particles that arrive later (i.e. with less energy) than the synchronous particle experience a larger accelerating field. In this way, particles are kept oscillating around a stable phase and longitudinal focusing, or phase stability, is achieved.

On the opposite side of the crest of the RF, the situation is reversed. Now earlier particles will receive more acceleration while later particles will receive less acceleration, creating a region of instability and longitudinal defocusing.

A third point is labeled in Figure 2.4 at the x -intercept at $\phi = -90^\circ$, the “bunching” phase. At this point, the reference particle does not gain any energy. Later particles gain energy, and earlier particles actually lose energy (negative portion of the curve), resulting in a

longitudinal “bunching” effect for which this point is named. The x -intercept on the unstable side of the curve would also correspond to a point where the reference particle does not gain any energy. Here, though, unlike the stable “bunching” point, earlier particles would gain energy and later particles would lose energy, spreading the beam out longitudinally. This point is therefore not used in typical beam transport situations, but may be utilized in cases where longitudinal phase space manipulation is desired [40].

Similarly to transverse motion, the longitudinal motion of the beam can also be linearized in cases where higher-order effects can be neglected. Accelerator modeling codes have several different choices of longitudinal coordinates, some of which will be presented here.

The coordinates used to describe longitudinal motion are often Energy and Time, as these are canonical variables [41]. These variables are often referred to as the change in Energy and change in Time, ΔW and Δt , defined with respect to the reference particle. These coordinates conveniently lend themselves as a natural basis for longitudinal motion as their phase space emittance is conserved according to Liouville’s theorem. This basis is especially convenient when describing bunch length, or energy spread, as the widths are directly evident from the longitudinal phase space diagram.

Another longitudinal coordinate basis of canonical variables is z and p_z . Conventionally the coordinates will often be defined as z and z' , or z and $\delta = \Delta p/p_{\text{ref}}$, as seen in Equation 2.2, but it is important to remember that these bases are not strictly canonical variables.

One matrix modeling code, XAL, available as open source code through the Open XAL project [42], uses z and z' where $z' = \frac{\Delta p}{\gamma_0 p_{\text{ref}}}$. Here γ_0 refers to the relativistic factor, not to be confused with γ from the Courant-Snyder parameters defined previously. There is a simple transformation between XAL’s coordinate definition and the z and δ basis, as shown

in Equation 2.17.

$$\begin{pmatrix} z \\ \Delta p/p_{\text{ref}} \end{pmatrix} = \begin{pmatrix} 1 & 0 \\ 0 & \gamma_0^2 \end{pmatrix} \begin{pmatrix} z \\ z' \end{pmatrix} \quad (2.17)$$

It is easy to arrive at this transformation, as the same first coordinate, z , is used in both definitions, and z' is simply a function of δ : $z' = \frac{\delta}{\gamma_0^2} = \frac{\Delta p}{\gamma_0^2 p_{\text{ref}}}$. More complicated transformations are necessary when the longitudinal coordinates are more dissimilar.

The modeling code COSY [33], for example, uses the more esoteric longitudinal coordinates l and $\Delta W/W$, where $l = -\Delta t v_0 \frac{\gamma_0}{(1+\gamma_0)}$, and $\Delta W/W$ is the relative change in energy. This basis is chosen to give a coordinate along the beam line, l , that accounts for the relativistic factor as the longitudinal coordinate points in the direction of propagation. The transformation between this definition and the z and δ basis is slightly more complicated, as shown in Equation 2.18.

$$\begin{pmatrix} z \\ \frac{\Delta p}{p_{\text{ref}}} \end{pmatrix} = \begin{pmatrix} \frac{\gamma_0+1}{\gamma_0} & \frac{1}{\gamma_0(\gamma_0+1)} \\ 0 & \frac{\gamma_0}{\gamma_0+1} \end{pmatrix} \begin{pmatrix} l \\ \frac{\Delta W}{W} \end{pmatrix} \quad (2.18)$$

This can be shown in the following manner. Beginning with the definitions for p and W , $p = \beta\gamma m_0 c$ and $W = (\gamma - 1)m_0 c^2$, it can be shown that for a change in time, Δt , Equations 2.19 and 2.20 hold true, noting here that p , W , γ and β are all functions of time.

$$\Delta p = \gamma_0^2 p \frac{\Delta \beta}{\beta_0} \quad (2.19)$$

$$\Delta W = \gamma_0 \beta_0^2 m_0 c^2 \frac{\Delta p}{p_{\text{ref}}} \quad (2.20)$$

The relative change in W , $\Delta W/W$ is found by dividing ΔW in Equation 2.20 by $W =$

$(\gamma_0 - 1)m_0c^2$. This result can be simplified to yield the relationship shown in Equation 2.21.

$$\frac{\Delta p}{p_{\text{ref}}} = \frac{\gamma_0}{\gamma_0 + 1} \frac{\Delta W}{W} \quad (2.21)$$

This completes the derivation for the second row of matrix Equation 2.18. For the first row, across the change in time, Δt , z is defined by $z = -\Delta t(v_0 + \Delta v)$. Substituting in the definition for Δv from $v = \beta c \Rightarrow \frac{\Delta v}{v_0} = \frac{c\Delta\beta}{c\beta_0} = \frac{\Delta\beta}{\beta_0}$ leads to Equation 2.22.

$$z = -\Delta t v_0 \left(1 + \frac{\Delta\beta}{\beta} \right) = -\Delta t v_0 \left(1 + \frac{1}{\gamma_0^2} \frac{\Delta p}{p_{\text{ref}}} \right) \quad (2.22)$$

Plugging in the definition from Equation 2.21 for $\Delta p/p_{\text{ref}}$ as well as the COSY definition of $-\Delta t v_0 = \frac{l(1+\gamma_0)}{\gamma_0}$ into Equation 2.22 along with some rearranging of terms results in Equation 2.23.

$$l = \frac{\gamma_0}{1 + \gamma_0} z \left(\frac{1}{1 + \frac{1}{\gamma_0(1+\gamma_0)} \frac{\Delta W}{W}} \right) \quad (2.23)$$

The Taylor series $\frac{1}{1-x} = 1 + x + \dots$ can be used to simplify this result, making the assumption that $\frac{1}{\gamma_0(1+\gamma_0)} \frac{\Delta W}{W}$ is small. This yields $l \approx \frac{\gamma_0}{1+\gamma_0} z \left(1 - \frac{1}{\gamma_0(1+\gamma_0)} \frac{\Delta W}{W} \right)$, which can be rearranged to form Equation 2.24.

$$z = \left(\frac{\gamma_0 + 1}{\gamma_0} \right) l + \left(\frac{1}{\gamma_0(1 + \gamma_0)} \right) \frac{\Delta W}{W} \quad (2.24)$$

This is exactly the first row as given in the matrix Equation 2.18, completing this derivation. As previously stated, this matrix transforms the longitudinal coordinates between the two bases, z and $\Delta p/p_{\text{ref}}$, and l and $\Delta W/W$.

If the transport matrix, M , is expressed in one basis, it also must also be transformed

in order to be used in the different basis. Defining T the transformation matrix of the coordinates given in Equation 2.18, the following transformation is necessary to transform the transport matrix.

$$M_{\text{COSY}} = T^{-1}M_{\delta}T \quad (2.25)$$

In Equation 2.25 M_{δ} refers to a transport matrix expressed in terms of the $(z, \Delta p/p_{\text{ref}})$ basis, while M_{COSY} refers to the transport matrix in terms of the COSY longitudinal coordinates. Again, the transformation matrix T is defined by $U_{\delta} = TU_{\text{COSY}}$.

This transport matrix transformation definition can be shown in the following manner. Beginning with $U_{\delta 2} = M_{\delta}U_{\delta 1}$, plug in the definition $U_{\delta} = TU_{\text{COSY}}$. This results in $TU_{\text{COSY}2} = M_{\delta}TU_{\text{COSY}1}$. Multiplying both sides by T^{-1} yields Equation 2.26.

$$U_{\text{COSY}2} = \left(T^{-1}M_{\delta}T\right)U_{\text{COSY}1} \quad (2.26)$$

This can be compared with the definition $U_{\text{COSY}2} = M_{\text{COSY}}U_{\text{COSY}1}$ to arrive at the result shown in Equation 2.25. In this way the transport matrices in different bases may be arrived at in a straightforward manner once the transformation between coordinate bases is known.

When comparing modeling results across these different codes these appropriate transformations must be made in order to be consistent. It should also be noted that although some bases are used as they are more convenient in terms of calculations, such as the case with the momentum coordinates z and δ , and z and z' , these coordinates are not canonical variables and therefore their phase space emittance will not be conserved.

The next chapter will focus on the matrix modeling of several accelerator elements, including quadrupoles, solenoids, and accelerating cavities. To reinforce the validity of these models, benchmarking results with multi-particle tracking code IMPACT are also included.

Chapter 3

Modeling Elements

The ability to accurately model beam line elements is fundamental in the field of accelerator physics. Once a model for each element is established, the combination of these individual elements forms a model of the entire beam line. Developing further studies with these individual models promotes a deeper understanding of the beam's behavior through the accelerator, and also produces opportunities to measure basic beam properties, such as emittance.

This is the case for quadrupole emittance measurements which use our understanding of modeling quadrupoles in a beam line to manipulate the beam in such a way to derive the beam's emittance through a simple procedure. The quadrupole model and the results from emittance measurements taken with the quadrupole doublets before the RFQ at ReA are presented in the first section of this chapter.

Following is a detailed discussion of the investigation into two of the main elements that make up the ReA linac, the solenoid and the Quarter-Wave RF cavity. Solenoidal fields provide focusing, while RF cavities provide the acceleration, or, in some cases, deceleration. Each element is addressed in its own section, and results from modeling both elements together are also included. Also discussed is the modeling of combined solenoid and corrector magnets and studying the addition of errors, while further investigation of the RF cavities is left to Chapter 4.

This chapter concludes with a brief history of multiple charge state transport, as this is an important emerging technique for increasing beam intensity beyond the current limits of state-of-the-art ion sources. Matrix-based codes have not traditionally incorporated multiple charge state modeling functionality, motivating the matrix-based envelope method presented later in the chapter. This method greatly reduces the calculation time required compared with multi-particle tracking, allowing for on-line based modeling of multiple charge states.

3.1 Quadrupoles

Quadrupole magnets are important elements in transport beam lines—in fact, they make up one of the most basic units for beam transport, forming a ”Focus-Drift-Defocus-Drift”, or FODO, lattice [38]. This common lattice assembly of alternating focusing and defocusing quadrupoles allows for focusing to be accomplished in both transverse planes. The ability to utilize strong focusing and furthermore the ability to decouple the x and y transverse planes make quadrupoles an essential component in beam transport lines. Quadrupoles are focusing in one plane, and defocusing in the other, without coupling between the two planes.

Hyperbolic equipotential surfaces uniquely determine the quadrupole field, as shown in Figure 3.1. Ideal quadrupole fields are linear near the beam axis. Quadrupoles can be magnetic or electrostatic elements; magnetic quadrupole fields take the form of $B_x = Gy$, $B_y = Gx$, and $B_z = 0$, where G is the focusing gradient. Electrostatic quadrupole fields take the form of $E_x = 2Vx/a^2$, $E_y = -2Vy/a^2$, and $E_z = 0$, where V is the voltage on the hyperbolic electrodes, and a is the minimum radial aperture. As both produce transverse forces proportional to the distance from the central axis, they both have the same resulting transport matrix form, given in Equation 3.1. This matrix represents the case of a quadrupole

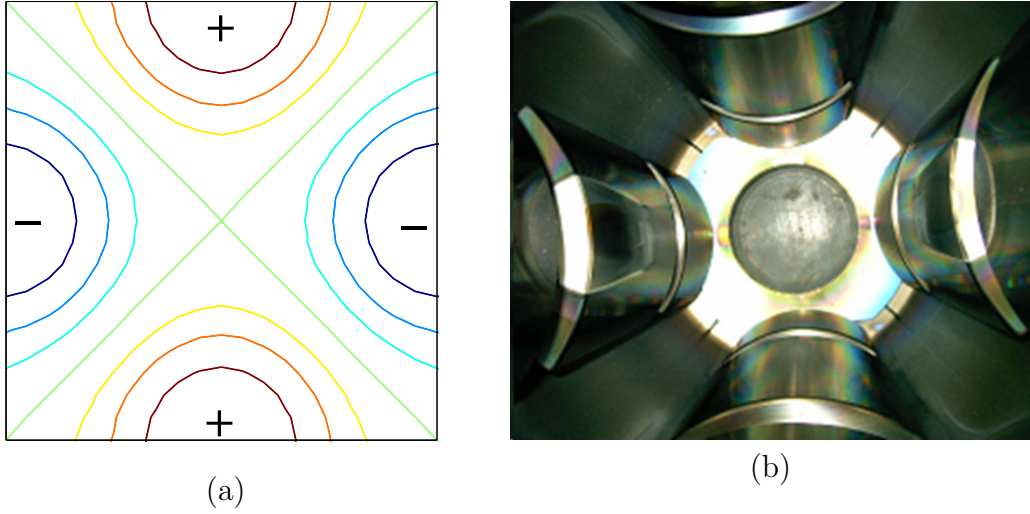


Figure 3.1: Left (a): Equipotential surfaces of quadrupole fields plotted for several different voltages. Right (b): The electrodes inside an actual electrostatic quadrupole are shaped along equipotential surfaces in order to produce a pure quadrupole field.

of length L and focusing strength k , focusing in the xx' plane.

$$M_{\text{quad}} = \begin{pmatrix} \cos(kL) & \frac{\sin(kL)}{k} & 0 & 0 \\ -k \sin(kL) & \cos(kL) & 0 & 0 \\ 0 & 0 & \cosh(kL) & \frac{\sinh(kL)}{k} \\ 0 & 0 & k \sinh(kL) & \cosh(kL) \end{pmatrix} \quad (3.1)$$

Notice that the 2×2 submatrix in the focusing plane, xx' , contains sines and cosines, while the 2×2 submatrix in the defocusing plane, yy' , contains hyperbolic sines and cosines. A quadrupole focusing in the yy' plane would have these submatrices reversed accordingly. Taking the limit as $kL \rightarrow 0$ of the focusing submatrix, the diagonal elements become $\cos(kL) \rightarrow 1$. The off-diagonal elements become $\frac{\sin(kL)}{k} \rightarrow L$ and $-k \sin(kL) \rightarrow -k^2 L$. In this way a thin-lens focusing approximation is recovered, with focal strength $\frac{1}{f} = k^2 L$.

As stated previously, the form of the quadrupole transport matrix, given in Equation 3.1, does not depend on whether the quadrupole is magnetic or electrostatic. The focusing

strength, k , however, is uniquely defined by the quadrupole type. If the quadrupole is magnetic, the focusing strength k is given by $k^2 = \frac{G}{B\rho}$, where $G[\text{T/m}]$ is the focusing gradient and $B\rho[\text{T m}]$ is the beam's magnetic rigidity. In the case of an electrostatic quadrupole, $k^2 = \frac{Q}{A} \frac{V_{\text{quad}}}{T} \frac{1}{a^2}$ where $V_{\text{quad}}[\text{V}]$ is the voltage on the electrode, $T[\text{eV/u}]$ is the kinetic energy, and $a[\text{m}]$ is the radial aperture.

If by varying the voltage of a quadrupole a waist can be established at the point of a diagnostic device downstream, it is possible to analyze the resulting data to make an indirect measurement of the beam's emittance. Although there are several methods of analysis, the one highlighted here uses Singular Value Decomposition (SVD) to compute a pseudoinverse of a known matrix to solve the least-squares problem presented.

The σ_x matrix can be written as

$$\sigma_x = \begin{pmatrix} \sigma_{11} & \sigma_{12} \\ \sigma_{21} & \sigma_{22} \end{pmatrix}_x \equiv \begin{pmatrix} \langle x^2 \rangle & \langle xx' \rangle \\ \langle x'x \rangle & \langle x'^2 \rangle \end{pmatrix}. \quad (3.2)$$

Recall that the σ matrix in this propagates from point 1 to point 2 in a beam line as $\sigma_2 = M\sigma_1 M^T$. Multiplying out these M and σ matrices and solving for the $\sigma(1,1)$ element yields Equation 3.3. The fact that $\sigma_{12} = \sigma_{21}$ has been used for simplification.

$$(\sigma_{11})_2 = \langle x^2 \rangle = M_{11}^2 (\sigma_{11})_1 + 2M_{11}M_{12} (\sigma_{12})_1 + M_{12}^2 (\sigma_{22})_1 \quad (3.3)$$

In this equation, the left-hand side, $\langle x^2 \rangle$, is the measurement of the beamsize. The M transport matrix elements can be calculated in order to solve for the elements of σ_1 which in turn determine the emittance.

By performing many measurements, a system of equations of the form shown in Equa-

tion 3.4 can be built. If this is written as $(\sigma_{11})_2 = A(M)(\sigma_{\text{column}})_1$, then $A(M)$ is an $n \times 3$ real matrix, with n the number of measurements. This matrix is not suitable for inversion, as it is not square. However, a factorization of A , the SVD, may be found which enables the calculation of the pseudoinverse of A . The pseudoinverse, also known as the Moore-Penrose pseudoinverse, is a generalized inverse matrix which can be used to find the least squares solution for an over-constrained system of equations where a unique solution may not exist.

$$\begin{pmatrix} \langle x^2 \rangle_1 \\ \vdots \\ \langle x^2 \rangle_n \end{pmatrix}_2 = \begin{pmatrix} (M_{11}^2)_1 & 2(M_{11})_1(M_{12})_1 & (M_{12}^2)_1 \\ \vdots & \vdots & \vdots \\ (M_{11}^2)_n & 2(M_{11})_n(M_{12})_n & (M_{12}^2)_n \end{pmatrix} \begin{pmatrix} \sigma_{11} \\ \sigma_{12} \\ \sigma_{22} \end{pmatrix}_1 \quad (3.4)$$

The SVD factorization is given in Equation 3.5. U is an $n \times n$ unitary matrix ($U^*U = UU^* = I_n$), Σ is an $n \times 3$ diagonal matrix of non-negative reals, and V^* is a 3×3 unitary matrix, the conjugate transpose of V . The matrices U and V act as rotations, while Σ is like a scaling transformation. These matrices are used to find A^+ , given in Equation 3.6.

$$A = U\Sigma V^* \quad (3.5)$$

$$A^+ = V\Sigma^+ U^* \quad (3.6)$$

In Equation 3.6, Σ^+ is the pseudoinverse of Σ , which can be found by replacing the non-zero entries along the diagonal by their reciprocals, and taking the transpose. Once A^+ is solved for, it may be multiplied with the column vector of measured beamsizes to determine the σ matrix elements column vector, $(\sigma_{\text{column}})_1 = A^+(\sigma_{11})_1$. Having solved for σ_{column} , the σ matrix is simply the symmetric 2x2 matrix formed from the elements of the

σ_{column} vector through Equation 3.2, noting again that $\sigma_{12} = \sigma_{21}$. It is then simple to find the emittance by taking the determinant of the σ matrix and solving through $\epsilon = \sqrt{\det(\sigma)}$.

This is the method of analysis chosen to determine the emittance from quadrupole scan data taken before the RFQ at ReA. One example scan is shown in Figure 3.2(a). There may have been errors in measuring the beamsize from the viewer plate, or instabilities in the beam itself which cause the measured data to not be entirely parabolic. When using a parabolic fit to the data, the resulting emittance was found to strongly depend on the choice of the subset of data analyzed, whereas the SVD method gave very consistent emittance values across the various subsets of the data. The results of the SVD analysis is summarized in Table 3.1. Note that Equation 2.16 has been used to define ϵ , β , α , and γ in this table.

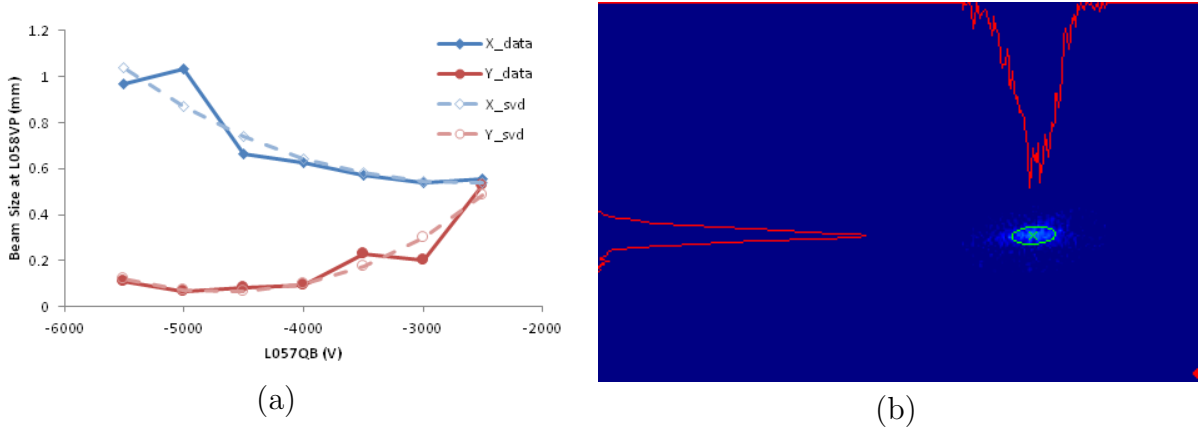


Figure 3.2: Left (a): Quad Scan Measurements performed before RFQ at ReA. Solid lines indicate measurement data, while dashed lines indicate SVD analysis. Right (b): Analyzed viewer data for L057QB=-5.5 kV with overlay of beam position and RMS beam size in green. Beam profiles in red are shown above and to the left of the beam spot.

Table 3.1: Analysis Results of Quad Scan Measurement Data (2-24-11)

L057QB	xx'	scan	L057QB	yy'	scan
$\epsilon_{xRMS}[\pi\text{mm} \cdot \text{mrad}]$	1.3064		$\epsilon_{yRMS}[\pi\text{mm} \cdot \text{mrad}]$	1.0874	
$\beta_x[\text{m/rad}]$	$-\alpha_x$	2.4272 1.7385	$\beta_y[\text{m/rad}]$	$-\alpha_y$	1.7325 -0.6737
$-\alpha_x$	$\gamma_x[\text{rad/m}]$	1.7385 1.6572	$-\alpha_y$	$\gamma_y[\text{rad/m}]$	-0.6737 0.8685

The final RMS-emittances as seen in Table 3.1 were found to be $\epsilon_x \approx 1.3\pi\text{mm} \cdot \text{mrad}$ and $\epsilon_y \approx 1.1\pi\text{mm} \cdot \text{mrad}$, which are consistent with predicted values. The values for $\beta_{x,y}$, $\alpha_{x,y}$, and $\gamma_{x,y}$, vary depending on the chosen fitting method, while the emittance stays fairly constant as it is the determinant of the matrix. It is important to note that the x and y Courant-Snyder parameters are at least of the same order of magnitude. The signs of α_x and α_y are opposite from one another, indicating that the beam is defocusing in the x -plane and focusing in the y -plane, consistent with transport through a drift following a quadrupole, as with this Quad Scan measurement.

During this measurement, a He^+ beam from the LB commissioning source was tuned through the center of the quadrupole L057QB, the second quadrupole in a quadrupole doublet that comes before the RFQ. After the centering is established, the quad's voltage is varied from 5.5 kV to -2.5 kV in steps of 0.5 kV. The beamsize was measured on a CaF scintillating viewer plate located in a diagnostic box immediately after the quadrupole. One of the analyzed viewer images can be seen in Figure 3.2(b). The transfer matrices used to complete the SVD analysis were computed in COSY, with fringe-fields on. The inclusion of fringe-fields had less than a 1% effect on the end result.

3.2 Solenoids

Solenoid magnets are one of the focusing elements used in ReA and FRIB that need to be modeled accurately. There are multiple models for focusing elements, including thick and thin lens approximations, as well as particle tracking through the magnetic field. COSY has several different solenoid models, including a tanh-based on-axis field model with optional fringe fields and a thick element model with a theoretical on-axis field distribution. XAL and

many other matrix modeling codes use an equivalent hard-edge model of the solenoid.

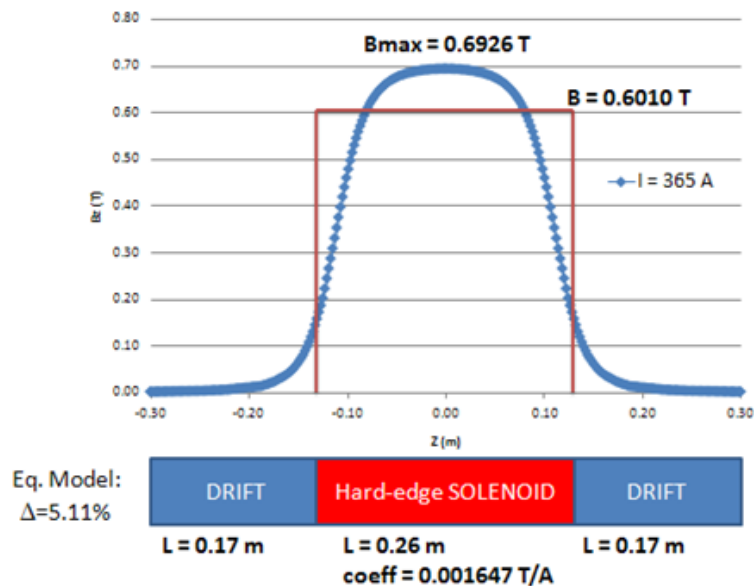


Figure 3.3: Equivalent hard-edge model for LEBT 0.6 T solenoid located before RFQ. The measured longitudinal field profile is shown with $B_{\max} = 0.6926$ T, while the equivalent hard-edge model consists of a drift section ($B = 0$ T), a constant field section ($B = 0.6010$ T), followed by a second drift section ($B = 0$ T).

This so-called equivalent hard-edge model method utilizes an effective solenoid length and field to approximate the magnetic field profile experienced by the beam, resulting in “hard” edges to the solenoid instead of the smooth increase of real fields. An example of this hard-edge equivalent model can be seen in Figure 3.3.

The motion in a solenoid can be seen as a series of three consecutive transformations on the beam, and motivates the method for computing the full transport matrix for a hard-edge solenoid model. First, the beam experiences fringe fields upon its entrance into the solenoid. Next, the beam travels through the body of the solenoid where it interacts with the longitudinal component of the field, B_z . Finally, the beam exits the solenoid and encounters fringe fields once again.

The entrance fringe fields of a solenoid produce an azimuthal velocity in the beam.

Similarly, the exit fringe fields produce an azimuthal velocity in the opposite direction, essentially canceling the effect of the entrance fringe fields by the time the beam has exited the solenoid.

This can be seen by examining the forces acting on the beam as it moves through a region of changing longitudinal magnetic field, where $\left|\frac{dB}{dz}\right| > 0$. Beginning from the Lorentz force, $\frac{d\vec{p}}{dt} = q\vec{v} \times \vec{B}$, when $B_\theta = 0$ the azimuthal component becomes

$$\frac{dp_\theta}{dt} = qv_z B_r. \quad (3.7)$$

The radial magnetic field, B_r , is related to the change in the longitudinal magnetic field, $\frac{dB_z}{dz}$, through Ampère's Law. From $\oint \vec{B} \cdot d\vec{l} = \mu_0 I_{\text{enc}}$ in a current free region, along a circular path of radius r within the solenoid fringe field region, we arrive at

$$\oint \vec{B} \cdot d\vec{s} = B_z \pi r^2 + 2\pi r \int B_r dz = 0. \quad (3.8)$$

Solving for B_r in terms of B_z yields

$$\int B_r dz = -\frac{r}{2} B_z \Rightarrow B_r = -\frac{r}{2} \frac{dB_z}{dz}. \quad (3.9)$$

As the beam is moving along the z -direction, we can rewrite the expression in Equation 3.7 as

$$\frac{dp_\theta}{dz} \frac{dz}{dt} = qv_z B_r. \quad (3.10)$$

Plugging in the solution for B_r and simplifying yields $\frac{dp_\theta}{dz} = -\frac{qr}{2} \frac{dB_z}{dz}$, which becomes $\Delta p_\theta = -\frac{qr}{2} \Delta B_z$. Here ΔB_z , defined across the "hard-edge" boundary, is simply $\Delta B_z = B_z$.

Looking at the x -component, $\Delta p_x = -\Delta p_\theta \sin \theta$, and using $y = r \sin \theta$ we find

$$\Delta p_x = \frac{qr}{2} B_z \sin \theta = \frac{qB_z}{2} y. \quad (3.11)$$

Rewriting this in terms of the angle $\Delta x' = \frac{\Delta p_x}{p_z}$, and using the definition of magnetic rigidity, $B\rho = \frac{p_z}{q}$, we arrive at the equation

$$\Delta x' = \frac{qB_z}{2p_z} y = \frac{B_z}{2B\rho} y. \quad (3.12)$$

Similarly, it can be shown that

$$\Delta y' = -\frac{qB_z}{2p_z} x = -\frac{B_z}{2B\rho} x. \quad (3.13)$$

This derivation leads to the matrix for a step into(+), or out of(-), a constant longitudinal magnetic field, as

$$M_{\text{edge}\pm} = \begin{pmatrix} 1 & 0 & 0 & 0 \\ 0 & 1 & \pm k & 0 \\ 0 & 0 & 1 & 0 \\ \mp k & 0 & 0 & 1 \end{pmatrix}$$

where k is given by

$$k = \frac{B_z}{2B\rho} \quad (3.14)$$

and B_z is the longitudinal magnetic field of the solenoid. The transport matrices used when describing motion through a solenoid are 4×4 matrices, as the xx' and yy' planes are coupled. Note that when stepping into a magnetic field, the field is increasing such that $\frac{dB_z}{dz} > 0$.

While stepping out of a magnetic field, the field is decreasing such that $\frac{dB_z}{dz} < 0$ and this is what changes the sign that appears in front of the two k terms in the M_{edge} matrix.

A similar derivation for the rotation of a charged particle in a constant magnetic field is used for describing the motion of the beam through the body of a solenoid. The transformation of the (x, x', y, y') vector through the body of a solenoid with a constant magnetic field $\vec{B} = B_z \hat{z}$ is given by the following matrix:

$$M_{\text{body}} = \begin{pmatrix} 1 & \frac{\sin(\theta)}{2k} & 0 & \frac{-(1-\cos(\theta))}{2k} \\ 0 & \cos(\theta) & 0 & \sin(\theta) \\ 0 & \frac{-(1-\cos(\theta))}{2k} & 1 & \frac{\sin(\theta)}{2k} \\ 0 & -\sin(\theta) & 0 & \cos(\theta) \end{pmatrix} \quad (3.15)$$

where $\theta = 2kL$.

When the entrance, body, and exit matrices are multiplied together, they give the final matrix of the hard-edge equivalent solenoid model.

$$M_{\text{sol}} = M_{\text{exit}} \times M_{\text{body}} \times M_{\text{entrance}} \quad (3.16)$$

where

$$M_{\text{entrance}} = M_{\text{edge}+} \quad (3.17)$$

$$M_{\text{exit}} = M_{\text{edge}-} \quad (3.18)$$

resulting in

$$M_{\text{sol}} = \begin{pmatrix} \cos(kL)^2 & \frac{\sin(kL)\cos(kL)}{k} & \sin(kL)\cos(kL) & \frac{\sin(kL)^2}{k} \\ -k\sin(kL)\cos(kL) & \cos(kL)^2 & -k\sin(kL)^2 & \sin(kL)\cos(kL) \\ -\sin(kL)\cos(kL) & \frac{-\sin(kL)^2}{k} & \cos(kL)^2 & \frac{\sin(kL)\cos(kL)}{k} \\ k\sin(kL)^2 & -\sin(kL)\cos(kL) & -k\sin(kL)\cos(kL) & \cos(kL)^2 \end{pmatrix}$$

the full hard-edge equivalent solenoid transport matrix.

As noted, the hard-edge model of a solenoid simplifies the smooth growth and decline of the magnetic field on axis to a rectangular function which consists of a step up, constant field, and step down approximation. The matrix representation of this model is made up of matrices representing the entrance into the solenoid, the solenoid body, and the exit from the solenoid. The correct effective length and field strength, however, must be chosen for the hard edge solenoid model to be valid.

3.2.1 Hard-Edge Model Parameterization

It is important to determine appropriate solenoid parameters when using the hard-edge model. These parameters include the effective length, L_e , and the effective field strength, which may be represented by the magnitude of the scaling coefficient between current and magnetic field, $B_e = \mu_e[\text{T/A}] \times I[\text{A}]$. In order to determine which combinations of these two factors would be appropriate in accurately modeling a given solenoid field, a numerical method for comparing the hard-edge model with an approximated “real-field” model, which closely follows the actual solenoid field profile, has been developed.

This numerical method computes the error between the transport matrix that steps

through the solenoid field in many small sections, approximating the “real-field” profile, and the matrix where there is only one step through the solenoid, the hard-edge model. This error is defined as the sum of the relative difference in the matrix elements, as given in Equation 3.19. This simple difference definition provides a method of evaluation to determine the degree to which the two matrices agree, allowing them to be compared numerically. Here $M [i, j]$ represents the i -th row and j -th column of matrix M .

$$\Delta M_{\text{tot}} = \sum_i \sum_j \left(\frac{M_{\text{step}} [i, j] - M_{L_e B_e} [i, j]}{M_{\text{step}} [i, j]} \right)^2 \quad (3.19)$$

This calculation is performed for a wide range of combinations of L_e and B_e , mapping out an effective solution space. The result is dependent on both the scaling of the magnetic field, as well as the beam’s rigidity. A sample 2×2 plot of this error as a function of effective field strength and effective length produced by this method is shown in Figure 3.4.

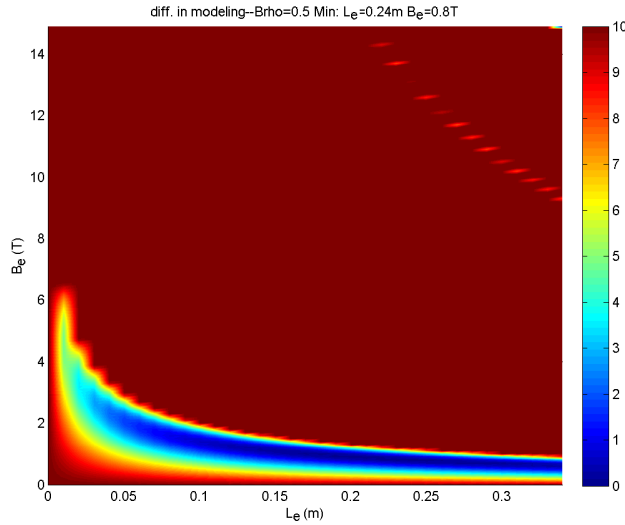


Figure 3.4: The ReA solenoid L090SN scaled to 1T for $B\rho = 0.5 \text{ T m}$. The solution that minimized M_{tot} is found to be at $L_e = 0.24 \text{ m}$, $B_e = 0.8 \text{ T}$.

In this case, the magnetic field profile has been scaled down to 1 T. The beam has

magnetic rigidity $B\rho = 0.5 \text{ T m}$, which corresponds to a H_2 beam at 3 MeV/u . In Figure 3.4, red represents high error as calculated from Equation 3.19, while blue represents a region of minimal error. The optimum solution found is $L_e = 0.24 \text{ m}$, with $B_e = 0.8 \text{ T}$. The coefficient μ_e can be computed from Equation 3.20, and comes out to 0.0883 T/A .

$$B_e [\text{T}] = \left(\frac{B_{\text{max}}}{I} \right)_{\text{profile}} \times \frac{B_e}{B_{\text{scaled}}} \times I [\text{A}] = \mu_e \times I [\text{A}] \quad (3.20)$$

The difficulty with using this method to accurately calculate the correct effective length and field strength for the hard-edge model is that it depends on the magnitude of the magnetic field in the solenoid, as well as the magnetic rigidity of the beam. Unfortunately, this brute force method of calculating the relevant solenoid parameters is not practical when many different types of beams with various Q/A ratios and energies will be used at ReA. It can, however, prove useful as a cross-check in determining which L_e and B_e combinations are reasonable, as calculated by a more general solution which would be valid for all cases.

One natural method would be to calculate L_e and B_e directly from the solenoid field distribution [43]. The effective length is defined intuitively, as given in Equation 3.21. The importance of the focal length depending on B^2 , not B ($\frac{1}{f} = k^2 L$ where $k = \frac{B}{2B\rho}$), motivates the determination of the effective field strength in Equation 3.21.

$$L_e = \frac{\int B_z dz}{B_e} \quad B_e^2 = \frac{\int B_z^2 dz}{L_e} \quad (3.21)$$

Multiplying through by the denominators, the integral quantities may be defined as given

in Equations 3.22 and 3.23.

$$I_1 = B_e L_e = \int B_z dz \quad (3.22)$$

$$I_2 = B_e^2 L_e = \int B_z^2 dz \quad (3.23)$$

This system of equations can be solved as

$$B_e = \frac{I_2}{I_1} \quad L_e = \frac{I_1^2}{I_2}. \quad (3.24)$$

The end result of this parameterization is given by Equation 3.25.

$$L_e = \frac{(\int B dz)^2}{\int B^2 dz} \quad \mu_e = \frac{\int B^2 dz}{I \int B dz} \quad (3.25)$$

This method has the advantage that it does not depend on the central field of the solenoid, B_0 , or the beam's rigidity, $B\rho$. This method also produced reasonable beam responses through the ReA linac when modeling the beam with the machine settings from the QWR steering experiment on August 29th, 2013, as seen in Figure 3.5. The H₂ beam is at 0.6 MeV/u, with no cavities turned on, and the original initial conditions given by the RFQ output simulation have been used. The vertical dashed lines indicate the location of the diagnostic boxes. The beam size was fairly equal at both the L092 and L110 locations, represented by the vertical lines at ~6 m and ~11 m. This is reproduced well with the solenoid parameterization given by this method.

It is important to recognize the regions where this method is valid. Because this method does not give any information about the beam's rigidity or the scaling of the solenoid, we should be sure to check that we are in the region where the equivalent method is comparable

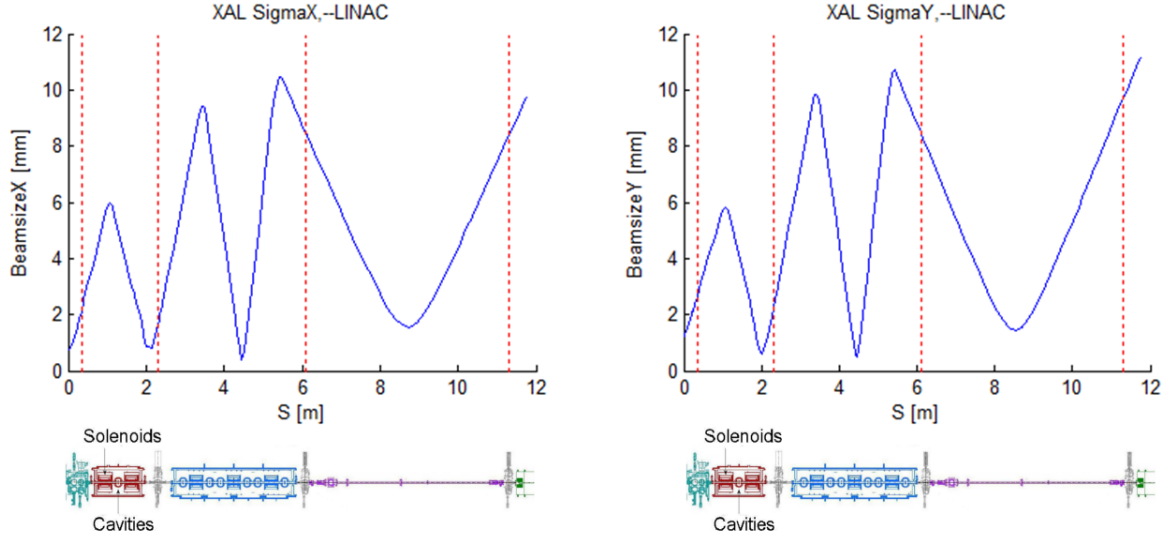


Figure 3.5: XAL simulation of transverse beamsizes, $\langle x^2 \rangle$ and $\langle y^2 \rangle$, σ_{11x} and σ_{11y} as defined in Equation 3.2, for the ReA Linac without the third cryomodule using the solenoid parameterization defined in Equation 3.25. Vertical dashed lines indicate diagnostic locations. Note that the beam is focused in both x and y at the solenoid locations, and the beam sizes at the third and fourth diagnostic locations, at ~ 6 m and ~ 11 m respectively, are of similar magnitude, which was observed experimentally.

to the step by step transport matrix. If the fields are too large for the beam's rigidity, as shown in Figure 3.6, then the beam's motion will be influenced by the steeply increasing fields at edges of the solenoid. The linear transport matrix approximation is only valid where these nonlinear effects can be neglected, so this should be taken into consideration.

In Figure 3.6, $B\rho$ ranges from 0.22 Tm to 1.00 Tm, while B_e ranges from 1 T to 8 T. The rows from top to bottom represent $B\rho = 0.22$ Tm, corresponding to H_2 at 0.6 MeV/u, $B\rho = 0.32$ Tm, $B\rho = 0.44$ Tm corresponding to He at 0.6 MeV/u, $B\rho = 0.50$ Tm, corresponding to H_2 at 3 MeV/u, $B\rho = 0.75$ Tm, and $B\rho = 1.00$ Tm corresponding to He at 3 MeV/u. The columns represent $B_e = 1 - 8$ T in steps of 1 T. This covers the entire range of relevant beam rigidities and solenoid fields available at ReA.

The blue regions in Figure 3.6 are where the hard-edge model converges to the field-profile

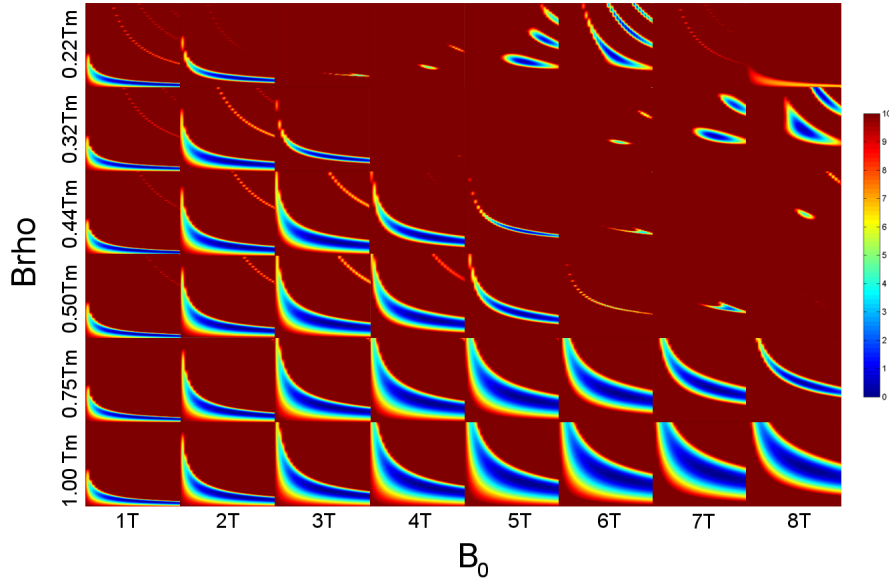


Figure 3.6: Numerical method results of B_e vs. L_e shown calculated at various $B\rho$ and B_0 values that cover the relevant ReA ranges. The red regions indicate areas with high divergence between the hard-edge and field-profile models, while the blue regions indicate areas where the two models agree. Note that solutions are present (blue regions exist) for low beam rigidities, $B\rho$, only at low solenoid fields, B_0 . The solution range increases to higher fields at higher rigidities.

model. For beams of low rigidity (upper rows), this is only valid at the lowest field strengths (left most columns). As the beam's rigidity increases, the model is valid at higher and higher fields. This is because higher energy beams are more difficult to influence, and therefore the hard-edge model is still valid even at the stronger fields. It is important to ensure that when the hard-edge model is utilized, the relevant parameterization corresponds with an appropriate region as given by Figure 3.6. This is typically not an issue when modeling machine settings because during operation the solenoid's fields are optimally kept at the lowest possible values, which means we will most likely always be in an acceptable region, shown in blue in Figure 3.6.

3.2.2 Solenoid with Corrector

Each solenoid at ReA contains horizontal and vertical correctors which can steer a misaligned beam back toward its design trajectory. In this section we will restrict our discussion to horizontal correctors only (B_y), as the treatment is analogous for vertical correctors (B_x). In order to model this configuration simply, we insert a thin horizontal corrector dipole element into the center of the body of the hard edge solenoid model. This total “thin-lens” matrix model will then consist of three matrices multiplied together: the second half of the solenoid body, a thin-lens corrector, and the first half of the solenoid body, as seen in Equation 3.26.

$$M_{\text{thin-corr/sol}} = M_{\text{body}}\left(\frac{L_{\text{sol}}}{2}\right) \times M_{\text{thin-corr}} \times M_{\text{body}}\left(\frac{L_{\text{sol}}}{2}\right) \quad (3.26)$$

Here we must deal with 6×6 matrices, as the thin dipole element couples the longitudinal motion with the transverse. The $M [1, 4; 1, 4]$ sub-matrix of M_{body} is defined in Equation 3.15, plugging in $L = \frac{L_{\text{sol}}}{2}$. The $M [5, 6; 5, 6]$ sub-matrix of M_{body} is simply a drift matrix with $L = \frac{L_{\text{sol}}}{2}$, and all other elements are zero.

The terms in the matrix for a thin corrector are simply derived from the equations of motion for a charged particle with longitudinal velocity \dot{z} in the corrector’s magnetic field: B_y for a horizontal corrector, B_x for a vertical corrector. In the case of a horizontal corrector, from the Lorentz force we have $m\ddot{x} = -qvB_y = -q\dot{z}B_y$. Simplifying with $B\rho = \frac{p}{q} = \frac{m\dot{z}}{q}$ results in $\ddot{x} = \frac{-B_y\dot{z}^2}{B\rho}$. Using $\frac{d}{dt}(z\dot{z}) = \dot{z}\dot{z} + z\ddot{z}$ and recognizing that there is no acceleration ($\ddot{z} = 0$), the equation becomes $\ddot{x} = \frac{-B_y}{B\rho} \frac{d}{dt}(z\dot{z})$. Integrating both sides produces $\dot{x} = \frac{-B_y}{B\rho} z\dot{z}$. Therefore the only non-zero off-diagonal element in the thin horizontal corrector matrix is element $[2; 6]$, how \dot{x} depends on \dot{z} .

Substituting $z = L$, the length of the corrector, in the above equation, $M_{\text{thin-corr}}$ for a

thin horizontal corrector with field B_y becomes simply the identity matrix with element $M[2;6] = -\frac{B_y L}{B\rho}$. A vertical corrector with field B_x would have element $M[4;6] = \frac{B_x L}{B\rho}$ instead.

Multiplying the matrices out results in the formula for the “thin-lens” transfer matrix as given in Equation 3.27. Here we define the dimensionless quantity $\xi = \frac{B_z L}{B\rho}$. B_z is the magnetic field of the solenoid, and B_y is the magnetic field of the corrector.

$$M_{\text{thin-corr/sol}} = \begin{pmatrix} 1 & \frac{B\rho \sin \xi}{B_z} & 0 & \frac{B\rho(1-\cos \xi)}{B_z} & 0 & -\frac{B_y L \sin\left(\frac{\xi}{2}\right)}{2B_z} \\ 0 & \cos \xi & 0 & \sin \xi & 0 & -\frac{B_y L \cos\left(\frac{\xi}{2}\right)}{2B\rho} \\ 0 & -\frac{B\rho(1-\cos \xi)}{B_z} & 1 & \frac{B\rho \sin \xi}{B_z} & 0 & \frac{B_y L \left(1-\cos\left(\frac{\xi}{2}\right)\right)}{2B_z} \\ 0 & -\sin \xi & 0 & \cos \xi & 0 & \frac{B_y L \sin\left(\frac{\xi}{2}\right)}{2B\rho} \\ 0 & 0 & 0 & 0 & 1 & L \\ 0 & 0 & 0 & 0 & 0 & 1 \end{pmatrix} \quad (3.27)$$

The “full-field” matrix solution is obtained by considering the total combined fields of the solenoid and vertical dipole corrector, $\vec{B} = B_y \hat{y} + B_z \hat{z}$, across the entire length of the element, as opposed to breaking up the interactions as in the “thin-lens” approximation. The Lorentz force, $q(\vec{v} \times \vec{B}) = (v_y B_z - v_z B_y) \hat{x} + (-v_x B_z) \hat{y} + (v_x B_y) \hat{z}$, produces the resulting equations of motion, given in Equations 3.28-3.30.

$$m\gamma\ddot{x} = qB_z\dot{y} - qB_y\dot{z} \quad (3.28)$$

$$m\gamma\ddot{y} = -qB_z\dot{x} \quad (3.29)$$

$$m\gamma\ddot{z} = qB_y\dot{x} \quad (3.30)$$

Solving these equations of motion yields the “full-field” matrix solution as shown in Equation 3.31. Here the quantities $B_\alpha = \sqrt{B_y^2 + B_z^2}$, and $\eta = \frac{B_\alpha L}{B_\rho}$ are defined.

$$M_{\text{full-field}} = \begin{pmatrix} 1 & \frac{B_\rho \sin \eta}{B_\alpha} & 0 & \frac{B_\rho B_z (1 - \cos \eta)}{B_\alpha^2} & 0 & -\frac{B_\rho B_y (1 - \cos \eta)}{B_\alpha^2} \\ 0 & \cos \eta & 0 & \frac{B_z \sin \eta}{B_\alpha} & 0 & -\frac{B_y \sin \eta}{B_\alpha} \\ 0 & -\frac{B_\rho B_z (1 - \cos \eta)}{B_\alpha^2} & 1 & L - \frac{B_z^2 \left(L - \frac{B_\rho \sin \eta}{B_\alpha} \right)}{B_\alpha^2} & 0 & \frac{B_y B_z \left(L - \frac{B_\rho \sin \eta}{B_\alpha} \right)}{B_\alpha^2} \\ 0 & \frac{B_z \sin \eta}{B_\alpha} & 0 & 1 - \frac{B_z^2 (1 - \cos \eta)}{B_\alpha^2} & 0 & \frac{B_y B_z (1 - \cos \eta)}{B_\alpha^2} \\ 0 & \frac{B_\rho B_y (1 - \cos \eta)}{B_\alpha^2} & 0 & \frac{B_y B_z \left(L - \frac{B_\rho \sin \eta}{B_\alpha} \right)}{B_\alpha^2} & 1 & L - \frac{B_y^2 \left(L - \frac{B_\rho \sin \eta}{B_\alpha} \right)}{B_\alpha^2} \\ 0 & \frac{B_y \sin \eta}{B_\alpha} & 0 & \frac{B_y B_z (1 - \cos \eta)}{B_\alpha^2} & 0 & 1 - \frac{B_y^2 (1 - \cos \eta)}{B_\alpha^2} \end{pmatrix} \quad (3.31)$$

These two solutions, the “full-field” and the “thin-lens”, agree when we make the assumption that the corrector field is much weaker than the solenoid field, $B_y \ll B_z$, such that $B_y/B_z \rightarrow 0$. If we can confidently determine that this assumption is valid in the case of Hydrogen beams, H_2 , which require the weakest solenoid fields, then it will therefore be valid for all beams.

The two matrices given in Equations 3.27 and 3.31 are applied to a σ matrix of parameters typical of a beam exiting the ReA RFQ. The ratio of B_y to B_z is varied across both models, and the beam sizes at the end of the solenoid models are then compared.

An approximately 1% effect on the beam size is found when B_y is approximately 25% the strength of B_z . In Figure 3.7, the percent difference between the two models, the “thin-lens” and “full-field” solutions, of the beamsize at the solenoid exit is plotted as a function of corrector field strength, B_y where the solenoid field has been set at $B_z = 2$ T. Typical solenoid fields for H_2 beams in the ReA linac are on the order of a few Tesla, while the

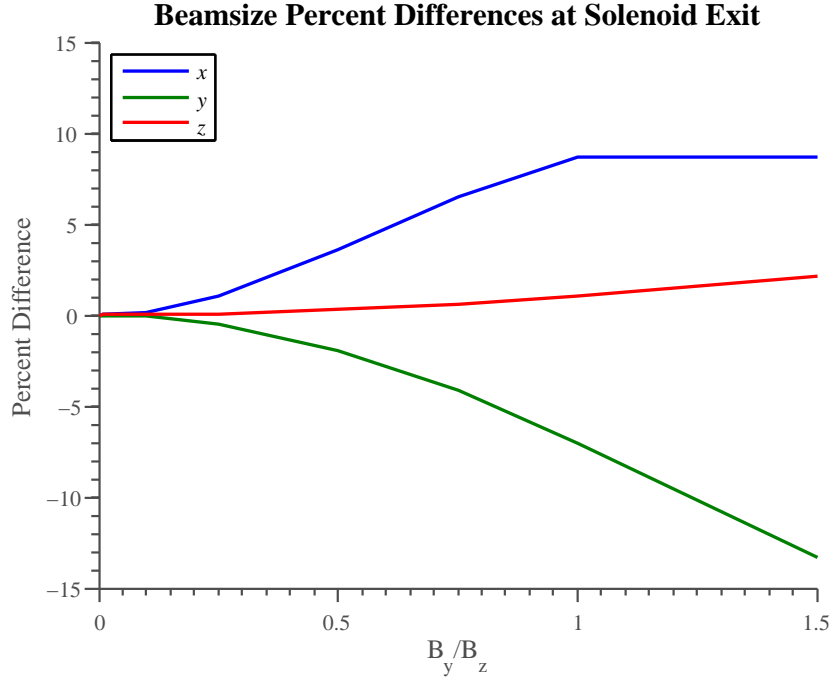


Figure 3.7: Percent difference between the “full-field” and “thin-lens” models for beamsizes calculated at the solenoid exit, $z = 0.2$ m, as a function of relative corrector field strength, B_y , to the main solenoid field, $B_z = 2$ T.

corrector fields only reach a few milliTesla. This is less than 0.1% of typical B_z values, and in the region in Figure 3.7 where the percent difference is $\ll 1\%$. Therefore the error introduced by the simplified model is completely negligible in this region, as we hoped. It is concluded that the thin-lens model of a corrector at the center of the solenoid is therefore valid.

3.2.3 Solenoid Error Study

As with any kind of modeling, it is always important to remember that the physical elements being modeled are subject to real-life conditions, with minor imperfections such as asymmetries in the field profiles, misalignments of the elements, or fluctuating temperatures potentially affecting their performance. It is therefore necessary to study what effect small errors will introduce to the system being modeled. In particular, it is extremely important to understand

how small errors affect a system that contains many of the same element, as in these cases small systematic errors can compound quickly and cause serious problems.

For example, FRIB uses a total of 87 superconducting solenoids for beam focusing through its linac and folding segments [29]. It is therefore important to know the effect of errors in the solenoid strength on the beamsize exiting the solenoid. To illustrate this technique, we introduce small errors, $d_{i,k}$ (on order of 1.0% and 0.5%), to the solenoid field strengths in FRIB Linac Segment 1, and calculate the resulting change in beamsize, $\Delta\sigma$. The new solenoid strengths are produced through the formula $B_{1,k} = B_{0,k} \times (1 + d_{i,k})$, where k is the solenoid index, and i is the run number through the XAL model. The error introduced, $d_{i,k}$, is a Gaussian error $d_{i,k} = \mu + d_{\text{RMS}} \times \text{randn}$; where $\mu = 0$, d_{RMS} is the maximum error amplitude, and randn is a pseudorandom value generated by MATLAB drawn from the standard normal distribution.

With the error introduced, there are fluctuations in the beam envelope about the original case, as seen in Figure 3.8. The RMS of the relative difference in σ in each case approaches the value of the error that was introduced to the solenoid fields. A 1% random error on the solenoid fields produced $\frac{\Delta\sigma_{\text{RMS}}}{\sigma} \approx 0.1$ while A 0.5% error resulted in $\frac{\Delta\sigma_{\text{rms}}}{\sigma} \approx 0.05$. From the plots of $\frac{\Delta\sigma_{\text{RMS}}}{\sigma}$ on the right-hand side of Figure 3.8, one can see that the error has essentially saturated after ~ 10 m, and does not increase with the additional segments of solenoids.

This result is encouraging in that random errors on the solenoid fields produce a bounded error in the beam size that does not increase rapidly throughout the beam line. These errors should be quite low as superconducting magnets can kept stable at a precise field. Even with small errors throughout the beam line, only a small change in the beamsize is observed, not a compounding effect throughout the linac which would be problematic for operations.

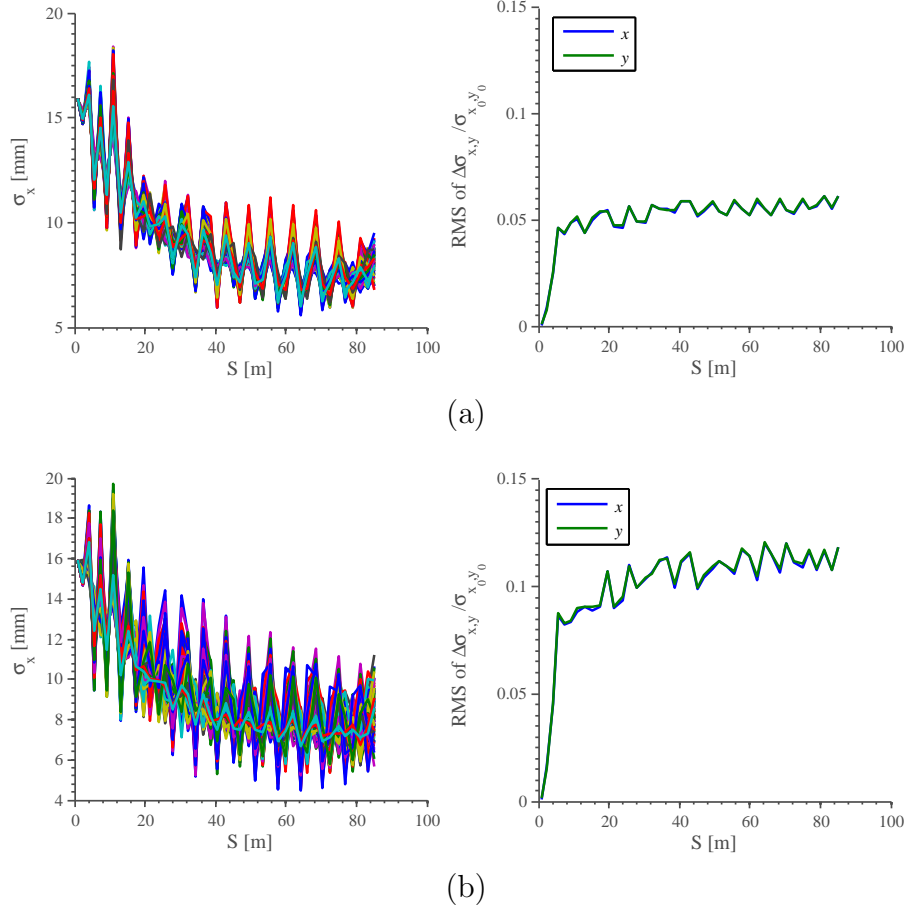


Figure 3.8: FRIB Linac Segment 1 (XAL) with random Gaussian error added to each solenoid. Gaussian errors of about (a)0.5% and (b)1% have been used — note how the RMS of the relative difference in $\sigma_{x,y}$ grows by approximately the percentage of the Gaussian error introduced to the system. It is an important result that this growth levels out without increasing exponentially.

3.3 Accelerating Cavities

Accelerating cavities are arguably the most important beam line elements to be modeled in a linac. ReA, as well as FRIB, uses Superconducting Radiofrequency (SRF) cavities to accelerate the beam. This section focuses on the Quarter-Wave Resonator (QWR) type, seen in Figure 3.9, as this is the type used during the experiment detailed in Chapter 4.

This section discusses the theoretical background of particle acceleration through QWRs in order to understand how these structures are modeled. It is important to first be familiar

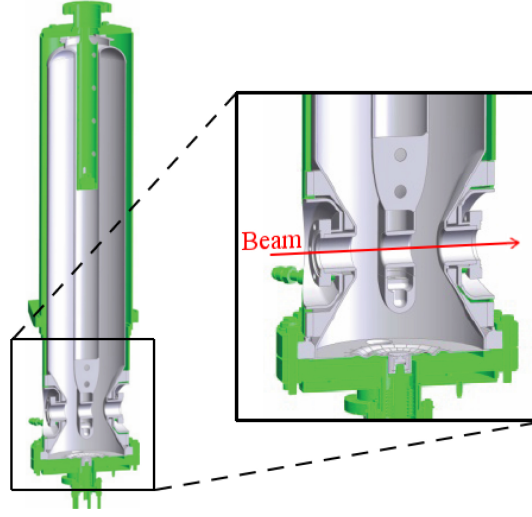


Figure 3.9: Cut-away image of the ReA $\beta = 0.041$ QWR cavity type. The two accelerating gaps that the beam travels through towards the bottom of the cavity are shown in detail.

with the electromagnetic fields present in the cavity. These fields ultimately determine the motion of particles through these accelerating structures, so they shall be discussed in more detail here.

3.3.1 Electromagnetic Fields

In a vacuum, the wave equation is given by equation 3.32 where ∇^2 is the Laplacian and c is the speed of light. This equation is derived from Maxwell's equations, and determines the propagation of electromagnetic waves. The electric field, \vec{E} , or magnetic field, \vec{B} , can be substituted for the wave function, $u(\vec{r}, t)$.

$$\left(\nabla^2 - \frac{1}{c^2} \frac{\partial^2}{\partial t^2} \right) u(\vec{r}, t) = 0 \quad (3.32)$$

By separating variables, $u(\vec{r}, t) = u(\vec{r})e^{i\omega t}$, a time-independent spatial equation for steady state oscillations is achieved, known as the Helmholtz equation, given in 3.33. In this equation

the wave vector, k , is given by $k = \omega/c$.

$$\left(\nabla^2 + k^2\right) u(\vec{r}) = 0 \quad (3.33)$$

In a hollow resonator, such as the case with accelerating cavities, the electric field satisfies the boundary condition that the electric field vanishes at the surface [44, p. 310]. Using the boundary conditions and the Helmholtz equation, a solution for the electromagnetic fields inside the cavity can be found. Due to the complex surface structures, analytical solutions are foregone in favor of determining the solution numerically on a mesh. Dedicated commercial electromagnetic field solvers are available for this purpose, such as CST Microwave Studio [45].

The fields present in the ReA $\beta = 0.041$ cavity are shown in Figure 3.10. These field profiles are calculated along the z -axis of the 3D field maps [46]. The z -axis is centered on the beam port of the cavity, and taken as the ideal trajectory of the beam. Figure 3.10 plots the electric and magnetic fields vs. the longitudinal position in the cavity, with $z = 0$ positioned at the center of the cavity.

E_z is the electric field in the longitudinal direction which is responsible for the acceleration of the beam through the cavity gaps. E_y is the electric field in the vertical direction, and can be positive or negative depending upon the design of the cavity. From the symmetry of the cavity, $\vec{B} = B_\phi(\vec{r})\hat{\phi}$, which results in $\vec{B} = B_x(z)\hat{x}$ along the z -axis. For a right-handed coordinate system with the z -axis to the right and y to the top of the page, the x -axis points into the page. This corresponds to B_x pointing out of the page for negative z , and into the page for positive z , as is seen by the sign of B_x going from negative to positive along the z -axis in Figure 3.10.

In this instance, the second gap, located at positive z , is accelerating the beam. The

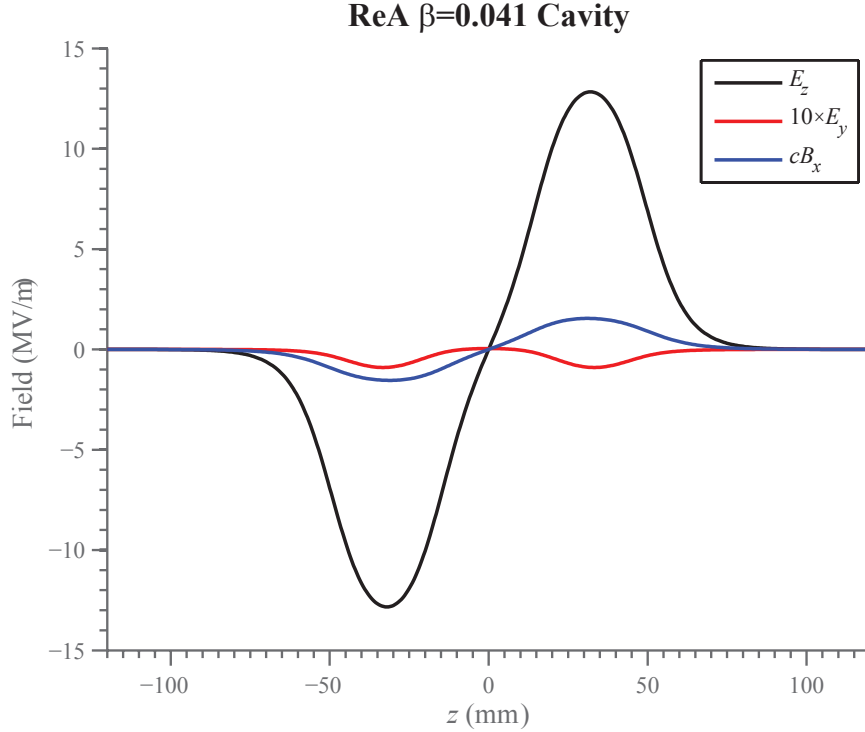


Figure 3.10: ReA $\beta = 0.041$ Cavity Fields, including the accelerating electric field, E_z , and the transverse fields B_x and E_y . Note that E_y is very small, and so therefore has been multiplied by ten for the purposes of this graph.

fields oscillate at the RF frequency of these cavities. From this we can see that at an earlier time, the first gap, located at negative z , would have the positive accelerating E_z field. The longitudinal electric field is asymmetric with respect to z , as is the magnetic field, B_x , while the shape of E_y is symmetric with respect to z . It is also important to note that the magnitude of E_y has been multiplied by 10. For QWR fields, $E_z \gg cB_x \gg E_y$.

3.3.2 Energy Gain

As previously stated, the longitudinal electric field is responsible for the acceleration of the beam. The energy gain through a cavity is given by the following formula:

$$\Delta W = qE_a L \cdot TTF(\beta) \cos \phi, \quad (3.34)$$

where

$$E_a = \frac{1}{L} \int_{-L/2}^{L/2} E_z(z) dz. \quad (3.35)$$

In Equation 3.34, q is the charge, L and ϕ are the cavity length and phase respectively. E_a is the average accelerating electric field, given by equation 3.35 and $TTF(\beta)$ is the transit time factor. The transit time factor gives the relative acceleration for beams traveling at different velocities, as it is a function of β .

3.3.2.1 TTF Calculation

The full definition of the transit time factor is given by equation 3.36.

$$TTF(\beta) = \frac{\int_{-L/2}^{L/2} E_z(z) \cos(\omega t(z)) dz}{\int_{-L/2}^{L/2} E_z(z) dz} \quad (3.36)$$

Assuming that the change in velocity across the gap is small compared with the beam's incoming velocity, $\frac{\Delta v}{v} \ll 1$, the formula for the transit time factor can be simplified. This assumption is valid for velocity gains $\frac{\Delta v}{v} < 10\%$, which cover all cavities in ReA and FRIB.

The lowest velocity beams experience an energy gain increase across one accelerating gap of ~ 0.03 MeV/u out of ~ 0.6 MeV/u. This 5% energy gain corresponds to an $\sim 2\%$ velocity gain, which allows us to eliminate v , and thereby t , as a function of z in Equation 3.36.

Neglecting the change in velocity across the gap, we can rewrite $\omega t(z) = \frac{\omega z}{v} = \frac{\omega z}{\beta c}$ [47].

An analytical solution can then be calculated, which results in Equation 3.37.

$$T_{Ez}(\beta) = \sin\left(\frac{\pi d_{Ez}}{\beta \lambda}\right) \frac{\sin\left(\frac{\pi g_{Ez}}{\beta \lambda}\right)}{\left(\frac{\pi g_{Ez}}{\beta \lambda}\right)} = \sin\left(\frac{\pi d_{Ez}}{\beta \lambda}\right) T_g(\beta, g_{Ez}) \quad (3.37)$$

This form is useful for calculations, and is valid in most practical cases. The gap-to-gap

distance, d_{Ez} , and the gap length, g_{Ez} , are defined by Equations 3.38 and 3.39 respectively. Here α represents each index, while F_α stands in for each field, E_z , E_y , and B_x , respectively.

$$d_\alpha = 2 \frac{\int_0^{L/2} z F_\alpha(z) dz}{\int_0^{L/2} F_\alpha(z) dz} \quad (3.38)$$

$$g_\alpha = 4 \frac{\int_0^{L/2} \left| z - \frac{d_\alpha}{2} \right| F_\alpha(z) dz}{\int_0^{L/2} F_\alpha(z) dz} \quad (3.39)$$

Figure 3.11 shows calculated $TTF(\beta)$ curves for ReA $\beta = 0.041$ and $\beta = 0.085$ QWRs. At each curve's optimal point, the beam has the exact velocity required for the energy gained from the first gap to result in the beam passing between the two gaps in the time that it takes the RF to switch 180° . The distance between the gaps is designed to be $\sim \beta_{opt} \lambda / 2$.

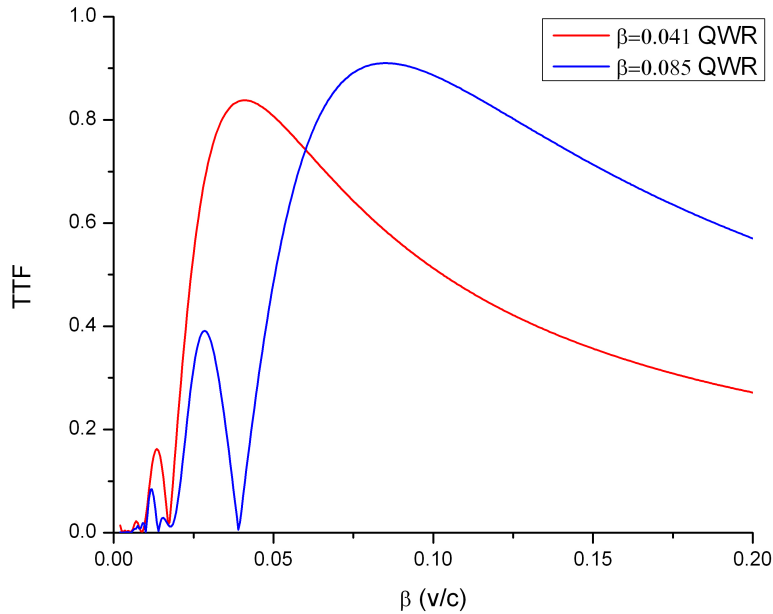


Figure 3.11: TTF of $\beta = 0.041$ and $\beta = 0.085$ cavities

Faster than optimal velocity beams travel between the two gaps of the cavities in less time than it takes RF to fully oscillate 180° , and therefore experience slightly less acceleration

than an optimal velocity beam. In a similar manner, slower than optimal velocity beams take a longer time between the two gaps, resulting in the RF oscillating more than 180° and receiving less acceleration.

Following the curve down from the optimal point to slower and slower velocities to the left, there even comes a point where the curve equals zero. This is at the point where the beam's velocity is such that the transit time between the two gaps results in equal acceleration in the first gap and deceleration in the second gap, for zero total acceleration. The cavities are optimally operated well away from this point.

3.3.2.2 Cavity Geometry

The cavity types that will be utilized at FRIB are called Quarter-Wave Resonators (QWRs) and Half-Wave Resonators (HWRs), as seen in Figure 3.12. As discussed previously, each cavity type is optimized for a certain velocity, at which point the beam experiences the maximum kick at both gaps. This is a function of the distance between the two gaps and the frequency of the RF.

The two types of QWR cavities in ReA have been optimized for $\beta = 0.041$ and $\beta = 0.085$. The $\beta = 0.085$ cavities operate at the same frequency, 80.5 MHz, as the $\beta = 0.041$ cavities, but the spacing between the gaps is larger, resulting in a higher optimal β . The half-wave resonators (HWRs) of FRIB operate at a higher harmonic frequency, 322 MHz, and have been optimized for $\beta = 0.29$ and $\beta = 0.53$.

The difference in gap spacing between the cavity types can clearly be seen in Figure 3.12. The inner conductor, which comes down through the center of the cavity, is noticeably larger in the $\beta = 0.085$ cavity from the $\beta = 0.041$ cavity, thereby optimizing the transit of a faster beam. The inner conductor shields the beam from experiencing the cavity fields when the

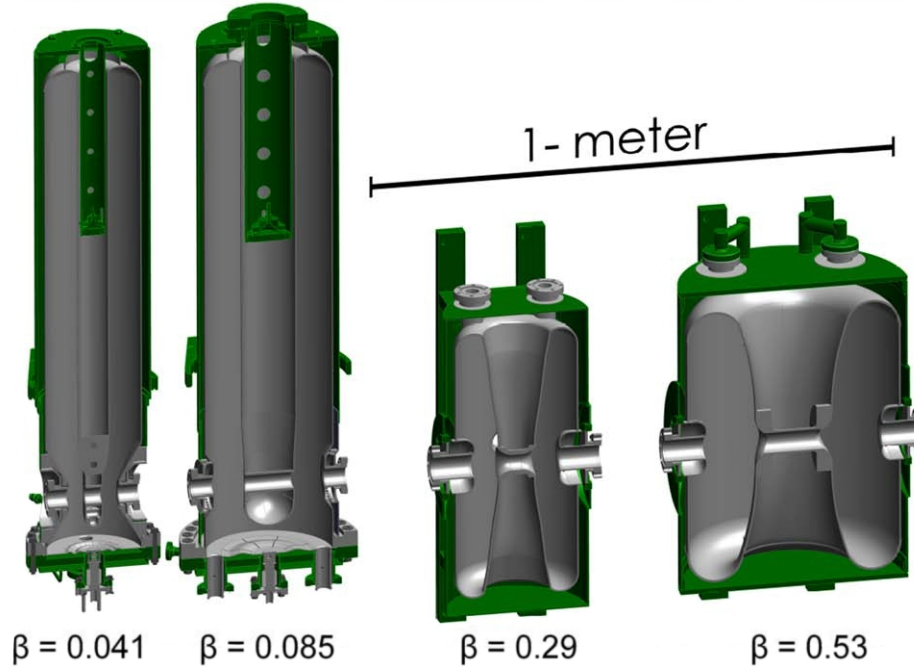


Figure 3.12: QWR and HWR Cavities [29]. The QWR cavities operate at 80.5 MHz, while the HWR cavities operate at 322 MHz.

RF is changing. The same is true for the HWR cavities.

If the beam were allowed to see the fields continuously, it would be accelerated and decelerated the same amount, resulting in no net acceleration. The longitudinal electric field, oscillating back and forth between pointing in the positive, and then negative, z -direction, is shielded by the cavity geometry from the beam when it is pointing in the negative z -direction. In this way, the beam can be accelerated in both gaps as it passes through the cavity.

3.3.3 Focusing Effects

As the beam passes through the cavity, recall that it experiences not only the accelerating longitudinal electric field, E_z , but also transverse fields. Figure 3.13 depicts schematically the electric field lines present in an RF gap. As the beam's position deviates off the central axis, the transverse components of the electric field are seen in addition to E_z .

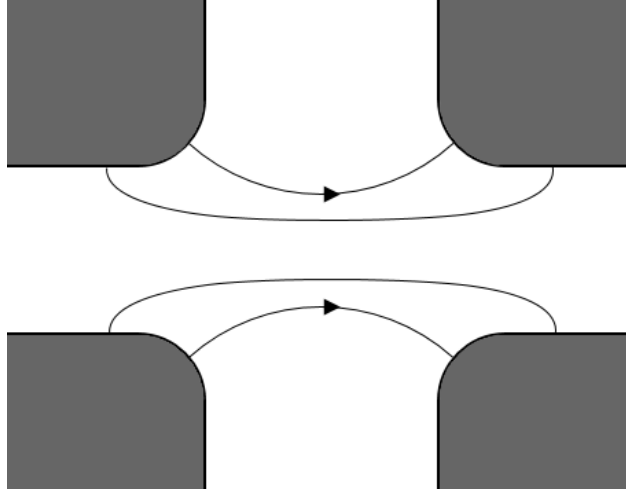


Figure 3.13: Electric field lines in an RF gap.

The radial electric field, E_r , has the opposite sign of E_z following from Maxwell's equation $\nabla \cdot \vec{E} = 0$, or in cylindrical coordinates, $\frac{1}{r} \frac{\partial(rE_r)}{\partial r} + \frac{\partial E_z}{\partial z} = 0$. This leads to the fact that when the electric field is accelerating the beam, as in Figure 3.10 for positive z , E_z is decreasing with respect to z toward the end of the gap, meaning E_r must be positive. This is the case of RF defocusing [47].

The transverse focusing, with the cavity modeled as a thin lens, can therefore be calculated as having a strength k_r as given in Equation 3.40.

$$k_r = \frac{\pi q E_z TTF(\bar{\beta}) L f \sin(-\phi)}{c E_r (\bar{\beta} \bar{\gamma})^2} \quad (3.40)$$

Note that this quantity is negative, indicating transverse defocusing. The longitudinal focusing has the opposite sign from the transverse defocusing, as given in Equation 3.41.

$$k_z = -2k_r \bar{\gamma}^2 \quad (3.41)$$

With the cavity changing the energy of the beam, these quantities have been calculated

at the midpoint of the cavity, using the beam's energy at the midpoint of the cavity, \overline{W} to calculate $\bar{\gamma} = 1 + \frac{\overline{W}}{E_r}$, and then $\bar{\beta} = \sqrt{1 - \frac{1}{\bar{\gamma}^2}}$. It is important that $\bar{\beta}$ is not calculated as the average of β_i and β_f , as β is not linear and therefore this will not yield the correct result.

In addition to these focusing effects, quarter-wave resonator cavities are known to steer the beam vertically due to fields present from the asymmetry of this cavity type with respect to the beampipe. This effect is very important to study, as it has been previously calculated but not measured. This will be discussed in more detail in Chapter 4, along with presentation of measurement data taken at ReA investigating this effect.

3.3.4 Benchmark Considerations

Multi-particle tracking through simulated fields is one method of beam line modeling that is used, while another is a thin-lens adaptation for matrix modeling. Multi-particle tracking is crucial for studying higher-order effects, while matrix modeling is utilized in many cases where speed of calculation is a factor, such as with on-line modeling, or studies with large variable spaces to explore.

The energy gain from an RF cavity is the one of the first things to investigate when comparing cavity models in multi-particle tracking codes with cavity models in envelope matrix models. As previously discussed, the energy gain imparted to a beam from an RF cavity is a function of the beam's charge to mass ratio, and the cavity's voltage, phase and geometry, as given by Equation 3.34. The geometry of the cavity determines its transit time factor, or TTF , which is a function of the cavity's efficiency with respect to beam velocity.

3.3.4.1 TTF Computation

Many multi-particle tracking codes, such as IMPACT, look up TTF values in a table, interpolating for points in between. Other codes, such as matrix-based XAL, fit a high-order polynomial to the region of interest, and use this polynomial and its derivative to calculate the TTF to use. Seemingly small differences between these two methods can result in large differences in the overall energy gain calculated, so it is important to study this carefully in order to make sure both codes are using the same values when benchmarking the codes.

This is particularly important when the TTF is changing rapidly, as is the case when entering the third cryomodule at ReA. In Figure 3.14, note that where the transition between the the $\beta = 0.041$ and $\beta = 0.085$ cavities takes place, at $\beta \approx 0.05$, the $\beta = 0.085$ TTF curve is much steeper than the curve for the $\beta = 0.041$ TTF , which is fairly flat.

The small difference in energy gain as calculated by the two models for one cavity may not be a large effect, $\lesssim 1\%$, but when there are multiple cavities one after another, such as in a linac, these errors compound and can produce increasingly inaccurate results.

3.3.4.2 Thin-lens Modeling

One final aspect to consider when benchmarking the energy gain through an RF cavity between the two types of modeling methods involves the intrinsic difference between the modeling methods. Multi-particle tracking follows the beam smoothly through the changing cavity fields, resulting in a smooth energy gain profile, while the matrix representation of a cavity models the energy gain as a thin-lens, with a single kick at the center of the cavity, or with two kicks located at the cavity's physical gap locations. Figure 3.15 shows the difference in energy gain profiles between the smooth multi-particle tracking model and the two-gap thin-lens matrix model.

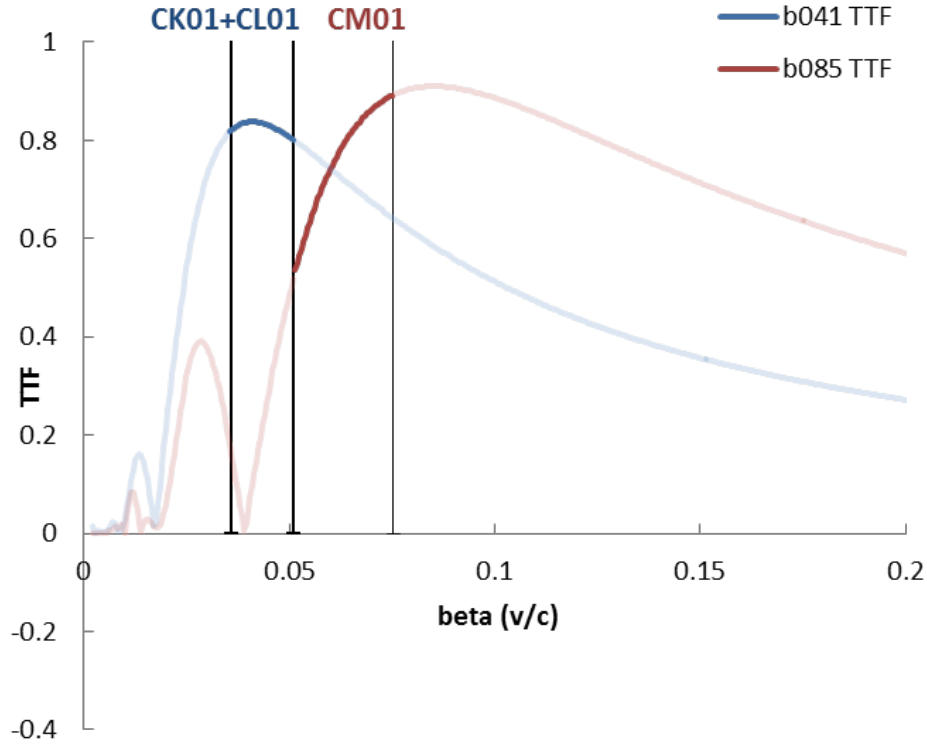


Figure 3.14: ReA TTF for $\beta = 0.041$ and $\beta = 0.085$ cavities, with operating regimes highlighted. The $\beta = 0.041$ cavities are located in the first two cryomodules, CK01 and CL01, while the $\beta = 0.085$ cavities are located in the third cryomodule, CM01.

When modeling the second gap kick, the relative phase between the two gaps has to be calculated. Since the envelope for the reference particle is being modeled, it should arrive at the design phase (nominally -20° for ReA). This is accomplished by running the matrix model twice, first calculating the energy gain and correct phases for the cavities, and finally using these correct phases to track the beam through the lattice.

For simplification, the one-kick model at the midpoint of the cavity is often used instead as it produces nearly identical results. Moreover, the one-kick model reflects the fact that the thin-lens model is used simply as an approximation to the real-field. When speed of calculation is crucial, the simplest reliable model is desired, and so the thin-lens model is appropriate in these cases.

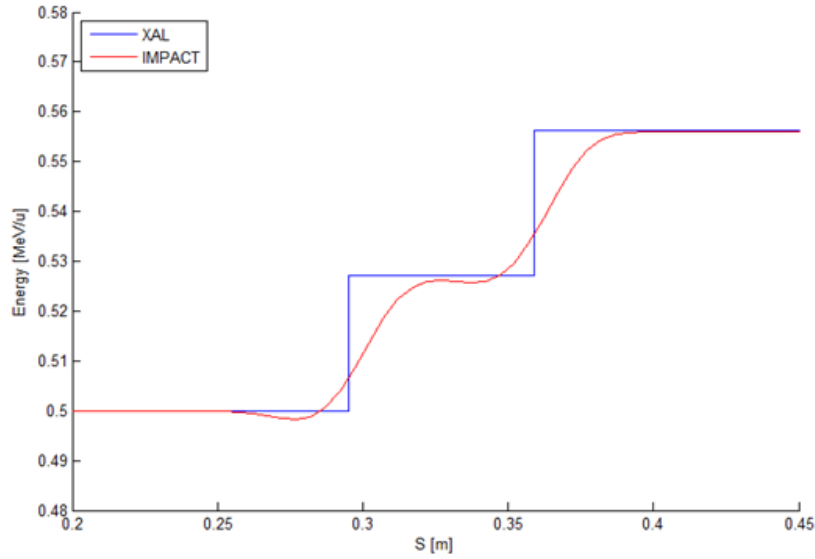


Figure 3.15: Modeling two gap acceleration in XAL as compared with IMPACT for a $\beta = 0.041$ accelerating cavity.

3.4 Lattice Examples

With the models established for the linac beam line elements, solenoid and RF cavities, the full accelerator lattice can now be modeled for various beams and machine settings. It is also important to benchmark the results of multi-particle tracking, which uses full field profiles in its modeling, with that of the simplified matrix method approach which only include linear terms, and is therefore a linear approximation.

After many benchmarking considerations have been handled, as discussed in Section 3.3.4, a reliable model can finally be established for the linac in question. This section will present models for both the ReA and FRIB linacs which have been benchmarked in XAL, a matrix modeling code, against the design code, IMPACT, a multi-particle tracking code.

3.4.1 ReA Linac

The solenoid focusing results shown in Section 3.2 in Figure 3.5 was for the case of an RFQ energy beam, 0.6 MeV/u , without any cavities turned on. In the case where the cavities are on, we also need to make sure that the energy gain is modeled correctly, as well as the beam size. Using the models previously discussed for both the solenoids and RF cavities, the ReA linac can be accurately modeled.

Figure 3.16 shows the benchmarking modeling result for a H_2 beam, $Q/A = 0.5$. The nominal settings for this beam are modeled with the first rebunching cavity on and the $\beta = 0.041$ cavities set at 16 MV/m and $\phi = -20^\circ$ accelerating phase. In XAL, the solenoid hard-edge effective lengths and field strengths are calculated through the parameterization discussed in Section 3.2.1 using the real measured field profiles. The $\beta = 0.041$ cavities are modeled using the single-kick “thin-lens” model.

The benchmarking result of modeling the ReA linac in Figure 3.16 shows XAL’s calculation in red as compared with the design lattice model run from IMPACT in blue. Through thick elements, such as the solenoids, IMPACT outputs results at the beginning and end of the elements, while XAL tracks through the thick elements. This is the reason for the difference between the display of the two curves. A good agreement is found for transverse and longitudinal motion, as well as energy gain through the cavities. Slight discrepancies in the longitudinal plane are expected due to the inherent differences in the modeling methods.

3.4.2 FRIB Linac Segment 1

The benchmark results for FRIB’s Linac Segment 1 between IMPACT and XAL using a single kick at the center of the cavity, the “thin-lens” model, is shown in Figure 3.17. Note

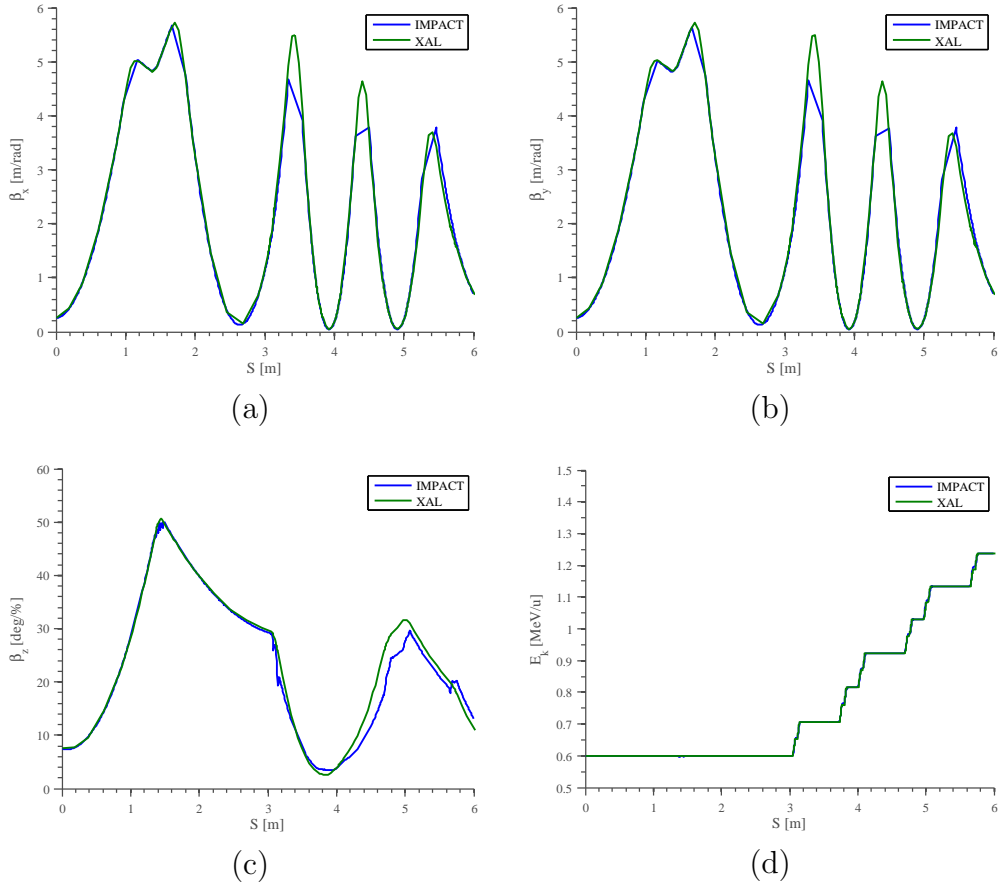


Figure 3.16: Benchmarking results of the ReA linac through its second cryomodule show good agreement between the matrix modeling code XAL, and the multi-particle tracking code IMPACT. Plots show the results for transverse β functions (a) β_x and (b) β_y , longitudinal β function (c) β_z , and finally the kinetic energy per nucleon, (d) E_k .

that in this example, the phases for the matching cavities for the transition between the $\beta = 0.041$ cavities and the $\beta = 0.085$ cavities had to be adjusted in order to account for the difference in TTF values calculated, as discussed earlier in Section 3.3.4.

FRIB's Linac Segment 1 (LS1) consists of 16 $\beta = 0.041$ cavities, 96 $\beta = 0.085$ cavities, and 44 superconducting solenoids. The energy for the nominal case of a U^{33+} beam through LS1 increases from 0.3 MeV/u to 16.6 MeV/u. FRIB's Folding Segment 1 (FS1) is also modeled, which brings the beam through a 180° bending section after a stripper foil which increases the beam's charge state from 33 – 34+ to 76 – 80+ for more efficient subsequent acceleration.

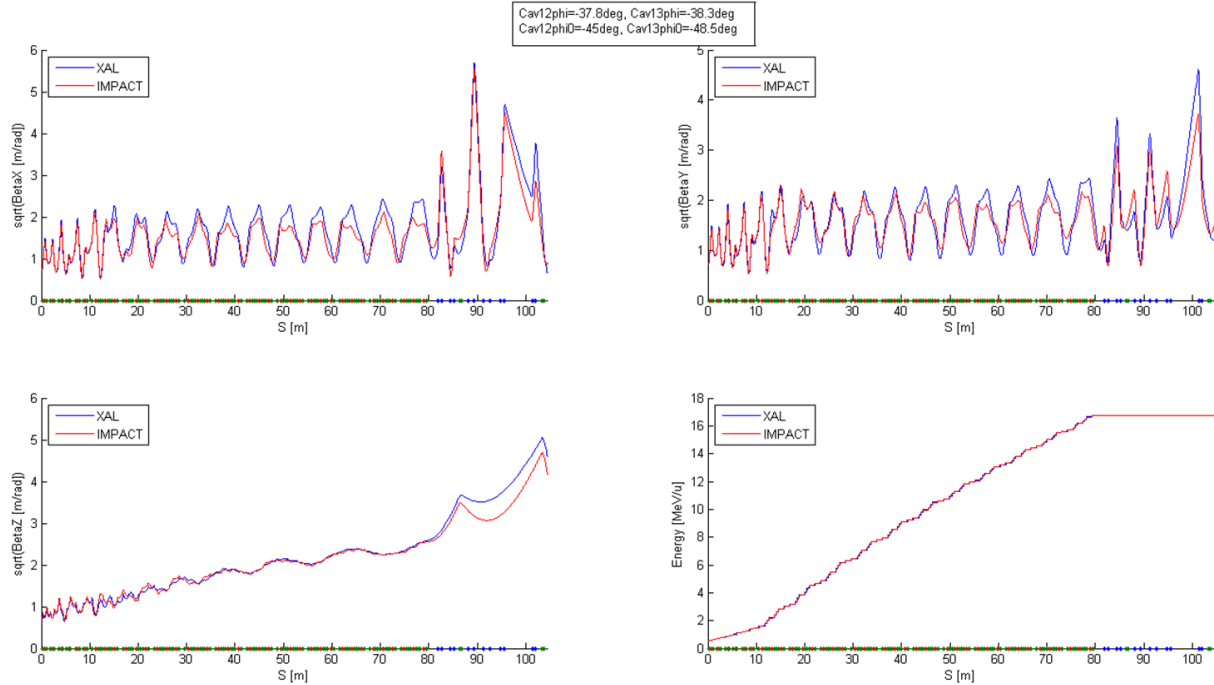


Figure 3.17: XAL Cavity Benchmark with IMPACT for a U^{33+} beam through FRIB's Linac Segment 1 to the Stripper Foil, including modeling of $\beta = 0.041$ and $\beta = 0.085$ cavities.

The nominal design for FRIB's LS1 and FS1 actually transports both U^{33+} and U^{34+} to satisfy the increased beam intensity requirements of modern experiments. The concept and challenges associated with multiple charge state transport are presented in the next section.

3.5 Multiple Charge State Transport

There are many challenges associated with multiple charge state transport, but this method of beam delivery is essential in order to attain the high currents required by modern experiments. A brief summary of the history of multiple charge state transport is presented in this section, followed by the methodology and benchmarking process of matrix modeling methods. Multi-particle tracking results of multiple charge state simulations in the FRIB Linac Segment 1 beam line (LS1) have been used as the basis for the benchmarking process. As stated before,

it is important to model multiple charge states with a matrix based model in the case of an on-line model, where the speed and performance of the calculation becomes an issue. For this purpose, the slower multi-particle tracking simulations are no longer a viable option.

3.5.1 Background

One of the primary performance criteria for FRIB's driver linac beam is to deliver beams with energy greater than 200 MeV/u with high beam currents of ~ 400 e μ A. During the design of FRIB, modern ECR ion sources were able to produce enough current in a single charge state to satisfy these requirements for all ion species up to *Xe* [29]. However, even the best sources, such as VENUS at Lawrence Berkeley National Lab (LBL), were only able to deliver ~ 200 e μ A of U^{33+} or U^{34+} [48] as of 2008. Therefore, ion beams heavier than *Xe* required design of simultaneous transport of at least two charge states in order to achieve the power requirements of FRIB. Improvements in beam development have resulted in state-of-the-art ECR ion sources producing ~ 400 e μ A of U^{33+} or U^{34+} which meets the requirement for single charge state transport [49], however multiple charge state transport is still an important technique that may be used for increasing the delivered beam current on target.

Experimenters at Argonne National Lab (ANL) in 2007 set up ECR-LEBT beam line sufficient for the study of transport and merging of multiple charge state *Bi* beams [50]. The setup consisted of an ECR ion source, a 100 keV platform and a Low Energy Beam Transport section, designed as an injector for a high-intensity heavy-ion linac, such as FRIB.

In 2008, they successfully demonstrated the separation and recombination of $^{209}Bi^{20+}$ and $^{209}Bi^{21+}$ [51]. Figure 3.18 shows the simultaneous transport of both charge states on the left, as well as a superimposed image of the transport of each charge state individually. This is an important proof-of-concept that two charge states can be transported simultaneously to

effectively double the beam intensity.

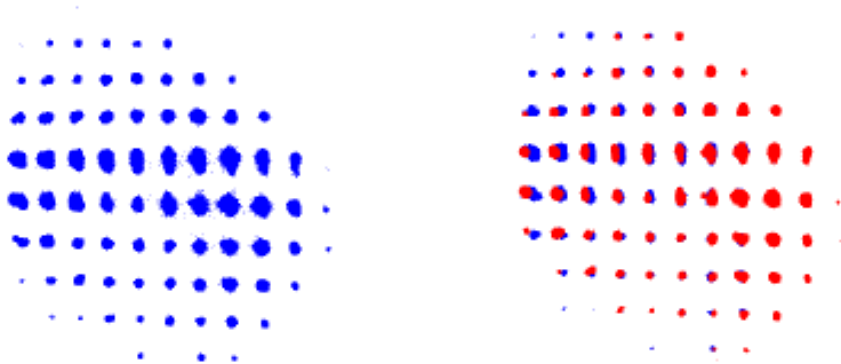


Figure 3.18: Results from ANL multiple charge state transport: pepper-pot image of the combined bismuth beam with charge states 20+ and 21+ (on the left) and superimposed images of $^{209}\text{Bi}^{20+}$ (blue) and $^{209}\text{Bi}^{21+}$ (red) beams transported individually (on the right) [51].

Multiple charge beam dynamics have been studied further in acceleration through an RFQ [52] and through an ion linac [53]. The verification of multiple charge state beams from an ECR ion source doubling the intensity of a high quality heavy-ion beam is highly encouraging, and motivates this technique as an option for FRIB to utilize for its heavy-ion beams.

3.5.2 Methodology

The following is a description of a method that can be used to model multiple charge state beams with a matrix envelope calculation instead of multi-particle tracking. The principle lies in tracking individual charge states, followed by a step where these individual charge states are combined in order to get the total extent of the beam. This approach is valid as long as beam-beam effects, such as space charge or interaction between the individual charge states can be neglected. This is appropriate for the cases we will consider, and, in fact, multi-particle tracking also ignores these effects. The space charge potential or other

higher order terms can be accounted for, but we constrain this section's discussion to the methodology of transporting multiple charge states in regions where these effects can be neglected.

To begin with, we track the reference charge state. In the case of the FRIB driver linac, for U₂₃₈ this would be the 33+ charge state. This step is performed like any other matrix model simulation of a single charge state beam. We then track each additional charge state with respect to this reference charge state orbit, as established in the first run.

In order to do this, we need to carefully consider elements that change the beam's energy, such as the accelerating cavities. In order to handle the case of modeling the cavities correctly for multiple charge states, it is necessary to calculate $\Delta\phi$ for each different charge state at each cavity with respect to the reference charge state. As the energy gain (given in Equation 3.34) depends on the charge, q , each additional charge state will have slightly different energies than the reference charge state. This means that they will arrive at slightly different times, and therefore slightly different phases, at each cavity. The equation for calculating the time of flight for each charge state is given in Equation 3.42.

$$t_i = \frac{d}{c \sqrt{1 - \frac{1}{\gamma_i^2}}} \quad (3.42)$$

Charge states gain different amounts of energy based on their different charge and also based on their different arrival times to the cavity gaps which results in them experiencing different cavity phases. As higher charge states gain more energy through the first gaps, they arrive earlier at the subsequent gaps which means they experience a lower phase and therefore gain less energy than the lower charge states. This continues until they have roughly the same energy at which point the process repeats itself, with higher charge states gaining more

energy than the lower charge states. This results in a longitudinal simple harmonic motion of the charge states about the nominal charge state.

We can then calculate the change in arrival time of the additional charge states from the reference charge state, $\Delta t_i = t_i - t_0$, which gives the change in RF phase that the charge state will experience in the cavity, $\Delta\phi_i = \omega_{\text{RF}}\Delta t$. Using this formula, we get the result for the energy gain that the different charge states experience in Equation 3.43.

$$\Delta E_i = \frac{Q_i}{A} e E T L \cos(\phi + \Delta\phi_i) \quad (3.43)$$

This formula gives the total energy gain for each charge state, with the reference charge state experiencing an energy gain of ΔE_0 , calculated using the reference charge state Q_0 and at the reference phase such that $\Delta\phi_0 = 0$. We might expect at first glance that because the higher charge states will get a larger energy gain due to their higher Q , that they would receive more energy than the reference charge state overall, while the the opposite would be true for the lower charge states. We can model this with FRIB Linac Segment 1 (LS1), where the reference beam is U^{33+} . Additional charge states are shown for $\Delta Q = \pm 1, \pm 2$. For practical purposes FRIB LS1 has only been designed to accelerate two charge states, $Q = 33+$ and $34+$, but the goal here is to show the characteristics of the energy gain of multiple charge states simultaneously, so we have included more charge states to illustrate this effect.

This result is shown in Figure 3.19 on the left, where $\Delta\phi = 0$. However, if the higher charge states arrive earlier to the next cavity because of a larger energy gain from the initial cavity, they consequently see a lower cavity phase (which would be rising to the ideal accelerating phase, for example -20°) and get a lower energy gain from the second cavity. The opposite happens for lower charge states than the reference charge state. This bunches

the beams longitudinally, and keeps the energies of the additional charge states oscillating about the reference charge state’s energy. The same stability condition that works for one charge state, which is why accelerating cavities are operated at a phase off from the crest, as discussed in Section 2.2, operates in the same way for multiple charge states. We see that when we include $\Delta\phi$ in the calculation in order to account for the difference in arrival times of the different charge states, we get the correct result as seen in the right of Figure 3.19.

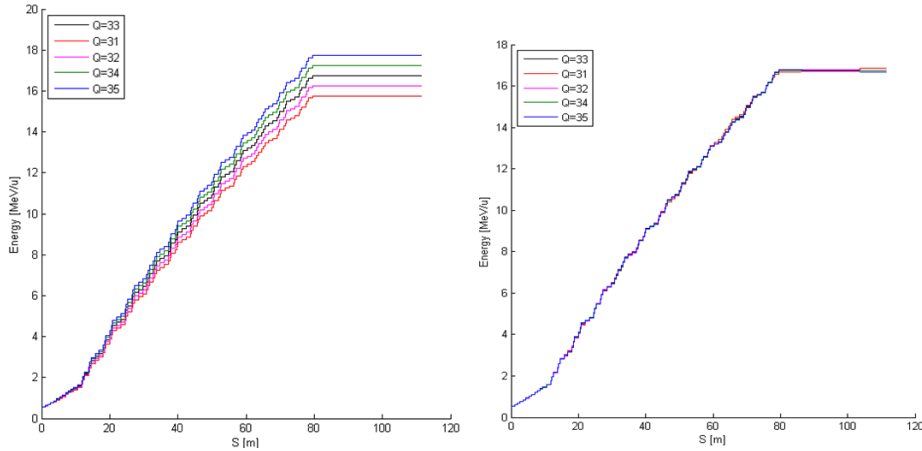


Figure 3.19: Multiple Charge State Energy Gain: $\Delta\phi = 0$ on left, $\Delta\phi = \omega_{RF}\Delta t$ on right. As discussed in the text, modeling the separate charge states with $\Delta\phi = 0$ yields the unphysical result where each charge state arrives at the accelerating phase of the reference charge state, resulting in higher charge states receiving higher energy gains and lower charge states receiving lower energy gains than the reference charge state. Instead, each individual charge state’s arrival time at each cavity must be calculated in order to correctly model the multiple charge state’s energy gain, as seen here on the right.

Another element that has to be treated carefully are bending dipoles, which change the beam’s reference orbit. In order to calculate the separation of charge states through bend elements, we need to account for the different bend radii of the different charge states. It is clear that the different charge states will each have its own bend radius from the fact that each charge state has a different rigidity, $B\rho_i = \frac{p_i}{q_i}$. In order to calculate the position of each charge state’s beamlet with respect to the reference charge state’s orbit, we must shift the beam centroid of the addition charge state’s calculation off by the amount that is

calculated to occur in theory. This way when plotting the results, each charge state will have the same reference orbit, instead of setting its own trajectory through the the dipole as zero. Charge states spread apart in dipoles because of their different rigidities. In order to get the correct dispersion, each additional charge state is given an offset to its average momentum in the bend axis coordinate plane which is calculated from the difference in rigidities. We can accomplish this by modifying an element in XAL's 7×7 sigma matrix, defined by Equation 3.44 [54].

$$\sigma = \begin{pmatrix} \langle x^2 \rangle & \langle xx' \rangle & \langle xy \rangle & \langle xy' \rangle & \langle xz \rangle & \langle xz' \rangle & \langle x \rangle \\ \langle xx' \rangle & \langle x'^2 \rangle & \langle x'y \rangle & \langle x'y' \rangle & \langle x'z \rangle & \langle x'z' \rangle & \langle x' \rangle \\ \langle xy \rangle & \langle x'y \rangle & \langle y^2 \rangle & \langle yy' \rangle & \langle yz \rangle & \langle yz' \rangle & \langle y \rangle \\ \langle xy' \rangle & \langle x'y' \rangle & \langle yy' \rangle & \langle y'^2 \rangle & \langle y'z \rangle & \langle y'z' \rangle & \langle y' \rangle \\ \langle xz \rangle & \langle x'z \rangle & \langle yz \rangle & \langle y'z \rangle & \langle z^2 \rangle & \langle zz' \rangle & \langle z \rangle \\ \langle xz' \rangle & \langle x'z' \rangle & \langle yz' \rangle & \langle y'z' \rangle & \langle zz' \rangle & \langle z'^2 \rangle & \langle z' \rangle \\ \langle x \rangle & \langle x' \rangle & \langle y \rangle & \langle y' \rangle & \langle z \rangle & \langle z' \rangle & \langle 1 \rangle \end{pmatrix} \quad (3.44)$$

The seventh row and column in XAL's sigma matrix refer to the respective centroids of the beam which transform linearly with the other beam moments, $\langle x^2 \rangle$, xx' , etc. The beam sigma matrix, σ , given in Equation 3.44, transforms according to Equation 3.45, where M is the transfer matrix. The transfer matrix in its general form is Equation 3.46.

$$\sigma_1 = M\sigma_0M^T \quad (3.45)$$

$$M = \begin{pmatrix} (x|x) & (x|x') & (x|y) & (x|y') & (x|z) & (x|z') & (x|\langle x \rangle) \\ (x'|x) & (x'|x') & (x'|y) & (x'|y') & (x'|z) & (x'|z') & (x'|\langle x' \rangle) \\ (y|x) & (y|x') & (y|y) & (y|y') & (y|z) & (y|z') & (y|\langle y \rangle) \\ (y'|x) & (y'|x') & (y'|y) & (y'|y') & (y'|z) & (y'|z') & (y'|\langle y' \rangle) \\ (z|x) & (z|x') & (z|y) & (z|y') & (z|z) & (z|z') & (z|\langle z \rangle) \\ (z'|x) & (z'|x') & (z'|y) & (z'|y') & (z'|z) & (z'|z') & (z'|\langle z' \rangle) \\ (\langle x \rangle|x) & (\langle x' \rangle|x') & (\langle y \rangle|y) & (\langle y' \rangle|y') & (\langle z \rangle|z) & (\langle z' \rangle|z') & 1 \end{pmatrix} \quad (3.46)$$

The notation in Equation 3.46, $(x|x')$ for example, simply refers to the relevant component of M which gives the dependence of x on x' through the element being modeled by matrix M . These terms depend on the fields present inside the element, and can be calculated as shown earlier in this chapter.

If we consider the case of a horizontally bending dipole, where we expect the x -position of the beam to spread out, we can look at the reference charge state's average position in x , $\langle x \rangle$, as a function of the matrix elements for a dipole, and the vector representing the beam centroid, the seventh column in the σ matrix. This equation is given in 3.47.

$$\begin{aligned} \langle x \rangle_1 = & (\langle x \rangle|x) \langle x \rangle_0 + (\langle x \rangle|x') \langle x' \rangle_0 + (\langle x \rangle|y) \langle y \rangle_0 + (\langle x \rangle|y') \langle y' \rangle_0 \\ & + (\langle x \rangle|z) \langle z \rangle_0 + (\langle x \rangle|z') \langle z' \rangle_0 + (\langle x \rangle|x) \end{aligned} \quad (3.47)$$

For our charge states, $\langle x \rangle_0 = \langle x' \rangle_0 = 0$. The dipole transfer matrix also has $(\langle x \rangle|y) = (\langle x \rangle|y') = (\langle x \rangle|z) = (\langle x \rangle|x) = 0$. This leads to the only nonzero element contributing from the dipole to be $(\langle x \rangle|z)$. The formula for this term for an additional charge state is given in Equation 3.48. Here the definition of magnetic rigidity, $B\rho [\text{T} \cdot \text{m}] = \frac{10p[\text{GeV}/c]}{2.9979Q}$ [34], has been used to solve for ρ . In Equation 3.48 all quantities are given for the additional charge

state, such that $\theta = \frac{L}{\rho} = \frac{eBL}{pc}$. The only contributing element from the σ matrix is then $\langle z \rangle_0$. This formula is given in Equation 3.49. Here, “ref” indices indicate the reference charge state, while all other quantities are given for the additional charge state being calculated.

$$(\langle x \rangle | z) = \rho (1 - \cos \theta) = \frac{10p_0}{2.9979Q_0B} (1 - \cos \theta) \quad (3.48)$$

$$\langle z \rangle_0 = \frac{1}{\gamma_0^2} \frac{\Delta B \rho}{B \rho_{\text{ref}}} = \frac{1}{\gamma_0^2} \frac{Q_{\text{ref}}}{\sqrt{\gamma_{\text{ref}}^2 - 1}} \left(\frac{\sqrt{\gamma_0^2 - 1}}{Q_0} - \frac{\sqrt{\gamma_{\text{ref}}^2 - 1}}{Q_{\text{ref}}} \right) \quad (3.49)$$

The full simulation for FRIB Linac Segment 1 (LS1) using XAL for U^{33+} and U^{34+} is given in Figure 3.20. A close up of the end of FS1, which has a chicane, or dogleg, consisting of four dipoles, bending 5° each, is shown in Figure 3.21. This chicane section is included in the beam line design to eliminate a direct line-of-sight of the beam path between the stripper foil and the linac. This precaution protects the accelerating cavities from any stray particles emitting from the collisions at the stripper foil, which would decrease the cavity’s performance if they happened to hit the cavity’s surface.

Notice that in the bottom graph of Figure 3.21 for U^{33+} , the reference charge state, $\langle x \rangle = 0$. This is the reference orbit from which the deviation for U^{34+} is calculated in the red plot. We can see that this beamlet spreads out by almost 1.5 mm from the reference charge state, and returns to ~ 0 mm by the end of the chicane. We can also note that the beamsize, σ_x remains small for each charge state, but the combination grows as they spread apart in the first dipole, and come back together through the rest of the chicane. The averages of these charge states as plotted is the sum of the distributions of the individual charge states which is derived in the following manner.

Each charge state can be modeled in each phase space (x, y, z) as a Gaussian distribution

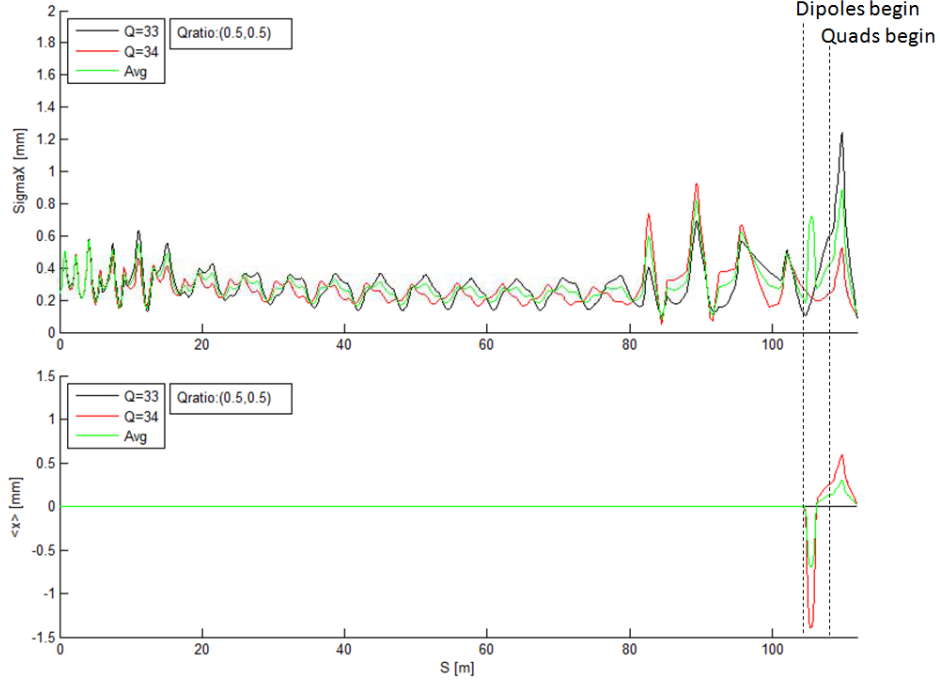


Figure 3.20: FRIB Linac Segment 1 as simulated by XAL for U^{33+} and U^{34+} charge states, as well as the result of the two charge states combined.

with its average equaling the centroid location, μ , and a standard deviation of σ . These Gaussian distributions for each charge state can be added together to form a Gaussian description of the combined beamlets which form the total beam. Equation 3.50 gives the formula for adding multiple Gaussian functions. This Gaussian description of the total beam is used to determine the center of mass of the beamlets, as well as the standard deviation of their distribution, and is not intended to describe the actual distribution of the beam. A schematic representation of the distributions being added is shown in Figure 3.22.

$$f_{\text{tot}}(x) = \sum_i \frac{N_i}{\sigma_i \sqrt{2\pi}} e^{-\frac{1}{2} \left(\frac{x - \mu_i}{\sigma_i} \right)^2} \quad (3.50)$$

The standard deviation of this distribution is the square root of the normalized variance of the function f_{tot} , defined by Equation 3.51, where μ_{tot} is the mean of the distribution.

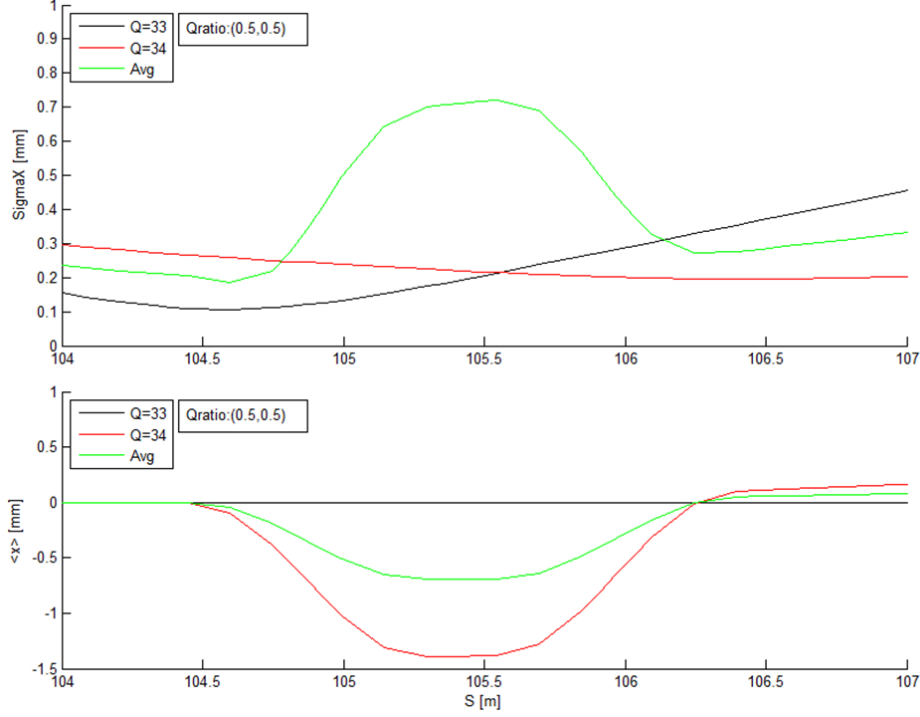


Figure 3.21: End of FRIB Linac Segment 1 chicane as simulated by XAL for U^{33+} and U^{34+} charge states, as well as the result of the two charge states combined.

The mean of the total distribution is the weighted average of the individual gaussian peaks, as given in Equation 3.52.

$$\sigma_{\text{tot}}^2 = \langle x^2 \rangle_{\text{tot}} = \frac{\int_{-\infty}^{\infty} (x - \mu_{\text{tot}})^2 f_{\text{tot}}(x) dx}{\int_{-\infty}^{\infty} f_{\text{tot}}(x) dx} \quad (3.51)$$

$$\mu_{\text{tot}} = \langle x \rangle_{\text{tot}} = \frac{\sum_i N_i \mu_i}{\sum_i N_i} \quad (3.52)$$

Plugging Equation 3.50 into Equation 3.51 and making the substitution $u = x - \mu_{\text{tot}}$, with $du = dx$, the formula for σ_{tot}^2 is simplified to Equation 3.53. Note here that the fact that integration of a Gaussian distribution over all space being normalized to one has been

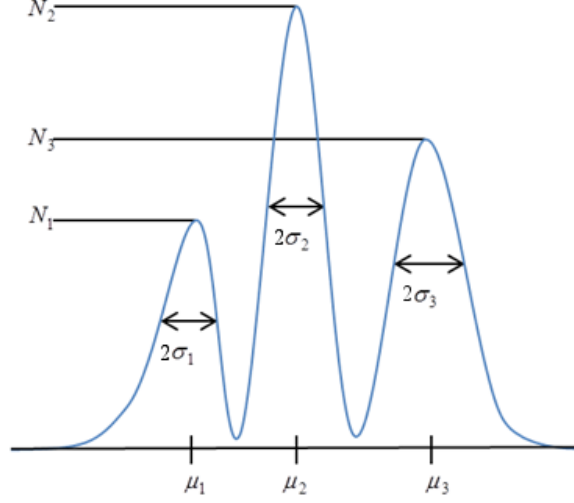


Figure 3.22: Schematic representation of three beamlets with means μ_i , standard deviations σ_i , and intensities N_i

used to simplify the denominator.

$$\sigma_{\text{tot}}^2 = \frac{1}{\sum_i N_i} \left[\sum_i \frac{N_i}{\sigma_i \sqrt{2\pi}} \int_{-\infty}^{\infty} \left(u^2 + 2u(\mu_i - \mu_{\text{tot}}) + (\mu_i - \mu_{\text{tot}})^2 \right) du \right] \quad (3.53)$$

Performing the integrals using $\int_{-\infty}^{\infty} x^n e^{-ax} dx = \frac{2(n!)}{a^{n+1}}$ results in Equation 3.54. Simplifying the terms, completing the square, and taking the square root yields the final result for the standard deviation in Equation 3.55.

$$\sigma_{\text{tot}}^2 = \frac{1}{\sum_i N_i} \left[\sum_i \frac{N_i}{\sigma_i \sqrt{2\pi}} \left(\sqrt{\pi} (1!) 2^{-1} (2\sigma_i^2)^{3/2} + 2(\mu_i - \mu_{\text{tot}}) \sqrt{\pi} (0!) 2^{-1/2} (2\sigma_i^2)^1 + (\mu_i - \mu_{\text{tot}})^2 \sigma_i \sqrt{2\pi} \right) \right] \quad (3.54)$$

$$\sigma_{\text{tot}} = \sqrt{\frac{\sum_i N_i (\sigma_i + (\mu_i - \mu_{\text{tot}}))^2}{\sum_i N_i}} \quad (3.55)$$

This equation for σ_{tot} along with Equation 3.52 for μ_{tot} define the distribution of the

charge states. By using these equations, individual charge states can be run through a matrix modeling code and the resulting individual distributions can be combined to define the total combined distribution of the charge states. Again, this means of describing the beam is intended to be used for determining the centroid motion of the combined charge states as well as their relative distribution size as a means to compare multiple charge state transport to the modeling of a single charge state, and is not intended to represent the physical distribution of the beam.

Now that this methodology has been implemented in XAL, in order to validate this method, the results must be benchmarked with a multi-particle tracking code, such as IMPACT. The results from this benchmarking procedure are presented in the following section.

3.5.3 Benchmark

The FRIB Folding Segment 1 (FS1) to the Stripper Foil is an ideal beam line to use as a benchmark for this method, as it contains both matching cavities and bending dipoles where the separation of charge states can be seen. The results are shown in Figure 3.23.

This method has been shown to agree with the results from the multi-particle tracking code, IMPACT. The XAL run and plotting only takes a few seconds to complete, compared with IMPACT that can take minutes to run. This makes XAL a feasible option for an on-line model. With this benchmark complete, the only part left to implement would be to include this new multiple charge state run capability into an established modeling code such as XAL.

A schema is given in Figure 3.24 which represents how this would be easy to realize. The left-hand side of the diagram in Figure 3.24 depicts how a single charge state XAL model run is accomplished presently. The XAL QS1 model run populates the XAL object from which applications draw the relevant beam modeling parameters.

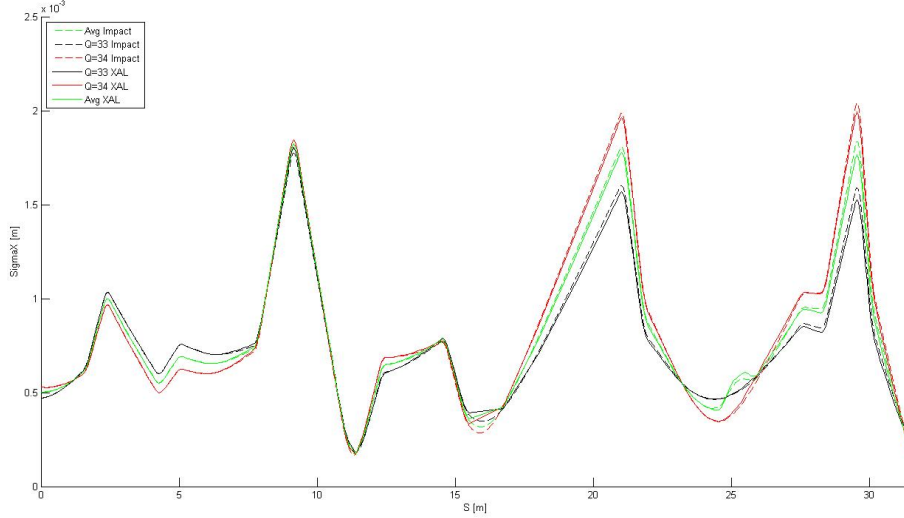


Figure 3.23: Results of XAL and IMPACT calculations for FRIB FS1 to Stripper. The IMPACT results are shown with dashed lines, while the XAL results are shown with the solid lines.

Multiple charge state XAL model runs may easily be implemented by wrapping the summing and $\langle z' \rangle$ routines around individual XAL runs of different charge states. This is depicted in the right-hand side of the diagram in Figure 3.24. In this way, the XAL QS1 model run is used to calculate $\langle z' \rangle$ for the subsequent model runs, XAL QS2 ... XAL QSN. The final result from each model run is given as input to the summing routine, which populates a single XAL object, mirroring the single charge state XAL model run method.

Consequently, applications would be able to run multi-charge state modeling in XAL with the advantage that there is no need for major source code editing, as the layer between applications and the XAL object remains unaltered. Although this method should be simple to implement, this development has been postponed until the OpenXAL collaboration is able to use this functionality, in order to reduce duplication of effort as the code develops.

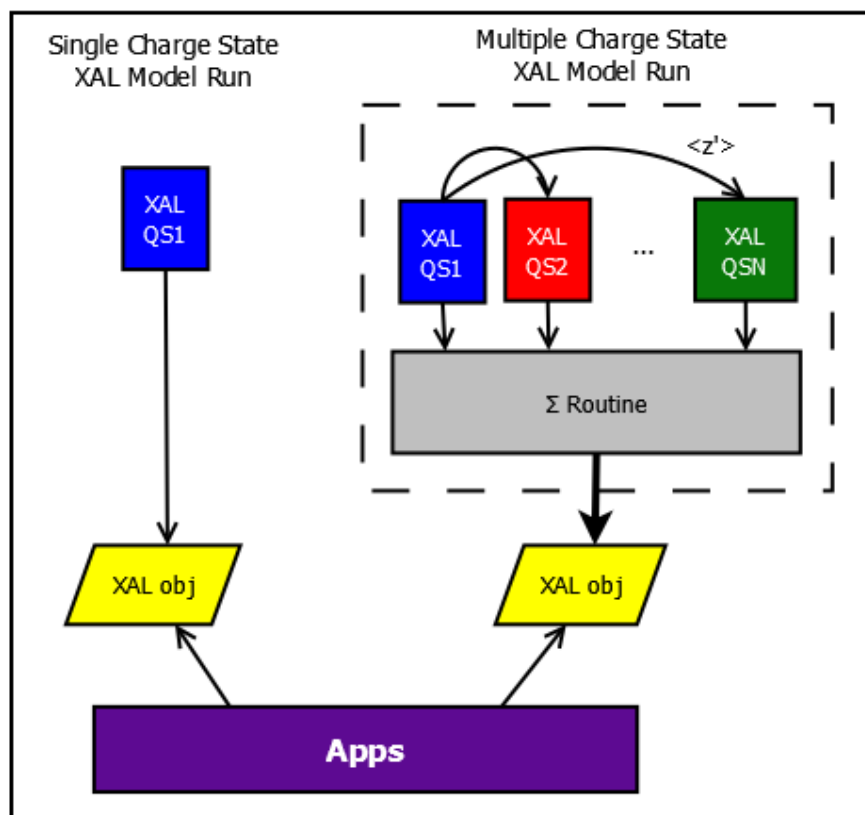


Figure 3.24: XAL Schema for adding multiple charge state run capabilities.

Chapter 4

Quarter-Wave Resonator Steering

The focus of this chapter is on the behavior of the low- β accelerating cavities utilized at ReA, Quarter-Wave Resonators (QWRs). Understanding and characterizing the performance of these cavity types is crucial for the most efficient operation of not only ReA, but other future linacs that will use QWRs, such as FRIB.

One attribute specific to QWRs is the unique asymmetric geometry with respect to the beampipe, unlike other accelerating cavity types which are symmetric with respect to the beampipe. This asymmetry, typically in the vertical direction, leads to a deflection of the beam in the direction of the asymmetry. Calculations of the predicted QWR steering effect as derived from electromagnetic field profiles have been performed, but they had not been experimentally verified. In order to accomplish this, calculations for the ReA $\beta = 0.041$ cavity type have been compared with the results from measurements performed at ReA characterizing this effect.

The analytic steering predictions are presented in Section 4.1, along with the calculation for the ReA $\beta = 0.041$ and $\beta = 0.085$ QWR steering prediction in Section 4.1.3. A detailed description of the experiments performed at ReA with the $\beta = 0.041$ QWR cavity type is presented in Section 4.2, concluding with analysis and results from these experiments.

4.1 Steering Predictions

An analytic approach to the behavior of QWR cavities with respect to vertical steering has been derived by Facco and Zvyagintsev [55]. They arrive at a formula for the vertical steering of the beam which consists of three terms.

The first two terms arise from the asymmetry of the QWR structure, depending on the x -component of the magnetic field, and the y -component of the electric field. The third term, proportional to the offset of the beam from the central cavity axis, arises from RF defocusing, as introduced in Section 3.3.3.

Before considering this formula, the choice of using QWR type accelerating cavities is briefly discussed in Section 4.1.1 to motivate the reasoning behind using an element that is asymmetric to the beampipe, and therefore produces steering of the beam due to this asymmetry. Following is a review of the derivation of the vertical steering formula, presented in detail in Section 4.1.2. A final discussion of the relevant ReA calculations is presented in Section 4.1.3.

4.1.1 QWR Choice

Quarter-Wave Resonators are the accelerating cavity of choice for low- β beams in linacs such as ReA and FRIB. Low- β beams require longer RF wavelengths, and therefore lower frequencies, due to the required spacing between the accelerating gaps.

For optimal acceleration, the beam travels the distance between the gaps in the time that it takes the RF phase to switch by $\Delta\phi = \pi$ (π -mode) [47]. This leads to $\Delta\phi = \omega\Delta t = \pi$, where $\omega = 2\pi c/\lambda$, and $\Delta t = l/v = l/(c\beta)$. Solving for l , the spacing between the RF gaps, results in $l = \beta\lambda/2$.

To be mechanically stable with a reasonable gap-to-gap distance, l , the RF wavelength, λ , must be increased when β is low. This results in a lower resonant RF frequency, f , recalling that $\lambda = c/f$. In order to avoid impractically large structures when requiring cavities to operate at lower frequencies, QWR type cavities are used, as its length is $\sim\lambda/4$, as its name suggests, as opposed to the HWR length of $\sim\lambda/2$, as seen in Figure 4.1.

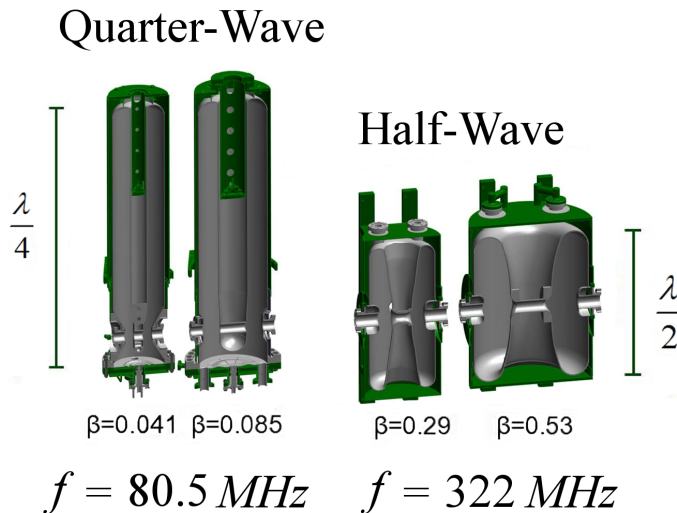


Figure 4.1: FRIB Quarter-Waver Resonator (QWR) and Half-Wave Resonator (HWR) cavity types shown with optimal β and operational frequencies. The FRIB HWRs are designed for four times the frequency of the QWRs, resulting in their length being about half as long.

The geometry of the QWR cavity type allows a standing wave of length $\lambda/4$ to be excited at its resonant frequency. The shape that the resonator must take to achieve this standing wave results in its asymmetry with respect to the beam pipe.

The QWR cavity can be thought of as a coaxial cable that is shorted at one end — the magnetic field circulates at the closed end, while the electric field that accelerates the beam is located at the open end. This can be seen in Figure 4.2.

Any asymmetries, whether part of the design or produced during the manufacturing process, of elements with respect to the beam pipe can introduce aberrations to the beam. These asymmetries introduce fields on-axis that can deflect the beam off its desired trajectory.

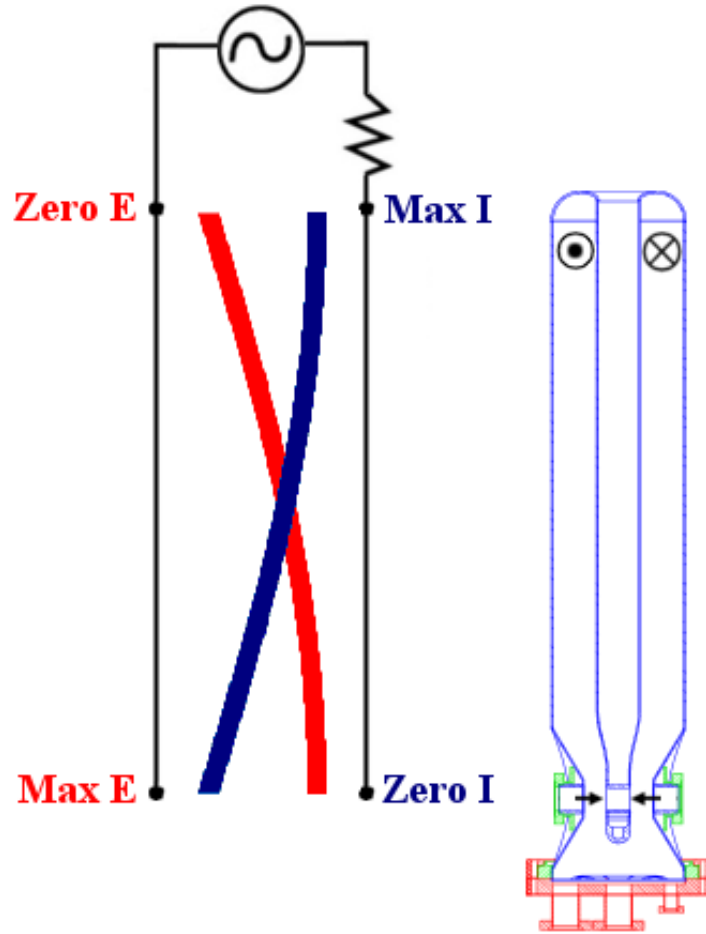


Figure 4.2: Coaxial Cable Analogy: the beam is accelerated at the open end of the “circuit” where the electric field is maximized, while the magnetic field circulates at the closed end.

This becomes an issue with QWR cavities because of the inherent asymmetry of their design.

There are two direct correction methods to address this issue, either through the design of the beam port shaping to counteract the field asymmetry, or through the displacement of the QWR axis during installation to offset the majority of the effect [56]. These methods may eliminate most of the steering introduced by the asymmetry, however this can be more complicated mechanically and lead to higher costs in production. Avoiding these complications with the simplified “straight” beam port design geometries and installing the QWRs on-axis is often the most realistic and feasible approach. Therefore it is important in

this case to study and understand the degree of the steering in order to be able to analyze this effect through modeling and aim to mitigate it through the use of corrective steerers.

4.1.2 Vertical Steering

The vertical steering induced through a QWR can be derived as a function of the average accelerating field, the cavity phase, the beam velocity and the vertical offset of the cavity. The fields that contribute to the change in vertical momentum that are present in a QWR cavity are E_y and B_x , from the Lorentz force, as seen in Equation 4.1.

$$\Delta p_y = q \int (E_y(z, t) + \beta c B_x(z, t)) dt \quad (4.1)$$

The assumption is made that the values of the fields on axis ($x = y = 0$) may be used to calculate the beam steering effect for beams slightly off-axis, a valid approximation when the beam is near the central cavity axis, as is the case for particles entering along the design trajectory. Recall that these field profiles have been shown in Figure 3.10.

By using the paraxial approximation ($p_z \approx p$), the vertical steering effect is then given by $\Delta y' = \frac{\Delta p_y}{p}$, where Δp_y is the change in transverse momentum imparted by the cavity, and p is the longitudinal momentum. By plugging in $p = \beta \gamma A m_0 c$ and performing the integrals while assuming only small changes in β through the accelerating gap, such that $z \approx z_0 + \beta c t$, we arrive at Equation 4.2.

$$\Delta y'(\beta) = \frac{q e E_a L \sin \phi}{A m_0 c^2 T_{Ez}(\beta_0)} \times \{D_{Bx}(\beta) + D_{Ey}(\beta)\} \quad (4.2)$$

Recall that T_{Ez} has been defined as the transit time factor in Equation 3.37. The first

term in Equation 4.2 arises from the fact that there is a nonzero x -component of the magnetic field. The formula for D_{Bx} is given in Equation 4.3.

$$D_{Bx}(\beta) = \frac{G_{Bx}}{\beta\gamma} T_g(\beta, g_{Bx}) \sin\left(\frac{\pi d_{Bx}}{\beta\lambda}\right) \quad (4.3)$$

The second term in Equation 4.2 is due to the y -component of the electric field. The formula for D_{Ey} is given in Equation 4.4.

$$D_{Ey}(\beta) = \frac{G_{Ey}}{\beta^2\gamma} T_g(\beta, g_{Ey}) \cos\left(\frac{\pi d_{Ey}}{\beta\lambda}\right) \quad (4.4)$$

This vertical electric field is much weaker than the transverse magnetic field, as mentioned earlier, which results in the strength of this term being an order of magnitude smaller. We also note this term is also inversely proportional to the square of β , so for low β beams, such as the case where we are interested, this term does become stronger. The geometrical constants, G_{Bx} and G_{Ey} , are given by Equations 4.5.

$$G_{Bx} = \frac{c \int_0^{L/2} B_x(z) dz}{\int_0^{L/2} E_z(z) dz} \quad G_{Ey} = \frac{\int_0^{L/2} E_y(z) dz}{\int_0^{L/2} E_z(z) dz} \quad (4.5)$$

$T_g(\beta, g)$ has been defined in Equation 3.37. The gap-to-gap distances, d_{Ez} , d_{Ey} , and d_{Bx} , are given by Equation 3.38. The gap lengths, g_{Ez} , g_{Ey} , and g_{Bx} , are given by Equation 3.39.

These terms arise from fields due to the asymmetry of the cavity. These QWR on-axis fields were presented in Section 3.3.1. It is the result of these two terms that there is a net vertical steering for QWR cavities, even when the beam is centered in the aperture of the cavity. Once the beam is not centered in the cavity, however, these are not the only factors behind beam steering. There is also a contribution due to the offset of the beam entering into

the cavity. This contribution is present due to an effect called RF defocusing, as previously presented in Section 3.3.3.

This radial transverse defocusing effect depends on $\vec{r} = r\hat{r} = x\hat{x} + y\hat{y}$. Restricting our discussion to beam steering in the vertical \hat{y} -direction, the RF defocusing term depends simply on y , the vertical deviation of the beam from the beam axis. When added to the first two terms introduced due to the QWR cavity asymmetry, the full equation for the change in vertical angle as a function of β as presented in [55] is given in Equation 4.6.

$$\Delta y'(\beta) = \frac{qeE_a L \sin \phi}{Am_0 c^2 T_{Ez}(\beta_0)} \times \{D_{Bx}(\beta) + D_{Ey}(\beta) + D_{rf}(\beta, y)\} \quad (4.6)$$

The term due to RF defocusing is given in Equation 4.7.

$$D_{rf}(\beta, y) = -\frac{\omega}{2\beta^3 \gamma^3 c} T_g(\beta, g_{Ez}) \sin\left(\frac{\pi d_{Ez}}{\beta \lambda}\right) y \quad (4.7)$$

Note again that it depends linearly with y , and has a negative sign, due to the fact that E_r and E_z have opposite signs, as stated in Section 3.3.3. This term is typically larger than D_{Bx} and D_{Ey} at low velocities, but decreases at higher velocities. This can be seen in Figure 4.3 where each D -factor term is plotted across a typical β range calculated at ReA $\beta = 0.041$ cavity accelerating parameters of $E_a = 16$ MV/m and $\phi = -90^\circ$. The sum of the three terms is also plotted.

With all three terms introduced, there are some observations to be made. The magnitude of the terms has been presented, and it is important to recognize that when measuring the effect in an experiment, all terms will be present at once. Another important note is that the three terms that contribute to Equation 4.6 do not all have the same sign. The last term has

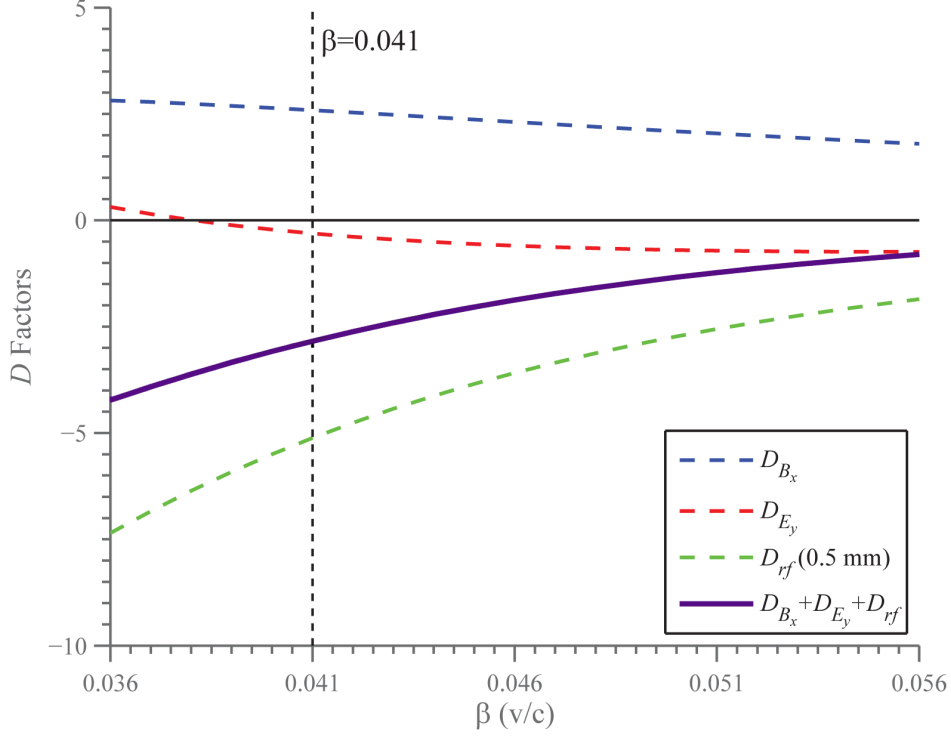


Figure 4.3: The calculated ReA $\beta = 0.041$ cavity D -factors from Equation 4.6, D_{B_x} , D_{E_y} , and D_{rf} , with $E_a = 16 \text{ MV/m}$ and $\phi = -90^\circ$ along with the sum of the three terms.

a minus sign, which indicates that there is a “sweet-spot” where the contribution from each term will cancel each other out. This is predicted to be at a slightly positive vertical offset. This “sweet-spot” as predicted by theory may allow for the determination of the alignment of the cavity center with respect to the diagnostics center with a beam-based measurement.

4.1.3 ReA Calculation

A calculation of Equation 4.6 has been performed and the results are shown here. As mentioned previously, the 3D fields from the ReA cavities are calculated with CST Microwave Studio. The on-axis fields are used to calculate the values for the vertical steering result. The $\beta = 0.041$ cavity’s on-axis fields used for the ReA calculation are shown in Figure 3.10. The FRIB cavity fields are similar, and result in comparable, but not identical, calculations. Here

we will focus solely on the calculations for the ReA cavities, to be compared with experiments.

A sample calculation of the change in vertical deflection from Equation 4.6 is presented in Figure 4.4. Typical accelerating parameters of $E_a = 16 \text{ MV/m}$ and $\phi = -20^\circ$ have been used for this calculation. The two graphs depict the result for the ReA $\beta = 0.041$ QWR fields, along with the calculations performed for the ReA $\beta = 0.085$ QWR fields. Each graph includes a vertical dashed line at the optimal beta of the cavity. The central theory line, in blue, plots the $dy = 0 \text{ mm}$ case, while the other lines above and below show the result of a $\pm 1 \text{ mm}$ vertical beam offset from the ideal trajectory through the center of the cavity.

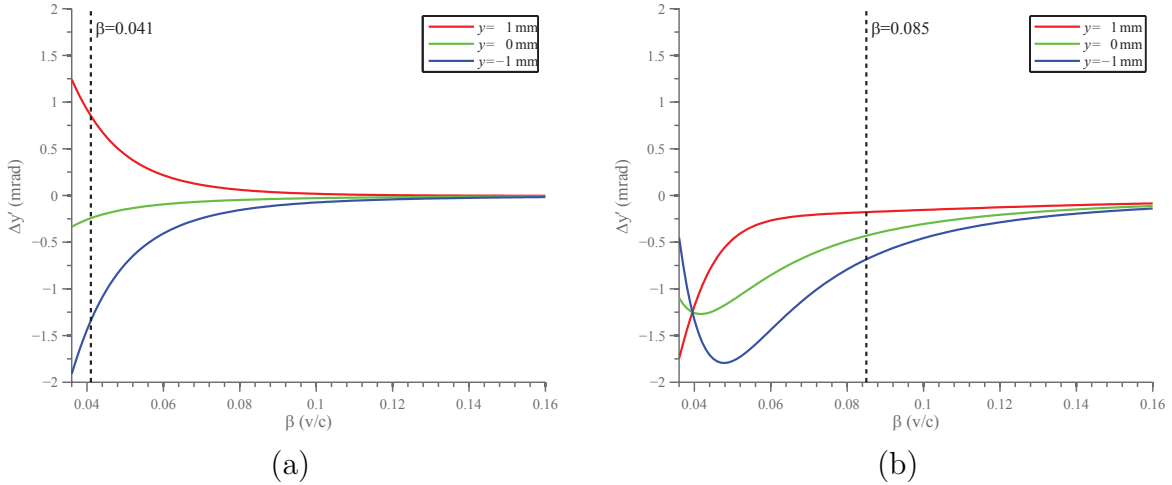


Figure 4.4: Calculation of $\Delta y'$ vs. β for the ReA (a) $\beta = 0.041$ and (b) $\beta = 0.085$ cavity types, plotted for centered and $\pm 1 \text{ mm}$ vertical offset scenarios. A typical accelerating cavity setting is used: $\phi = -20^\circ$ and $E_a = 16 \text{ MV/m}$. The beam species is H_2 with $q/A = 0.5$. The x -range for each plot is from $\beta = 0.036$, corresponding to the RFQ energy of 0.6 MeV/u , to $\beta = 0.16$, corresponding to the highest beam energy for H_2 at ReA, 12 MeV/u .

This calculation was performed at $E_a = 16 \text{ MV/m}$; however, many of the ReA cavities can be operated up to fields of $E_a = \sim 30 \text{ MV/m}$. This will almost double the $\Delta y'$ as shown in Figure 4.4. Another factor to consider is that the steering will increase when the cavities are operated in rebunching mode at $\phi = -90^\circ$, instead of accelerating at $\phi = -20^\circ$, but this is typically done at much lower fields which then reduces the effect. Each different case will

change the overall magnitude, but the trends of the curves remain the same. Keeping this in mind, we can use the case shown in Figure 4.4 to look more into this steering effect as it relates to the ReA QWR cavities specifically.

It is important to note that the regions in which the $\beta = 0.041$ and $\beta = 0.085$ cavities operate differ, and the calculated deflections are much larger in the lower β regions where $\beta = 0.041$ cavities are used. This is due to the effect being inversely proportional to β , with slower beams being deflected more. This is important to note, because it means that the effect is greatest with the lower velocity, lightest beams.

In these plots, the same offset produces a much larger effect at the $\beta = 0.041$ cavity's optimal β than it does at the $\beta = 0.085$ cavity's optimal β . From the $\beta = 0.041$ plot in Figure 4.4, it is noted that at $\beta = 0.041$, the difference between the ± 1 mm cases is ~ 2 mrad, while the same difference at $\beta = 0.085$ in the $\beta = 0.041$ plot in Figure 4.4 only produces a difference of ~ 0.5 mrad. This indicates that the $\beta = 0.041$ cavities are much more sensitive to an offset from the beam line center, which we also hope to measure.

Plotted in Figure 4.5a is the predicted change in vertical beam angle normalized by the cavity field for a ReA $\beta = 0.041$ cavity operating at -90° phase vs. β across a range of energies available at ReA.

From the plot in Figure 4.5a, the simple observation can be made that a negative kick is generally expected from the cavity for negative offsets. Similarly, a positive kick from the cavity is expected for positive offsets. Recall that the central theory line, plotted for $dy = 0$ mm, however, will not equal zero, as confirmed in the graph. From the trend of the curves, note that lower beam energies, corresponding to lower β , result in a larger net displacement. Again, comparing the plots it is also clear that larger offsets will result in larger displacement.

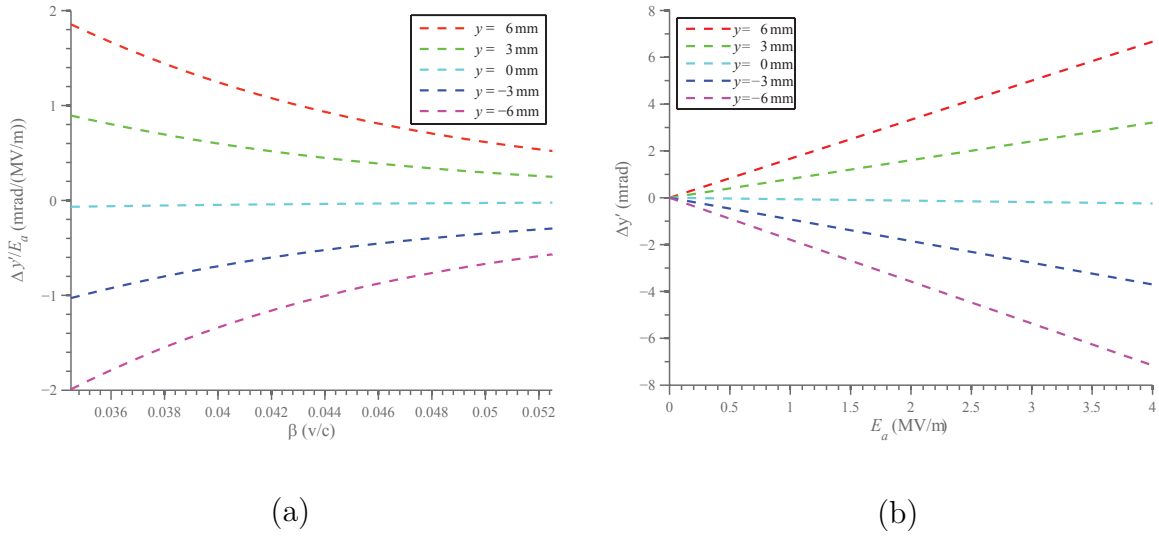


Figure 4.5: Left (a): Plot of ReA $\beta = 0.041$ calculation $\Delta y'$ vs. β for offsets $dy = -6, -3, 0, 3,$ and 6 mm. Right (b): $\Delta y'$ vs. cavity amplitude E_a for offsets $dy = -6, -3, 0, 3,$ and 6 mm for beam energy $E_k = 0.6$ MeV/u, corresponding to $\beta = 0.036$.

For the calculations in Figure 4.5a, the vertical kick has been normalized by E_a . Varying the cavity amplitude for a fixed energy instead results in the trends shown in Figure 4.5b. For a fixed energy of 0.6 MeV/u, corresponding to $\beta = 0.036$, Figure 4.5b plots $\Delta y'$ vs. E_a . Looking at the $dy = \pm 3$ mm plots at $E_a = 4$ MV/m, the expected $\Delta y'$ is 3 mrad and -4 mrad respectively. This demonstrates that the deflection is not symmetric. Adding a slightly positive offset dy to the beam entering the cavity can minimize the deflection of the beam due to the QWR steering. This is the “sweet-spot” indicated in section 4.1.2. This theoretical offset to eliminate steering in the QWR cavities at ReA for 0.6 MeV/u beams is ~ 0.2 mm.

4.2 Experiment

The vertical steering can be studied with a carefully designed experiment at ReA, which exclusively uses QWRs in its linac. The layout of ReA during this experiment is depicted in Figure 4.6. The deflection can be maximized by using a low mass beam at low energy and

operating one of ReA's relatively low beta cavities in rebunching mode. The deflection can be scaled down by either increasing the beam mass, increasing the beam energy, lowering the cavity's amplitude or operating the cavity at an accelerating phase instead of rebunching, where theory predicts the amplitude of the steering is greatest. For stability, the test cavity is left at a fixed phase of -90° . As energy is one of the variables under investigation in this experiment, it is also beneficial to measure the deflection at the -90° phase setting where the energy of the beam is unchanged.

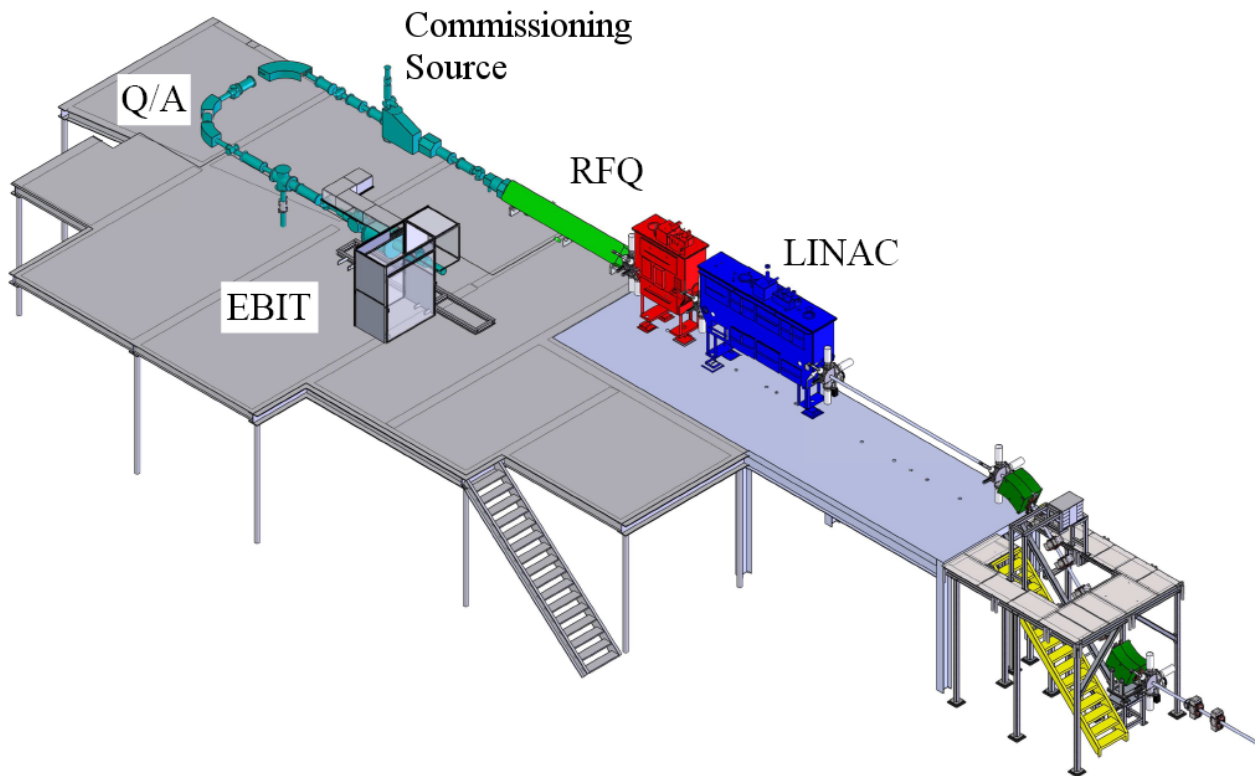


Figure 4.6: ReA Layout from 2013, including EBIT charge breeder, Q/A section, commissioning source, room temperature RFQ and superconducting linac including two cryomodules containing $\beta = 0.041$ accelerating cavities. Note the drift tube after the second cryomodule is the location for the third cryomodule containing $\beta = 0.085$ accelerating cavities, to be installed.

The cavity's amplitude is varied to compare its response with the linear relationship as predicted by Equation 4.6. The offset of the beam going into the cavity is also varied to see

the dependence of the third term in Equation 4.6. These results are then compared with the calculations shown in Figure 4.5b. Lastly, this measurement is performed at multiple beam energies in order to compare the experimental measurement with the theoretical predictions as seen in Figure 4.5a.

4.2.1 Procedure

The procedure for this measurement begins with tuning the linac to the desired energy with a parallel beam through the long drift tube following the linac. The four measurement energies are $E_k = 0.60 \text{ MeV/u}$, 0.85 MeV/u , 1.08 MeV/u , and 1.24 MeV/u . The last cavity is off during this phase. The parallel beam is achieved using the two horizontal and vertical steerers located before the last cavity in the second cryomodule, labeled in Figure 4.7 as the test cavity. Each solenoid in the linac is equipped with horizontal and vertical steerers. The two cavities before the test cavity remain off during each measurement point, resulting in a drift space between the two solenoids utilized to establish a parallel beam.

The beam diagnostic locations at which the beam profiles are measured are also labeled in Figure 4.7. These two beam diagnostic locations will be referred to as L092 and L110 respectively. The energy is measured using the dipole-slit procedure: a dipole magnet is located directly after L110 (not shown). Adjusting the calibrated dipole field to achieve a beam centered at the collimator slits determines the energy of the beam. The centroid at the two locations after the linac is measured with the 45° slit scanners to establish the baseline beam trajectory.

The test cavity is then turned on in rebunching mode and the slit scanners measure the beam centroid position at the two downstream locations. The cavity amplitude is then changed multiple times, measuring the centroid positions each time. After these measurements,

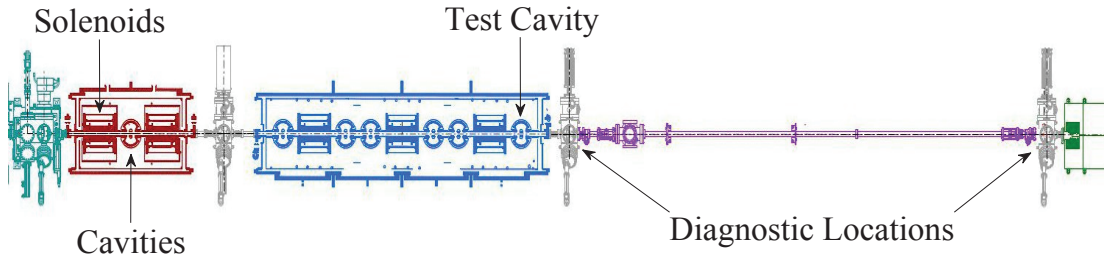


Figure 4.7: Schematic of ReA Linac as commissioned in 2013, before the installation of the third cryomodule. Square elements represent superconducting solenoids, while circular elements represent quarter-wave resonators. The drift space between the diagnostics after the second cryomodule is ~ 5.2 m.

the cavity is turned off and a new parallel beam is achieved with a vertical offset. The same procedure is repeated for multiple different offsets. The method for establishing a vertical offset using the two correctors before the test cavity is described in following section.

4.2.1.1 Vertical Offsets

Figure 4.8 is a compilation of the data taken in two different measurements, at 1.3 MeV/u and 1.24 MeV/u beam energy. The plot shows the extrapolated position of the beam, y_m from measuring the position at L092, y_1 and the angle y' from measuring the position at L110, y_2 . The different offsets were produced by changing the corrector settings in front of the test cavity can, as seen with the variation of the points in the y -direction.

The procedure during the first measurement in May was to steer the beam up by introducing small vertical steps in the slits, and tuning on the beam transmission. This step-by-step method resulted in a large shift in the x -direction, since the horizontal slit (measuring the vertical position) does not constrain the beam in the x -direction. It is preferable for this experiment to isolate the vertical motion of the beam.

A new method was therefore devised to determine the beam's response from each individual

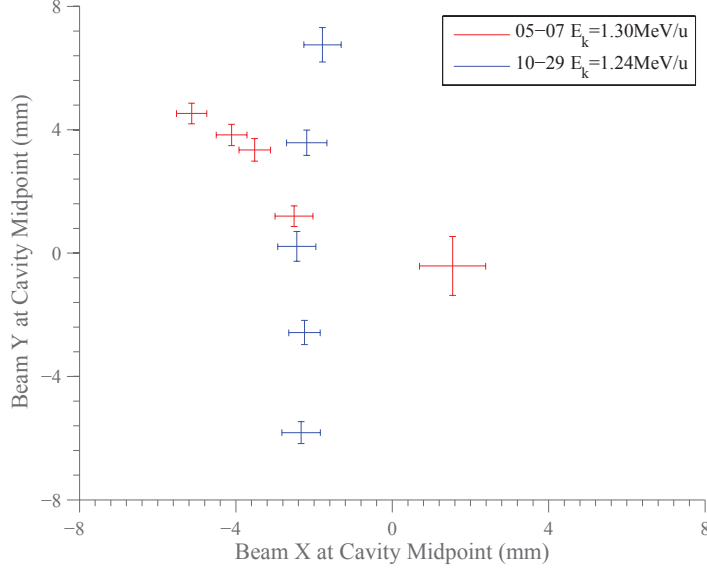


Figure 4.8: Beam position at cavity midpoint as projected from measurements at two downstream locations. Error bars are the RMS beam size. Note the improvement of the vertical separation and consistency of horizontal position achieved with the 10-29 data set which utilized the response matrix measurement technique.

corrector and use the resulting response matrix to achieve a purely vertical displacement of the beam. The difference between the beam's position at the two downstream locations, $\vec{\Delta x}$ given in Equation 4.8, was measured as a function of the change in the four individual corrector settings, $\vec{\Delta I}$.

$$\vec{\Delta x} = \begin{pmatrix} \Delta x_1 \\ \Delta y_1 \\ \Delta x_2 \\ \Delta y_2 \end{pmatrix} \quad \vec{\Delta I} = \begin{pmatrix} \Delta I_{H1} \\ \Delta I_{V1} \\ \Delta I_{H2} \\ \Delta I_{V2} \end{pmatrix} \quad (4.8)$$

By changing each corrector individually and recording the response of the beam, the matrix

M in Equation 4.9 is mapped out element by element.

$$\begin{aligned}\vec{\Delta x} &= M \vec{\Delta I} \\ \vec{\Delta I} &= M^{-1} \vec{\Delta x}\end{aligned}\tag{4.9}$$

Inverting M and plugging in the desired shift in beam position, given in Equation 4.10, established a ratio of the corrector settings to use in order to offset the beam vertically by a desired amount.

$$\vec{\Delta x} = \begin{pmatrix} 0 \\ \Delta y \\ 0 \\ \Delta y \end{pmatrix}\tag{4.10}$$

This procedure was more robust than the previous method, and successfully prevented the beam from moving in the x -direction, as can be seen in the October data in Figure 4.8. With this response matrix approach a large vertical shift of the beam with very little movement in the horizontal direction can be achieved, as desired.

4.2.1.2 Profile Measurement

Beam profile scans at both diagnostic locations discussed previously, L092 and L110, determine the centroid and RMS beam size. These measurements are performed with 45° slit scanners. The 45° slit scanner plate is shown in top left of Figure 4.9. This plate intercepts the beam at a 45° angle, allowing the horizontal slit to measure the vertical beam profile, and the vertical slit to measure the horizontal beam profile. A 5 mm collimation hole is also drilled in the end of the plate for beam tuning. Sample scans are shown in Figure 4.10.

The scan is performed by fully inserting the drive (drive position = -100 mm) and moving

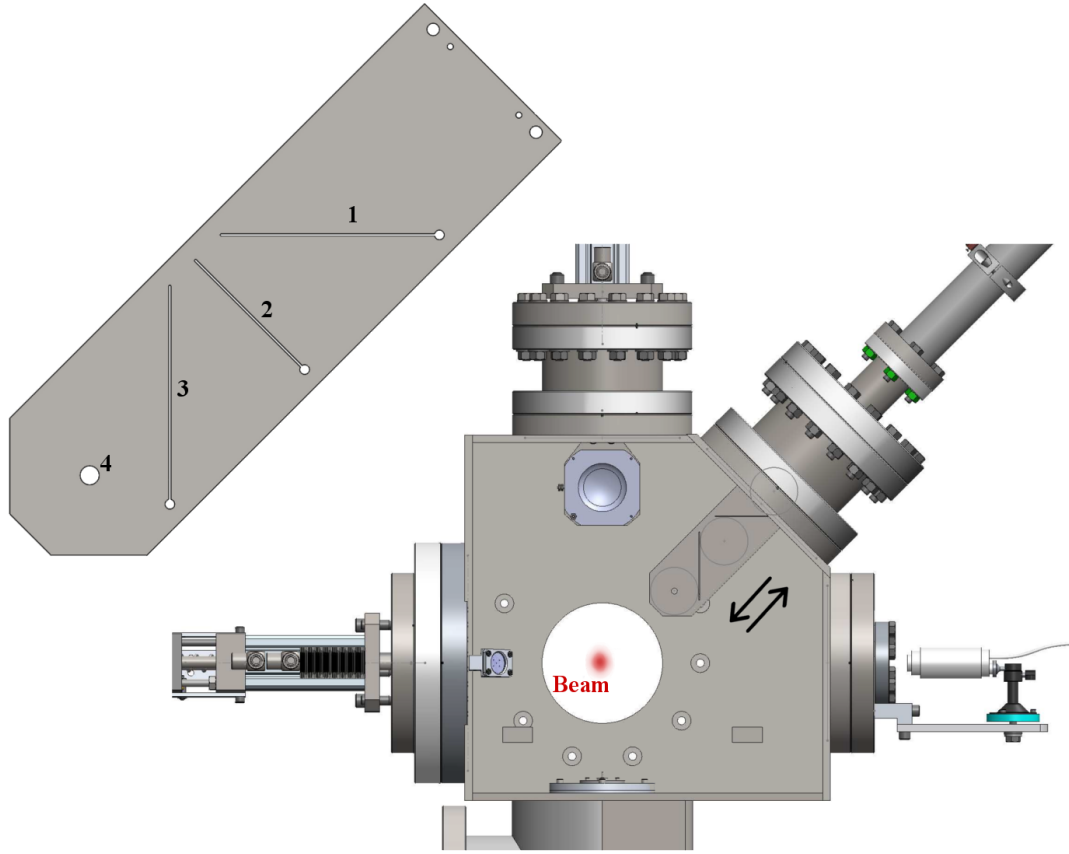


Figure 4.9: 45° Beam Profile Diagnostic setup. In the top left, the plate is shown with three slits and one aperture in the order that they intercept the beam during the profile scans: (1) the horizontal slit measuring the vertical beam profile, (2) the 45° slit for a measure of the coupling between the x and y planes, (3) the vertical slit measuring the horizontal beam profile, and (4) the 5 mm aperture for beam tuning.

the drive in 1 mm steps until it no longer intercepts the beam (drive position=40 mm). With this direction of running the scan, the peak on the far left of the plot corresponds to the vertical profile of the beam. The next peak corresponds to the horizontal profile of the beam, while the peak centered at drive position = 0 mm corresponds to the 5 mm hole. The drive at L092 has an additional central slit perpendicular to the motion of the drive to measure the 45° profile of the beam, which accounts for the central peak in the L092 drive scan that is absent from the L110 scan.

In Figures 4.10a and 4.10b, appropriate regions have been used for fitting a Gaussian curve

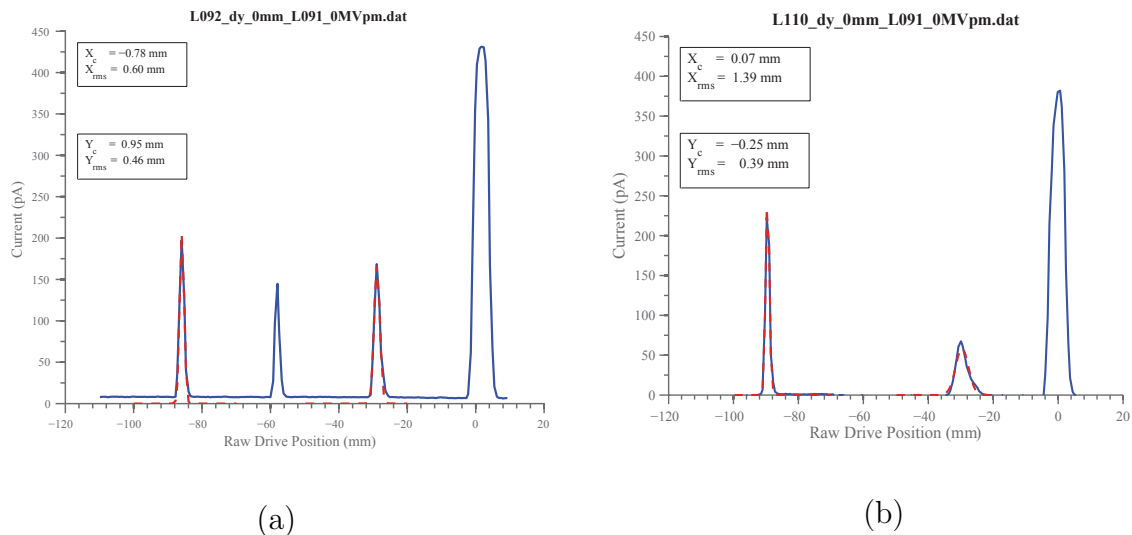


Figure 4.10: Plots of beam current vs. slit position for raw data from 45° slit scan taken at (a) L092 and (b) L110, and the Gaussian fit results for beam position and RMS beam size. Note that the 45° plate at L110 does not have the 45° slit, which accounts for the missing peak in (b).

to each peak. A low threshold level is subtracted from the raw data before the fitting analysis is performed to reduce background noise fluctuations. The resulting Gaussian curves fit to each peak is shown in the dashed red lines. The fit parameters from the Gaussian curve also give the centroid and RMS beam size for the horizontal and vertical profiles. Equation 4.11 gives the equation for a Gaussian function.

$$y = Ae^{-\frac{(x-\mu)^2}{2\sigma^2}} \quad (4.11)$$

The raw drive position, as plotted in Figure 4.10, is along the 45° axis, so a simple transformation has to be made to extract the absolute x and y positions and beam sizes. The raw position, given by μ in Equation 4.11, is centered and then the relative distance to the slit position is either added or subtracted to get the position of the slit measuring either y or x , and then divided by $\sqrt{2}$ to get the distance along the perpendicular axis instead of along the

45° angle. Similarly, the RMS size determined by the Gaussian fit, given by σ in Equation 4.11, must be divided by $\sqrt{2}$. These transformations are given in Equations 4.12 and 4.13, with a schematic representation of the distances d_{ref} and d_{offset} shown in Figure 4.11.

$$x_c, y_c = \frac{\mu_{x,y} - d_{\text{offset}} \mp d_{\text{ref}}}{\sqrt{2}} \quad (4.12)$$

$$x_{\text{RMS}}, y_{\text{RMS}} = \frac{\sigma_{x,y}}{\sqrt{2}} \quad (4.13)$$

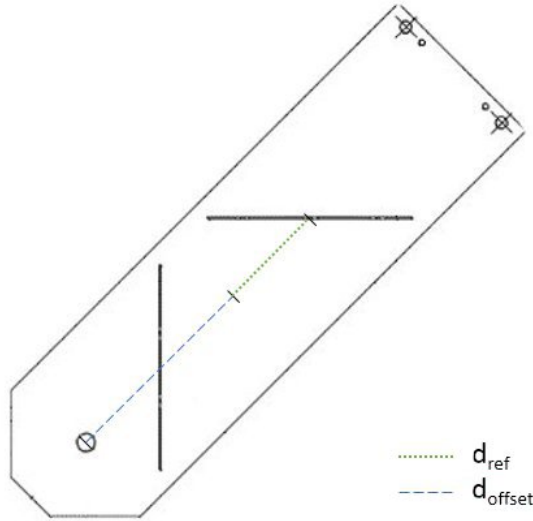


Figure 4.11: 45° Beam Profile Diagnostic Plate shown with distances from Equation 4.12, d_{ref} and d_{offset} , labeled.

In the scan in Figure 4.10a, the centroid position of the beam at L092 is about $(-0.8 \text{ mm}, 1.0 \text{ mm})$ with RMS size $(0.6 \text{ mm}, 0.5 \text{ mm})$. After the long drift space, the beam profile is measured again at L110, shown in the scan in Figure 4.10b. The centroid position of the beam has changed to about $(0.1 \text{ mm}, -0.3 \text{ mm})$ with RMS size of about $(1.4 \text{ mm}, 0.4 \text{ mm})$. The change in x -position of $\sim 0.9 \text{ mm}$ along a $\sim 5.2 \text{ m}$ drift corresponds to $x' \approx 0.17 \text{ mrad}$. In y the change in position of $\sim -1.3 \text{ mm}$ corresponds to $y' \approx -0.25 \text{ mrad}$.

All measurement data sets include these initial measurements taken with the test cavity turned off. During the analysis, all measurement points will subtract these small initial angles in order to measure changes in angle, instead of absolute angle. Multiple calibration points are also measured through the run time to ensure the stability of these initial conditions.

4.2.2 Beam Axis Definition

The measurement of the beam centroid position at both diagnostic locations enables the computation of the angle of the beam from the change in position between them, as they are separated by a drift space. This is schematically represented in Figure 4.12. The difference of the measurements at the first and second diagnostics determine the beam's deflection,

$$y' = \frac{y_2 - y_1}{d}.$$

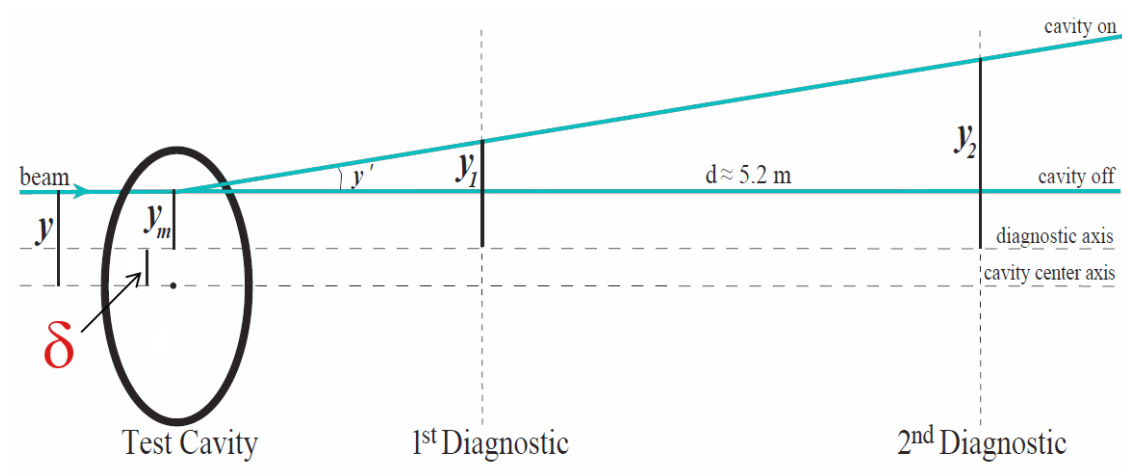


Figure 4.12: Schematic diagram of relevant measurement quantities depicting the difference between the diagnostic axis and the cavity center axis.

The beam enters the cavity at a certain unknown vertical offset, with the cavity off. The parallel beam is measured at the two diagnostic locations, but as noted in the previous section, the beam may have an initial angle measured with the cavity off (not shown). This is subtracted off from each measurement with the cavity turned on in order to look at relative

changes, $\Delta y'$. Figure 4.12 shows a simplified perspective where the incoming angle is zero.

Each beam measurement, y_1 and y_2 , are measured with respect to the diagnostic axis, with zero defined as the center of the beampipe as defined by the alignment of the diagnostic elements. Once y' is calculated from y_1 and y_2 , the position of the beam at the center of the test cavity, y_m , can be extrapolated. This quantity is also calculated with respect to the diagnostic axis.

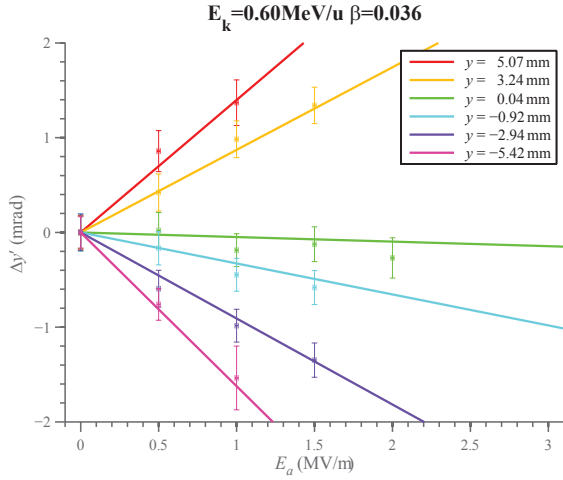
In Equation 4.6 for the QWR steering prediction, vertical offsets y are measured with respect to the cavity center. There exists a small unknown vertical displacement of the cavity center with respect to the diagnostic axis, δ . The relationship $y = y_m + \delta$, is true for all measurements, including across the different energy measurement, as δ is a constant. A chi-squared minimization of the entire data set calculates the optimal value of this quantity to be $\delta = 1.29$ mm.

This result is used to convert the raw measured values, y_m , to displacements with respect to the cavity center, y . In this way, all the data results shown in the following section along with the calculated predictions for a given offset y are consistent, defined with respect to the cavity center.

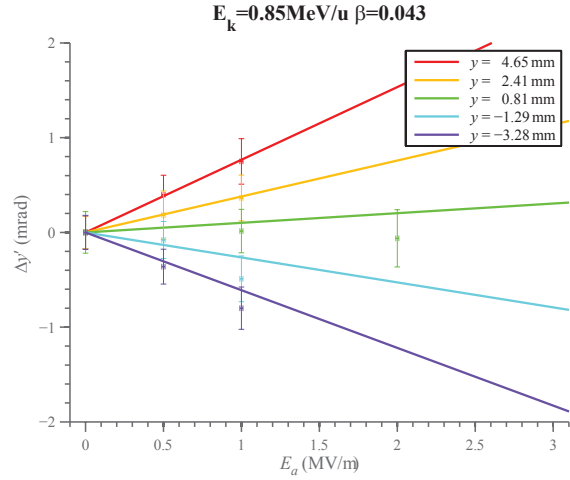
4.2.3 Results and Analysis

Figure 4.13 shows the results of the measurement data for beam energies 0.6 MeV/u, 0.85 MeV/u, 1.08 MeV/u, and 1.24 MeV/u. The plots show $\Delta y'$ vs. E_a (cavity amplitude setting) for various offsets, which were produced by changing the corrector settings in front of the cavity. With the cavity off, the beam positions at the two downstream locations are measured to give the baseline angle, which is then subtracted from each measurement point to get a change in angle, $\Delta y'$. This is why all the data sets overlap at the origin. This

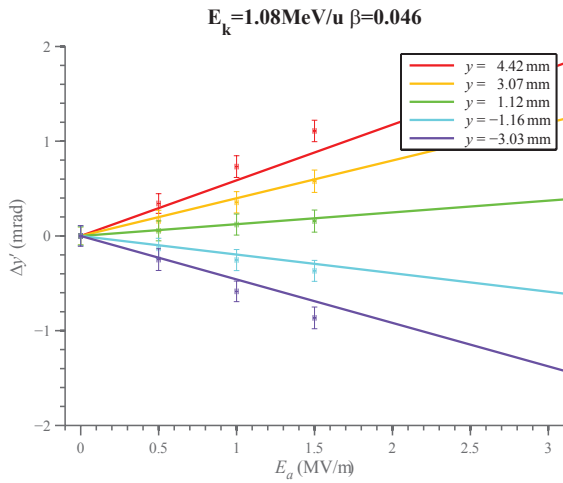
baseline angle is also used along with the position measured at the first measurement location to calculate the beam's position at the cavity center. These calculated values are given in the legends of the figures, as well as in the Δy column of Table 4.1, and are used to calculate the prediction for each data set.



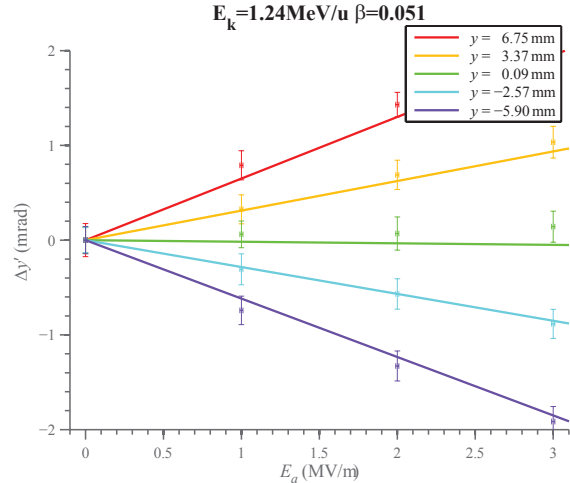
(a)



(b)



(c)



(d)

Figure 4.13: Plots of $\Delta y'$ vs. E_a for beam energies (a) $E_k = 0.6 \text{ MeV/u}$ ($\beta = 0.036$), (b) $E_k = 0.85 \text{ MeV/u}$ ($\beta = 0.043$), (c) $E_k = 1.08 \text{ MeV/u}$ ($\beta = 0.046$), and (d) $E_k = 1.24 \text{ MeV/u}$ ($\beta = 0.051$). Lines correspond to the predicted response calculated using cavity design data and experimental conditions.

The vertical error bars are determined from the statistical error inherent in fitting the beam's profile with a Gaussian. A larger RMS size of the beam at the measurement locations, or features of the profile such as a double peak, will increase the uncertainty to which the centroid of the beam is known at each location.

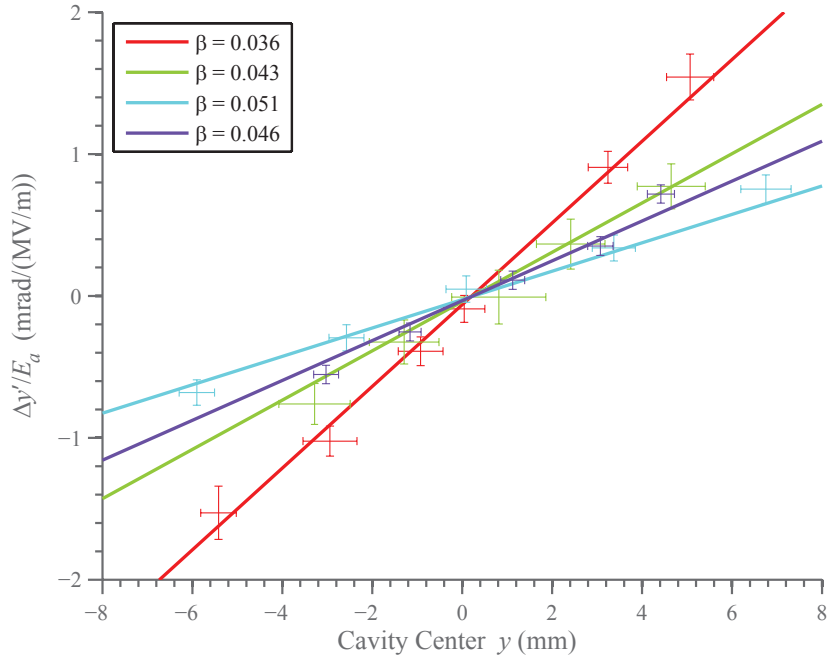
These errors in the beam's position are then added in quadrature and divided by the distance between the two measurement points in order to obtain the error on the angle. The horizontal errors are determined from the cavity's phase and amplitude stability measurements, yielding an RMS value of 0.005 MV/m.

When comparing similar vertical offsets from the cavity center between the plots, as expected, a larger kick was experienced by the lower energy beams. The cavity amplitude also could not be increased as much for the lower energy beams as it could for the higher energy beams, due to beam losses.

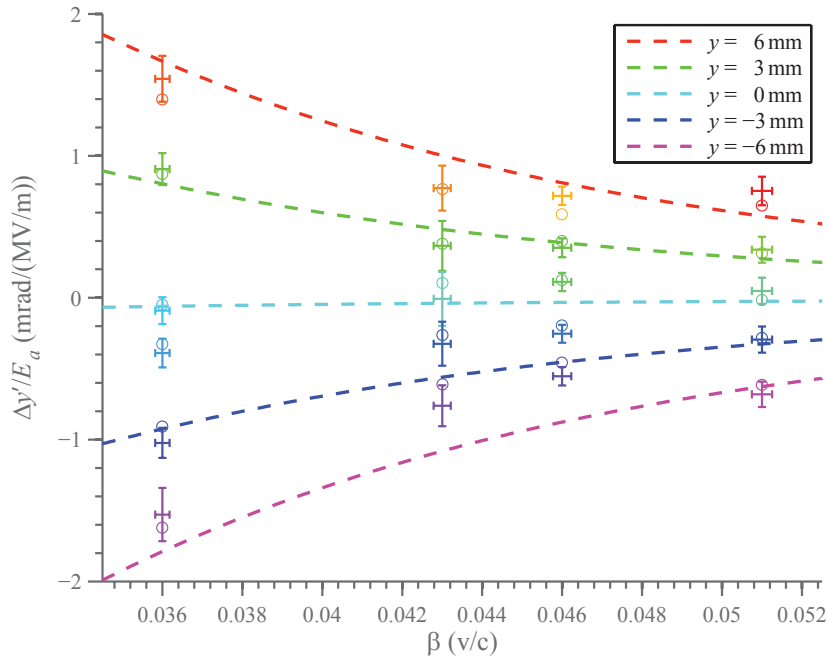
The setup at ReA limited the maximum possible measured $\Delta y'$ to ~ 2 mrad which corresponds to a ~ 10 mm shift over the 5.2 m drift between measurement points. Although the slit drives can measure a range of $\sim \pm 15$ mm, the beam may have already been displaced by up to ~ 5 mm from the center of the cavity, resulting in a maximum measurable displacement of ~ 10 mm in that same direction.

An important observation at this point that each data set is linear with varying the cavity amplitude, as we expect from Equation 4.6. It is also encouraging that the different offsets at the cavity fit fairly well within the error bars to its respective theoretical prediction.

The result from plotting $\Delta y'$ normalized by the amplitude of the test cavity setting for each point as a function of beam position at the midpoint of the test cavity is shown in Figure 4.14a. Note that the slopes of the relative energy measurements are ordered as expected, and agree reasonably well with theory.



(a)



(b)

Figure 4.14: Left (a): Plot of $\Delta y'/E_a$ vs. y at the midpoint of the test cavity, including each measurement data set. Note the agreement in the slopes for the different energies. Right (b): Plot of $\Delta y'/E_a$ vs. β including each measurement data set.

Another way to visualize the data is as a function of β , as shown in Figure 4.14b. Here the data points indicate an average of a measured data set (therefore plotting one point per offset). Open circles are the corresponding theory values for the zero-data measured offset at the cavity. Dashed lines are equally spaced theory lines for reference. Vertical error bars here are statistical, from the uncertainty in measurement of centroid from the Gaussian fitting of the beam profiles. The horizontal error bars on β correspond to a $\pm 1\%$ uncertainty on the energy measurement.

The full data set of values plotted in Figure 4.14b is available in Table 4.1. Note that numbers have been rounded to the hundredths place after all calculations.

Table 4.1: Summary of cavity steering data at $\beta = 0.036, 0.043, 0.046,$ and 0.051 .

β	Δy (mm)	$\Delta y'/E_a$ Meas. (mm/MV/m)	$\Delta y'/E_a$ Calc. (mm/MV/m)	Diff	Diff/Error
0.036	5.07	1.54 ± 0.16	1.40	0.14	0.89
	3.24	0.91 ± 0.11	0.87	0.03	0.31
	0.04	-0.09 ± 0.10	-0.05	-0.04	-0.45
	-0.92	-0.39 ± 0.10	-0.33	-0.06	-0.62
	-2.94	-1.02 ± 0.11	-0.91	-0.12	-1.09
	-5.42	-1.53 ± 0.19	-1.62	0.09	0.50
0.043	4.49	0.77 ± 0.16	0.74	0.03	0.20
	2.26	0.37 ± 0.18	0.35	0.01	0.07
	0.66	-0.01 ± 0.19	0.08	-0.08	-0.44
	-1.44	-0.33 ± 0.16	-0.29	-0.03	-0.22
	-3.44	-0.76 ± 0.14	-0.64	-0.13	-0.87
0.046	4.26	0.72 ± 0.06	0.57	0.15	2.39
	2.92	0.35 ± 0.07	0.38	-0.02	-0.37
	0.97	0.11 ± 0.06	0.10	0.01	0.12
	-1.31	-0.25 ± 0.06	-0.22	-0.04	-0.58
	-3.18	-0.55 ± 0.07	-0.48	-0.07	-1.13
0.051	6.60	0.75 ± 0.10	0.64	0.12	1.17
	3.22	0.34 ± 0.09	0.30	0.04	0.45
	-0.06	0.05 ± 0.09	-0.03	0.08	0.86
	-2.73	-0.30 ± 0.09	-0.30	0.00	0.04
	-6.05	-0.68 ± 0.09	-0.63	-0.05	-0.55

The four sections of this table, defined by the β column, correspond to the four measurement sets shown in Figure 4.13. Each row corresponds to a set of data taken with a distinct combination of corrector settings. The offset produced by these settings when $E_a = 0$ MV/m is given in the Δy column. Note that these are the same values used to create the lines shown in Figure 4.13.

The $\Delta y'/E_a$ Measurement column gives the average of all the data points for this given offset (after normalization by E_a). The stated error is the root of the sum of the squares of the errors for that measurement set normalized by the number of measurement points.

The $\Delta y'/E_a$ Calc. column gives the result of the calculation using the offset from the Δy column, while the Diff column gives the difference between the Measurement and Calculation columns. The Diff/Error column can be interpreted as a measure of how far off the data value is from the theory value with respect to the given error.

4.3 Conclusions and Outlook

A set of measurements has successfully been completed at ReA to study the vertical kick of the accelerating cavities, quarter-wave resonators (QWRs), in the linac. This study investigated the effect of the beam's vertical offset within the cavity, the cavity amplitude, and the beam's energy on the vertical steering. This is the first systematic measurement of QWR steering and its dependence on these various factors.

The basic procedure involves measuring the beam centroid at two downstream locations, from which the beam's vertical trajectory can be calculated. The beam's position at the center of the cavity is then used to calculate the predicted deflection of the beam, which can then be compared with the measurements. The prediction indicates that increasing the

cavity accelerating field, E_a , as well as increasing the offset of the beam from the central axis will result in a larger kick, $\Delta y'$.

In practice this has been known, but this is the first time that a systematic measurement of QWR beam steering has been performed. Having found a good agreement between the measured data and prediction, this effect can now confidently be included into future beam line modeling of ReA, and will be of relevance to other linacs using QWRs for low energy acceleration, such as the Facility for Rare Isotope Beams (FRIB).

These initial measurements have focused on the last $\beta = 0.041$ cavity of ReA, but in principle the established procedure could be performed with other cavities at ReA as well. In the future this method may prove to be useful in obtaining a beam-based measurement of the relative alignment of the cavities with respect to one another.

The only requirement for this method is that all elements after the test cavity be off in order to produce a drift space through which the beam's outgoing angle may be measured. This becomes more difficult with earlier cavities in the cryomodule, as the drift space to the first diagnostic increases.

It may be possible to use corrector fields after the test cavity to help transport the beam, as these weak fields induce a constant deflection on the beam, and the calculation is concerned with changes in deflection, rather than the absolute deflection. These corrector fields would have to be taken into account when calculating the beam's position in the cavity.

Overall, a very promising method now exists for determining the deflection of the beam from the QWR accelerating cavities, which can be used to inform future experiments and modeling efforts. This experimental verification of the steering predictions is an important step in fully understanding and characterizing the performance of the low- β accelerating cavities at ReA and FRIB.

Chapter 5

Conclusions

The various topics covered through this work are united under a central theme of modeling accelerator systems. From simulations of error propagation through an ideal design lattice, to experimental measurements of beam steering due to asymmetric accelerating cavities, the overall focus remains on accurately modeling accelerators in order to provide understanding, inform decisions, and ultimately improve performance.

5.1 Summary

There are many methods used for modeling accelerators. Multi-particle tracking and matrix transport are two that have been utilized throughout this work. The modeling of beam line elements including quadrupoles, solenoids, and coaxial accelerating cavities have been shown in detail, including considerations determined through the modeling studies.

The continuous development of online modeling of accelerator systems is enormously important for the future of accelerator physics. This crucial component is what will allow heavy ion accelerators of the future to be successful in running many different types of beam, including multiple charge states simultaneously, and minimize tuning times to increase efficiency.

This effort requires a method for modeling multiple charge states through envelope

calculations, which has been proposed and benchmarked with multi-particle tracking results.

A series of experiments has been conducted at ReA which measured the vertical quarter wave resonator steering. The results have been analyzed and compared with theory predictions.

The measured data from these experiments consists of changes in the vertical deflection, $\delta y'$ as a function of cavity accelerating field, E_a , for various energies. The cavity is set to -90° phase.

The raw data from the measurements initially does not correspond with the steering predictions, as shown in Figure 5.1a. This is due to the raw measurement data being taken with respect to an axis defined by the beam diagnostics, whereas the steering predictions are made with respect to the central cavity axis, as discussed in Section 4.2.2.

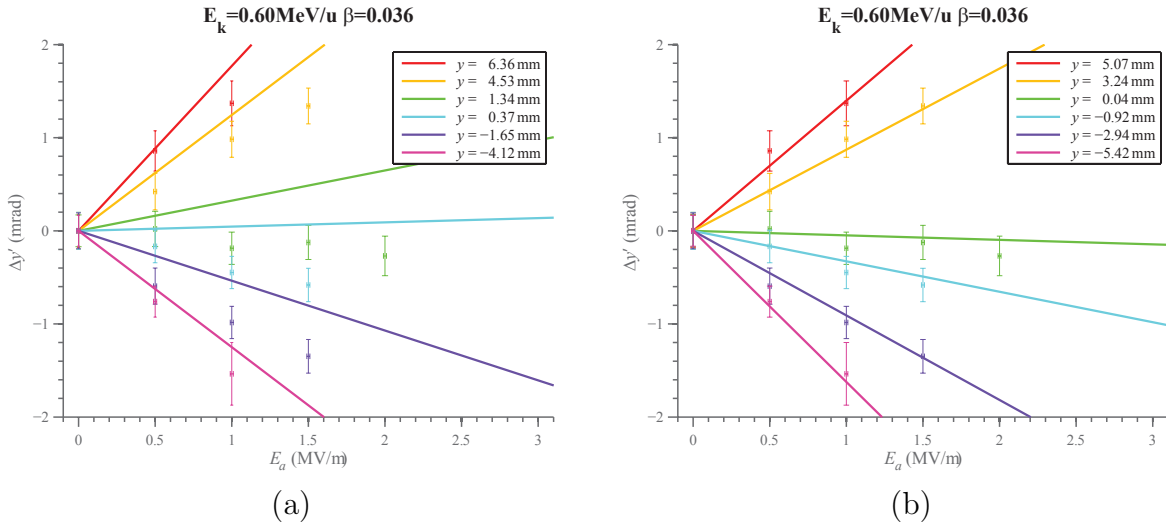


Figure 5.1: Left (a): Raw experimental data of $\Delta y'$ vs. E_a at $E_k = 0.6 \text{ MeV/u}$ ($\beta = 0.036$). Right (b): The same data set with a constant vertical offset, $\delta = 1.29 \text{ mm}$, applied during the analysis.

Introducing a single constant vertical offset, found to be $\delta = 1.29 \text{ mm}$ through a least-squares fitting, lines up the experimental data with the predicted calculations, as seen in Figure 5.1b. The same constant δ works to line up all the data sets regardless of energy, not

just the shown example at $E_k = 0.6 \text{ MeV/u}$, as it arises from the experimental setup and is therefore constant throughout all measurements.

This is a powerful statement for the verification of the steering predictions. As this is the first time such a systematic measurement of the QWR vertical steering has been performed, it is important to note that across all energies measured, and for different tunes that include varied offsets through the test cavity, a single constant δ may be introduced to the analysis to produce a near perfect match of the measured data with the steering predictions.

5.2 Outlook

There is much work that can be continued into the future. Accurate online modeling of accelerator systems is an increasingly important objective to achieve for machines such as ReA and FRIB that require flexible tuning routines and algorithms. Other challenges such as incorporating multiple charge state tracking and QWR steering effects into an online model must be handled sufficiently in the hopes of attaining the best possible working model.

The possibility of incorporating multiple charge state modeling into XAL is an idea for expanding XAL's future online model capabilities. Being able to track multiple charge states in an online model will be especially important for machines such as FRIB.

In the future it is entirely conceivable that quarter wave resonator steering modeling could be included in XAL's online model. This effect, especially now that it has been measured and confirmed experimentally, is critical to introduce into modeling codes if a model of the centroid motion through QWRs and corrector magnets is to be achieved. This is especially significant for modeling objectives such as orbit correction and scaling of linac settings.

APPENDICES

Appendix A

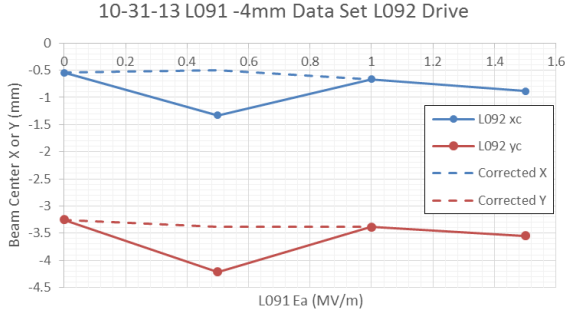
Additional Cavity Measurement

On October 30th, 2013, during the preliminary tuning for the $E_k = 1.08$ MeV/u measurement using the L091 test cavity, it was noted that by chance the final tune resulted in the last solenoid operating at a very low current compared with its nominal value. This solenoid, L090, had a setting of ~ 4 A, while the other solenoids were tuned to values in the range of 10-20 A.

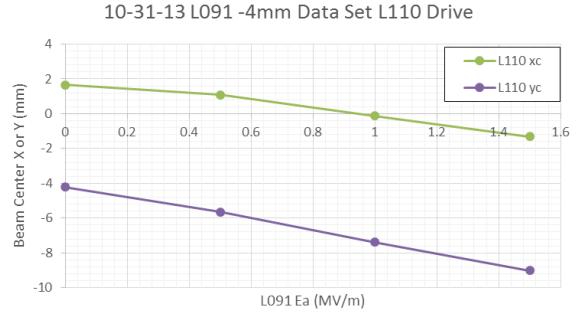
As discussed in Section 4.3, the only additional requirement necessary to use this same measurement technique for the cavities prior to the L091 test cavity is that there is a drift space between the cavity and the diagnostics. As the L090 solenoid field was already minimal, further tuning was pursued until this solenoid and its correctors could be turned off completely. This is the tune that was used to measure the L091 test cavity at $E_k = 1.08$ MeV/u on October 31st, 2013.

After this measurement was completed with the L091 cavity, the same measurement procedure was performed with the L089 cavity. However, on the last data point of the L091 data set there was an abrupt change in the L092 drive reading, as seen in Figure A.1a. There was no corresponding shift in the L110 drive at the same setting, which was taken immediately after the L092 measurement at $E_a = 0.5$ MV/m, indicating that this was an issue with the L092 drive instead of a shift of the beam.

Indeed, the L092 drive failed after the final $E_a = 1.5$ MV/m measurement point of the



(a)



(b)

Figure A.1: Final measurement of L091 data set on 10-31. The $E_a = 0.5$ MV/m L092 data point had all peaks shifted by the same amount. The dashed lines indicate where this overall shift has been manually accounted for in the analysis. L110 data indicates it was an issue with the L092 drive, not a sudden change in the beam, for instance from an instability in the LB source.

L089 data set, ending this data set measurement prematurely. This nearly complete data set is shown in Figure A.2 with two missing measurement points in the $y = 4.21$ mm data set.

The hope was to complete this measurement set with the L089 cavity in addition to the L091 measurement and to extract a relative offset of the cavities with respect to each other, as previously proposed in Chapter 4. By using the procedure introduced in Section 4.2.2 to find δ_{L091} and δ_{L089} , the difference $\Delta = \delta_{L091} - \delta_{L089}$, would be equal to the relative vertical offset of the cavities with respect to one another.

Using the raw data from both measurement to calculate δ_{L091} and δ_{L089} , it is found that $\Delta = 0.97$ mm. With this being a positive value, $\delta_{L091} > \delta_{L089}$, therefore the L089 cavity is $dy = 0.97$ mm above the L091 cavity. This value is suspect, however, due to the change in the L092 drive at the end of the L091 data set. When this shift of 0.83 mm is accounted for, the difference becomes $\Delta = 0.14$ mm. This would indicate that L089 is $dy = 0.14$ mm above L091. There is uncertainty about this result because of the malfunctioning L092 drive during the measurement. It would therefore be beneficial to take the L091 and L089 (and possibly

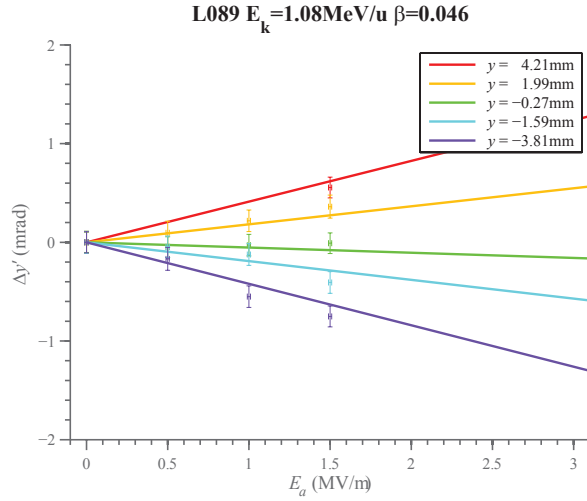


Figure A.2: Plot of $\Delta y'$ vs. E_a for beam energies $E_k = 1.08 \text{ MeV/u}$ ($\beta = 0.046$). Lines correspond to the predicted response calculated using cavity design data and experimental conditions.

even L088) data again without interruption from the L092 drive.

Appendix B

L092 Drive Calibration

The results and analysis shown in the following section are for the QWR steering measurements done at beam energies of 1.3 MeV/u for which $\beta = 0.053$, and 0.6 MeV/u corresponding to $\beta = 0.036$.

The first measurement in the Quarter-Wave resonator steering series of experiments took place on May 6-7, 2013. The second measurement took place on August 29, 2013. The measurement in May was performed at 1.3 MeV/u, while the August measurement used the RFQ energy of 0.6 MeV/u.

During the initial run in May, the slit drive at L092 would not maintain its calibration, and therefore needed to be recalibrated after each slit scan. During preparations for the August experiment, the same slit drive at L092 became inoperable, and a substitute drive had to be installed in its place. It was aligned by eye, with official alignment to take place at a later date. Due to these variables, it was necessary to introduce different calibration offsets for each measurement set in the analysis of the L092 data. The L110 data from both measurement sets used the original calibration during the analysis, as the L110 drive functioned properly during both measurements.

Changing the d_{ref} constant moves the x and y data in opposite directions, as seen through Equation 4.12. By the same equation, we see that changing the d_{offset} constant results in the x and y data moving in the same direction. By adjusting these two constants, it is possible

to fit the May data from L092 to the theory predictions. We could not measure the actual offset of the drive during the May experiment, as the drive failed and had to be removed from the beam line, but the true offset of the drive during the August experiment was measured and compared with the offset value that was used during the analysis.

The L110 calibration constants used in this analysis are $d_{\text{offset}} = -59.4233$ mm and $d_{\text{ref}} = 29.731$ mm from Equation 4.12. The L092 calibration constants for the May experiment (1.3 MeV/u) are $d_{\text{offset}} = -59.4233$ mm and $d_{\text{ref}} = 33.5$ mm. The L092 calibration constants for the August experiment (0.6 MeV/u) are $d_{\text{offset}} = -56.83$ mm and $d_{\text{ref}} = 29.731$ mm. This analysis was performed with only the May and August data. The procedure for producing the d_{offset} values is equivalent to the method for determining δ in Section 4.2.2.

It appears that in May, the L092 slit drive may not have been moving along an exact 45° trajectory. Another possibility is that it may have been offset in the direction perpendicular to the drive motion. During the measurement in May, the drive would continuously slip out of calibration. When it was finally removed from the beam line in August, it was observed that the drive had completely stripped the threads of the bolt holding it in place. This would be consistent with the drive not functioning properly, as we suspected.

In order to match the data to theory, the d_{ref} for L092 in May had to be increased from its original value, which was identical to the L110 calibration. We can interpret this to mean that the beam intercepted the slits along a path that was longer than the path along the central 45° angle, either being due to a change in the angle of the drive or a misalignment along the perpendicular 45° direction. The original d_{offset} value was able to be used to match the data to theory, which indicates that the drive's zero position was properly aligned at the 5 mm hole, with no overall offset along the 45° axis.

For the August data, the drive had to be installed quickly without being properly aligned,

as it was needed immediately. This was acceptable since we knew any misalignment that might occur would be along the 45° axis, which could then be compensated for in the post-processing of the data. As it turns out, the d_{offset} value had changed by ~ 3 mm. This corresponds to an offset along the 45° axis, as predicted would occur since it was aligned by eye. The d_{ref} constant returned to its original value, implying that this drive was properly functioning along the 45° axis, and intercepting the beam as expected.

The interpretation of the May measurements with respect to how well it agrees with theory predictions needs to take into consideration that these offsets were included in the analysis of its L092 data. Even though the reasons for these offsets as described in this section are well understood, it was determined that the best approach would be to redo this energy measurement and avoid using this data set in further analysis, which was the course of action taken.

BIBLIOGRAPHY

BIBLIOGRAPHY

- [1] LT Sun, J Brandon, D Cole, M Doleans, D Morris, G Machicoane, E Pozdeyev, T Roponen, and L Tobos. Intense beam production with SuSI. *ECRIS*, 10:4, 2010.
- [2] PA Závodszky, B Arend, D Cole, J DeKamp, G Machicoane, F Marti, P Miller, J Moskali, J Ottarson, J Vincent, et al. Design of SuSI–superconducting source for ions at NSCL/MSU–II. the conventional parts. *Nuclear Instruments and Methods in Physics Research Section B: Beam Interactions with Materials and Atoms*, 241(1):959–964, 2005.
- [3] G Machicoane, C Benatti, D Cole, M Doleans, OK Kester, F Marti, X Wu, PA Zavodszky, and Chi Zhang. Performance investigation of the nscl 18 ghz superconducting ecr ion source susi. In *in Proceedings of the 2009 Particle Accelerator Conference (Vancouver, Canada 2009)*, 2009.
- [4] RC York, HG Blosser, TL Grimm, F Marti, J Vincent, X Wu, and A Zeller. The NSCL coupled cyclotron project-overview and status. In *Proceedings of the Fifteenth International Conference on Cyclotrons and their Applications*, pages 687–691, 1998.
- [5] D.J. Morrissey. The coupled cyclotron project at the NSCL. *Nuclear Physics A*, 616(1-2):45–55, 1997. Radioactive Nuclear Beams.
- [6] David J Morrissey and Bradley M Sherrill. Radioactive nuclear beam facilities based on projectile fragmentation. *Philosophical Transactions A*, 356(1744):1985–2006, 1998.
- [7] The ISOLDE radioactive ion beam facility. <http://isolde.web.cern.ch/>, December 2011.
- [8] The NSCL at MSU. <http://nscl.msu.edu/>, March 2014.
- [9] D.J. Morrissey, B.M. Sherrill, M. Steiner, A. Stolz, and I. Wiedenhoever. Commissioning the A1900 projectile fragment separator. *Nuclear Instruments and Methods in Physics Research Section B: Beam Interactions with Materials and Atoms*, 204(0):90–96, 2003. 14th International Conference on Electromagnetic Isotope Separators and Techniques Related to their Applications.
- [10] J. Beringer et al. (Particle Data Group). Review of Particle Physics. *Journal of Physics G*, 33:258, 2006.

- [11] Kimberly Purtell, Kaitlynn Rethman, Autumn Haagsma, Joseph Finck, Jenna Smith, and Jesse Snyder. Performance comparison of MoNA and LISA neutron detectors. *Bulletin of the American Physical Society*, 55, 2010.
- [12] MS Wallace, MA Famiano, M-J van Goethem, AM Rogers, WG Lynch, J Clifford, F Delaunay, J Lee, S Labostov, M Mocko, et al. The high resolution array (HiRA) for rare isotope beam experiments. *Nuclear Instruments and Methods in Physics Research Section A: Accelerators, Spectrometers, Detectors and Associated Equipment*, 583(2):302–312, 2007.
- [13] D Bazin, JA Caggiano, BM Sherrill, J Yurkon, and A Zeller. The S800 spectrograph. *Nuclear Instruments and Methods in Physics Research Section B: Beam Interactions with Materials and Atoms*, 204:629–633, 2003.
- [14] S Schwarz, G Bollen, D Lawton, P Lofy, DJ Morrissey, J Ottarson, R Ringle, P Schury, T Sun, V Varentsov, et al. The low-energy-beam and ion-trap facility at NSCL/MSU. *Nuclear Instruments and Methods in Physics Research Section B: Beam Interactions with Materials and Atoms*, 204:507–511, 2003.
- [15] K Minamisono, BR Barquest, G Bollen, PF Mantica, DJ Morrissey, R Ringle, and S Schwarz. Beam cooling and laser spectroscopy (BECOLA) project at NSCL. *Bulletin of the American Physical Society*, 54, 2009.
- [16] G Bollen, DJ Morrissey, and S Schwarz. A study of gas-stopping of intense energetic rare isotope beams. *Nuclear Instruments and Methods in Physics Research Section A: Accelerators, Spectrometers, Detectors and Associated Equipment*, 550(1):27–38, 2005.
- [17] Georg Bollen, C Campbell, S Chouhan, C Guenaut, D Lawton, F Marti, DJ Morrissey, J Ottarson, G Pang, S Schwarz, et al. Manipulation of rare isotope beams—from high to low energies. *Nuclear Instruments and Methods in Physics Research Section B: Beam Interactions with Materials and Atoms*, 266(19):4442–4448, 2008.
- [18] X Wu, G Bollen, M Doleans, TL Grimm, W Hartung, F Marti, S Schwarz, RC York, and Q Zhao. MSU re-accelerator—the re-acceleration of low energy RIBs at the NSCL. In *Proceedings of the 13th Workshop on RF Superconductivity, Beijing, China*, page 28, 2007.
- [19] Daniela Leitner, John Popielarski, Alain Lapierre, Fernando Montes, Georgios Perdikakis, Stefan Schwarz, Walter Wittmer, and Xiaoyu Wu. Status of the ReAccelerator facility ReA for rare isotopes. *Bulletin of the American Physical Society*, 56, 2011.

- [20] M Berz and K Makino. COSY INFINITY 9.0. *MSU Report MSUHEP-060803*, pages 1–62, 2006.
- [21] Ji Qiang, Robert D. Ryne, Salman Habib, and Viktor Decyk. An object-oriented parallel particle-in-cell code for beam dynamics simulation in linear accelerators. *Journal of Computational Physics*, 163(2):434–451, 2000.
- [22] S. Schwarz, G. Bollen, M. Doleans, O. Kester, K. Kittimanapun, M. Kostin, A. Lapierre, M. Portillo, C. Wilson, J.R.Crespo López-Urrutia, and J. Dilling. Status of the EBIT in the ReA3 reaccelerator at NSCL. *Hyperfine Interactions*, 199(1-3):261–267, 2011.
- [23] M Portillo, G Bollen, S Chouhan, O Kester, G Machicoane, J Ottarson, S Schwarz, and A Zeller. An achromatic mass separator design for ions from the EBIT charge breeder at the NSCL. *PAC2009, Vancouver, May, 2009*.
- [24] Oliver Kester, D Bazin, C Benatti, J Bierwagen, G Bollen, S Bricker, S Chouhan, C Compton, K Davidson, J DeLauter, et al. The MSU/NSCL re-accelerator ReA3. In *International Conference on Radio Frequency Superconductivity*, pages 57–61, 2009.
- [25] J Schmidt, J Maus, N Mueller, A Schempp, O Kester, and J Haeuser. Tuning of the 4-Rod-RFQ for MSU. 2010.
- [26] W Hartung, J Bierwagen, S Bricker, C Compton, J DeLauter, P Glennon, M Hodek, M Johnson, F Marti, P Miller, et al. Superconducting quarter-wave resonator cavity and cryomodule development for a heavy ion re-accelerator. In *Proceedings of XXIV International Linear Accelerator Conference, Victoria, BC, 2008*.
- [27] O Kamigaito. World-wide efforts on rare isotope and radioactive ion beams. volume 10, 2010.
- [28] X Wu, B Arend, C Compton, A Facco, M Johnson, D Lawton, D Leitner, F Montes, S Nash, J Ottarson, et al. The design and commissioning of the accelerator system of the rare isotope reaccelerator–rea3 at michigan state university. *High-Intensity High-Brightness Hadron Beams (HB), Beijing, China, 2012*.
- [29] Conceptual Design Report for the Facility for Rare Isotope Beams (FRIB) at Michigan State University, 2010.
- [30] R York, S Assadi, G Bollen, T Glasmacher, W Hartung, MJ Johnson, G Machicoane, F Marti, E Pozdeyev, M Syphers, et al. Technical challenges in design and construction of FRIB. *FROBN2, PAC*, 11:2561, 2011.

- [31] T Pelaia II. Open XAL status report 2013. 2012.
- [32] Ji Qiang. IMPACT-T user document version 1.6. Lawrence Berkeley National Laboratory: LBNL Paper LBNL-62326 <http://www.escholarship.org/uc/item/2sw7g9c3>, 2010.
- [33] M Berz and K Makino. COSY INFINITY version 8.1. user's guide and reference manual. *Department of Physics and Astronomy MSUHEP-20704, Michigan State University*, 2002.
- [34] D. A. Edwards and M. J. Syphers. *Transverse Linear Motion*, pages 57–98. Wiley-VCH Verlag GmbH, 2008.
- [35] L.N. Hand and J.D. Finch. *Analytical Mechanics*. Cambridge University Press, 1998.
- [36] E. D. Courant and H. S. Snyder. Theory of the alternating-gradient synchrotron. *Annals of Physics*, 3(1):1–48, 1958.
- [37] D. C. Carey. *The Optics of Charged Particle Beams*. Second Printing with Corrections. Harwood Academic Publishers, Reading, UK, 1992.
- [38] H. Wiedemann. *Particle Accelerator Physics*. Springer, 2007.
- [39] Kenneth R Crandall and DP Rusthoi. *Trace 3-D Documentation*. Los Alamos National Laboratory, 1987.
- [40] Michiko G Minty and Frank Zimmermann. Longitudinal phase space manipulation. In *Measurement and Control of Charged Particle Beams*, pages 175–209. Springer, 2003.
- [41] H Goldstein, C Poole, and J Safko. Classical mechanics. *Classical mechanics (3rd ed.) by H. Goldstein, C. Poole, and J. Safko. San Francisco: Addison-Wesley, 2002.*, 1, 2002.
- [42] Open XAL. <http://xaldev.sourceforge.net/>, 2014.
- [43] Eduard Pozdeyev. Private Communication.
- [44] L. D. Landau and E. M. Lifshitz. *Electrodynamics of continuous media*. Elsevier et al., Amsterdam et al., 2008.
- [45] CST-computer simulation technology, 2013.

- [46] Winter Zheng. Private Communication.
- [47] Thomas P Wangler. *Principles of RF linear accelerators*. Wiley Beam Phys. Accel. Technol. Wiley, New York, NY, 1998.
- [48] Daniela Leitner, Michelle L Galloway, Timothy J Loew, Claude M Lyneis, I Castro Rodriguez, and Damon S Todd. High intensity production of high and medium charge state uranium and other heavy ion beams with venusa). *Review of Scientific Instruments*, 79(2):02C710, 2008.
- [49] Guillaume Machicoane, Dallas Cole, Daniela Leitner, Derek Neben, and Larry Tobos. Metallic beam development for the facility for rare isotope beama). *Review of Scientific Instruments*, 85(2):02A957, 2014.
- [50] SA Kondrashev, A Barcikowski, B Mustapha, PN Ostroumov, RH Scott, SI Sharamentov, and NV Vinogradov. Experimental results on multi-charge-state LEBT approach. In *Particle Accelerator Conference, 2007. PAC. IEEE*, pages 1658–1660. IEEE, 2007.
- [51] PN Ostroumov, A Barcikowski, SA Kondrashev, RH B Mustapha, NE SI Sharamentov, et al. Extraction from ecr and recombination of multiple-multiplecharge state heavy-ion beams in lebt. LINAC, 2008.
- [52] Jun Tamura, Toshiyuki Hattori, Noriyosu Hayashizaki, Takuya Ishibashi, Taku Ito, Takeshi Kanetsue, Hirotsugu Kashiwagi, and Masahiro Okamura. Multiple charge state ion beam acceleration with an RFQ LINAC. Venice, ITALY, 2009. HIAT09.
- [53] PN Ostroumov and KW Shepard. Multiple-charge beam dynamics in an ion linac. *Physical review special topics-accelerators and beams*, 3(3):030101, 2000.
- [54] Christopher Allen. Theory and technique of beam envelope simulation: Simulation of bunched particle beams with ellipsoidal symmetry and linear space charge forces. <http://wiki.ornl.gov/sites/xaldocs/XAL%20Documentation/Documents/SimulatingBeamsWithEllipsoidalSymmetry-SecondEdition.pdf>, August 2002.
- [55] A. Facco and V. Zvyagintsev. Beam steering in superconducting quarter-wave resonators: An analytical approach. *Physical Review Special Topics Accelerators and Beams*, 14(7):070101, July 2011.
- [56] PN Ostroumov and KW Shepard. Correction of beam-steering effects in low-velocity superconducting quarter-wave cavities. *Physical Review Special Topics-Accelerators and Beams*, 4(11):110101, 2001.